School of Biosciences

Measuring the sp2/sp3 Carbon Content Ratio in a Single Nanodiamond Using Quantitative Optical Microscopy

Samuel Owen Hamilton

Thesis Presented for the Degree of Doctor of Philosophy
School of Biosciences
Cardiff University

3$^{\text{rd}}$ November 2023

Contents

List of Acronyms

CARS   coherent anti-Stokes Raman scattering

CNTs   carbon nanotubes

CVD   chemical vapour deposition

DIC   differential interference contrast

DND   detonation nanodiamond

DLS   dynamic light scattering

HPHT   high pressure high temperature

NA   numerical aperture

ND   nanodiamond

NPs   nanoparticles

NTA   nanoparticle tracking analysis

PGF   pristine graphene flake

PS   polystyrene

PSF   point spread function

qDIC   quantitative Differential Interference Contrast

SRS   stimulated Raman scattering

SWCNTs   single wall carbon nanotubes

List of Figures

List of Tables

Abstract

The uses for dielectric nanoparticles, in particular nanodiamond (ND), cover a wide variety of fields including drug delivery and biomarkers in medicine. This is due to the properties of ND, being non-toxic, mechanically hard, and offering facile functionalisation chemistry. An important aspect modulating these properties is the presence of sp2 hybridisation at the surface, which changes the surface chemistry and the optical absorption properties. Treatments to reduce surface sp2 have been developed, however, a non-destructive method to accurately measure the sp2/sp3 ratio of single NDs is lacking. This thesis presents such a method, determining this ratio combining the optical microscopy methods of quantitative differential interference contrast (qDIC), extinction, and photothermal microscopy.

By converting an optical phase gradient to an intensity change, DIC enables the detection of dielectric nanoparticles. A method to determine the size of these particles from DIC has been developed, for which a calibration has been carried out using polystyrene beads of 100 nm radius. This showed the technique to be accurate to better than 10% in volume, with the smallest detectable particles being limited by background and shot noise. Measurements of milled nanodiamonds with nominal sizes of below 50 nm, showed a nearly exponential size distribution with a mean size of 28 ± 1.4 nm.

When illuminated, nanoparticles (NPs) cause attenuation of the transmitted light due to scattering and absorption, the sum of which is the extinction caused by the NP. A wide-field microscopy method by which the extinction cross section of NPs can be obtained has previously been developed. Since pure sp2 samples are absorbing under illumination by visible wavelengths, and scattering can be neglected, measurements of the extinction cross section could be obtained.

Photothermal background has been shown to be present in stimulated Raman scattering (SRS) measurements. The absorption of the Stokes beam causes a temperature change, which by the formation of a thermal lens causes a modulation of the pump beam, detected as stimulated Raman loss (SRL). Using this photothermal imaging on individual nanodiamonds, by using a Stokes wavelength which is absorbed by surface sp2 and delaying the pump by a set time, photothermal signal from the NDs can be used to determine the absorption by sp2. Correlative qDIC measurements of the same nanodiamonds, along with correlative optical extinction and photothermal measurements of a pure sp2 sample, allowed for quantitative determination of the sp2/sp3 ratio of individual NDs. Investigations into NDs that had been commercially purchased, and subsequently treated by a combination of temperature annealing and acid etching to reduce the amount of surface sp2, were carried out. It was found that the treatment procedure reduced the surface sp2 significantly, from up to 150% coverage (meaning a layer and a half of sp2 surface coverage around the ND) when untreated to around 30% when treated. The small-

est area of sp2 detectable using this technique was 52 nm^2, corresponding to a full surface layer coverage of a diamond with an edge length of 10 nm assuming cubic geometry.

Similarly to NDs, carbon nanotubes (CNTs) also have a wide range of uses in medical and biotechnology applications due to their tensile strength, and their electrical properties. The electrical properties of a given CNT depend on a property known as its chiral index. Techniques by which this property of individual CNTs can be determined are available in the form of atomic force microscopy and Raman spectroscopy, however these require specialised setups to carry out. While the progress of work here was limited due to the Coronavirus pandemic, an investigation to determine the best sample preparation procedure to deposit CNTs onto a coverslip ensuring the presence of individual nanotubes has been carried out. Subsequent initial measurements of individual CNTs to determine their extinction cross section using a wide field microscope were started. It was found that a nanotube concentration of 2 μg/ml provided an adequate distribution of CNTs on the coverslip surface such that individual nanotubes could be identified.

Given the respective properties of carbon allotropes such as NDs, making them desirable in many applications, are heavily dependant on the structures of individual NPs, it is important to have the ability to accurately characterise them prior to use. Presented here is a method by which the surface sp2 content in individual NDs can be measured using non-destructive techniques. This would allow for such characterisation of samples prior to use, providing the ability to screen samples which contain either too much or too little sp2 for a given application.

Acknowledgements

I would first like to thank Prof. Paola Borri and Prof. Wolfgang Langbein for their support throughout my PhD. Their expertise, guidance, and advice have been key to the success of this project, particularly in the early stages of the pandemic when it was hard to know how anything would progress. I would also like to extend my gratitude to Dr. David Regan, Dr. Lukas Payne, and Dr. Sion Harlow for the training they have provided in utilising the sample preparation and microscopy techniques, as well as the various analysis software, required for this project.

To everyone else in the QOBI group as well, thank you for the support through 3 extremely difficult years. The work required to present a viable PhD thesis is hard enough at the best of times, but through COVID became yet harder. The support all in this research group provide each other has helped me through even the toughest times. My special thanks in this regard goes to Martina and Furqan, who have both provided me with a sounding board when experiments went wrong.

On a more personal level I could not have undertaken, let alone completed, this project without the support of my mother and father, or of my girlfriend. All have given me the strength and encouragement I have needed to succeed. Without my mother's patience listening to my problems and offering advice, my father's encouragement to carry on when everything seemed too difficult, and indeed my girlfriend's shoulder to cry on when it all got too much I could not have hoped to be where I am now. Thank you, I love you all.

Finally, I must thank all those at CoolLED for their unending support as I wrote this thesis. Particularly to Mr. Gerard Whoriskey, Mr. Alex Gramann, and Mr. Luther Hindley who have all shown an incredible level of patience and understanding during the last 7 months. I'm looking forward to the next phase of my working life with CoolLED, and couldn't think of a better place to be.

Chapter 1

Introduction

1.1   Bulk Diamonds and Nanodiamonds

1.1.1   sp2/sp3 Structure and Formation

sp2 and sp3 hybridisation, when discussing carbon compounds, refer to graphitic and diamond-like carbon, respectively. During the formation of carbon compounds, the restructuring of the electron orbitals of carbon atoms gives rise to strong covalent bonds. Carbon has the electron configuration $1s^2\ 2s^2\ 2p^2$, with the 2s and 2p states being nearly degenerate, allowing mixing by a small perturbation. Mixing the s and all three p orbitals results in sp3 hybridisation, with orbitals extended in a tetrahedral geometry. Mixing only two of the three p orbitals creates Sp2 hybridisation, resulting in a planar triangular geometry. Therefore, sp3 hybridisation results in four partially filled hybrid orbitals, while sp2 hybridisation results in three hybrid orbitals with equal energy levels [1]. The process by which sp2 hybridisation occurs requires one s orbital and two p orbitals, from which a σ-π bond is formed with a bond angle of 120° [2]. For sp3 hybridisation, one s orbital and three p orbitals are required, forming a tetrahedral structure with bond angles of 109.5°. The 's character', or the ratio of s orbitals to p orbitals, of each of these hybridisations gives an idea of which is more stable. Sp2 hybridisation has a greater s character (33%), compared to that of sp3 hybridisation (25%), meaning the electrons are held closer to the nucleus with shorter bonds and hence are more stable due to the increased energy required to break them [3]. An experiment published in 1983 used Fourier transform nuclear magnetic resonance (FT NMR) of carbon-13 nuclei in a graphite lattice to determine the carbon-carbon bond lengths in the lattice. This experiment found that graphite has a bond length of around 142 pm [4] and corroborated previously found bond lengths of pyrolytic graphite found using x-ray diffraction [5]. This is shorter than the bond length found for diamond which is 154 pm [6]. Figure 1.1 shows the structures of graphite and diamond, with their respective bond lengths and angles.

1.1.2   Diamond Growth

In order for diamonds to form, very high pressures and temperatures are typically required. Naturally occurring diamonds are thought to form by way of carbonate melts at depths of up to 200 km in the lithospheric mantle, denoted by the red shaded region in the carbon phase diagram in Figure 1.2, in which diamond is metastable. Models of diamond formation in this region typically use temperatures

of between 1100°C to 1200°C, and pressures of 6 GPa [7, 8]. However, a recent experiment conducted by Palyanov et al. was designed to mimic the conditions by which diamonds naturally form primarily in the lithospheric mantle in the presence of an electric field to better understand the process of natural diamond formation. The experiment used pressures of 6.3 GPa and 7.5 GPa along with temperatures of 1300°C to 1600°C, and a potential difference of 0.4 V to 1 V across electrodes separated by distances of 8 mm at 6.3 GPa and 6 mm at 7.5 GPa, to produce diamonds from carbonate-silicate and carbonate melts. The experiment showed that some of the characteristics found in the diamonds obtained were similar to those found in so-called Type Ia natural diamonds (see definition below), such as a high nitrogen content, at around 1000 atomic parts per million, and carbonate inclusions [9]. Type I diamonds are the most common naturally occurring diamonds, making up 98% of those found, which are further subdivided into Type Ia and Type Ib, of which Type Ia makes up 99%. Type Ia diamonds contain nitrogen aggregates such as A centres (two substitutional nitrogen atoms in the lattice) and B centres (substitutional nitrogen atoms surrounding a central vacancy in the lattice), and absorb infrared light at $1282\,\mathrm{cm}^{-1}$ and $1175\,\mathrm{cm}^{-1}$, respectively [10, 11]. Type Ib diamonds also contain substitutional nitrogen atoms in the lattice, however, at a lower concentration than is found in type Ia diamonds forming singly substituted atoms as opposed to aggregates. These type Ib diamonds are less common due to the tendency for nitrogen atoms to aggregate in diamond lattices over the length of time the diamonds spend in the upper mantle [12]. Type II diamonds are less common naturally, and have subtypes IIa and IIb. Type IIa make up between 1 - 2% the number of natural diamonds found and have very low concentrations of nitrogen ($< 1\,\mathrm{ppm}$), therefore any colour present in the diamond is due to plastic deformation in the diamond lattice caused by dislocations [13]. Type IIb diamonds are the rarest natural diamonds, containing substitutional boron atoms in the diamond lattice. Due to the boron being an acceptor in the diamond lattice, type IIb diamonds are p-type semiconductors with an acceptor activation energy of 0.34 eV [14, 15]. Hence, this defect in the diamond lattice causes a strong absorption of infrared light at $2803\,\mathrm{cm}^{-1}$ ($3.56\,\mu\mathrm{m}$) as well as increased absorption in the visible light spectrum from red through yellow wavelengths, causing the blue appearance of these diamonds [11, 16].

The primary ways by which diamonds can be made synthetically are by detonation, high pressure high temperature (HPHT) synthesis, and by chemical vapour deposition (CVD). HPHT synthesis replicates the natural formation of diamonds [17], and has two variants, catalytic and non-catalytic synthesis, using presses to achieve the required pressures and temperatures for diamond growth. As can be seen from the purple shaded region in Figure 1.2, non-catalytic HPHT requires very high pressures of around 15 GPa and temperatures between 2000°C and 4000°C. Catalytic HPHT diamond synthesis typically uses catalysts such as Fe, Ni, or Co to reduce the required pressure and temperature significantly, to be around 5 GPa to 6 GPa and between 1300°C to 1600°C [18]. The conditions required for catalytic HPHT synthesis can be seen in the blue shaded region of the phase diagram in Figure 1.2. HPHT using catalysts requires purer starting material, particularly limiting initial nitrogen and hydrogen present, and has been shown to produce NDs with metallic inclusions due to the molten catalyst becoming trapped in the diamond lattice during growth [19]. It was shown [20] that the nitrogen and hydrogen from a starting material, such as melamine powder, disturbed the nucleation of diamond, while also reacting with the Mn, Co, and Ni catalysts forming nitrides and hydrides,
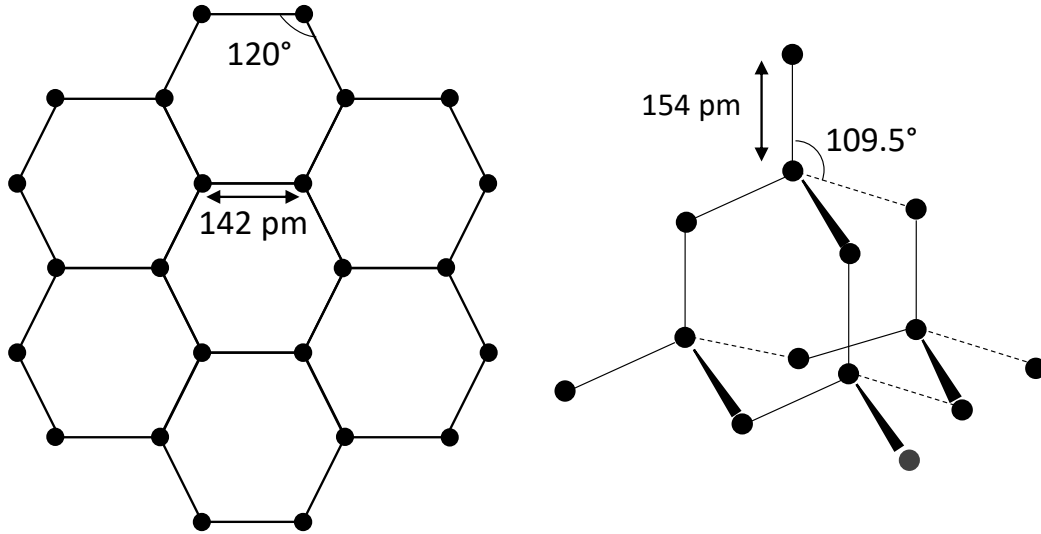
Figure 1.1: Structure of graphite (left) with bond angle of 120° and bond length of 142 pm. Structure of diamond (right) with bond angle of 109.5° and bond length of 154 pm.

thus changing the properties of the catalysts and reducing diamond growth. As such it is better to use graphite as a starting material. Diamonds grown by HPHT can have a number of uses ranging from jewellery to machining. A method of growing boron doped diamonds (BDDs) by HPHT, for electrochemical components, has also been developed using pressures of 5.5 GPa at 1200°C from graphite powder and aluminium diboride, with carbonyl Fe and Ni powders as catalysts. The resulting diamonds showed a high enough concentration of boron to be used in electrochemical applications while having a negligible number of sp2 bonds [21].

CVD synthesis is a process by which atoms from a plasma are deposited onto a substrate under vacuum conditions, and can be used to produce diamonds in a variety of ways, the most common being hot filament and microwave plasma. Other types of CVD include RF discharge [23], electron assisted [24], dc discharge [25], and laser-assisted deposition [26]. All methods involve a gas mixture containing a hydrocarbon, hydrogen, and sometimes oxygen. In hot filament CVD a tungsten filament is heated to between 1700°C and 2000°C to break the bonds between atoms in the precursor gases (typically methane and hydrogen), forming atomic hydrogen and carbon [27]. Microwave plasma CVD uses microwave generators of up to 100 kW power to produce microwaves of 2.45 GHz which in turn generates and sustains a plasma by impact ionisation of the precursor gases [28, 29]. Unlike in other diamond synthesis methods using solid and liquid phases (such as HPHT), CVD works in gas to solid phase, with a gas pressure below 10 kPa. The resulting carbon atoms are then deposited onto a substrate, typically made of silicon or silicon carbide which is heated to between 700°C and 1200°C. The green shaded region in Figure 1.2 shows the conditions under which CVD occurs, note it is the only synthesis method in which diamond is not in the stable phase. This is why the hydrogen gas is important when conducting diamond growth by CVD. Atomic hydrogen is what allows for diamond growth in these systems as the hydrogen etches away sp2 bonded atoms, thus promoting sp3 growth [27]. The Bachman diagram in Figure 1.3
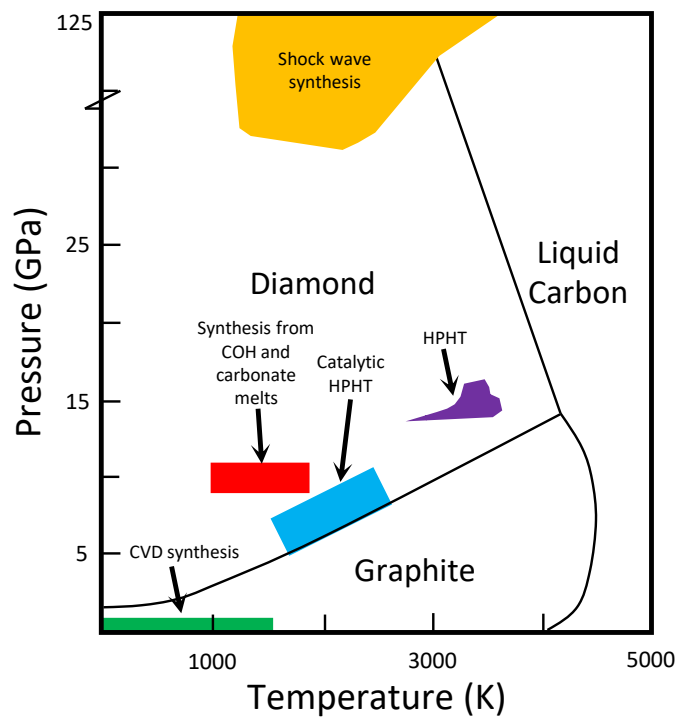
Figure 1.2: Carbon phase diagram showing the temperatures and pressures required for diamond and graphite formation. Temperatures and pressures required for detonation (orange region), HPHT (purple and blue regions), and CVD (green region) formation of diamond can also be seen. Figure adapted from [22].
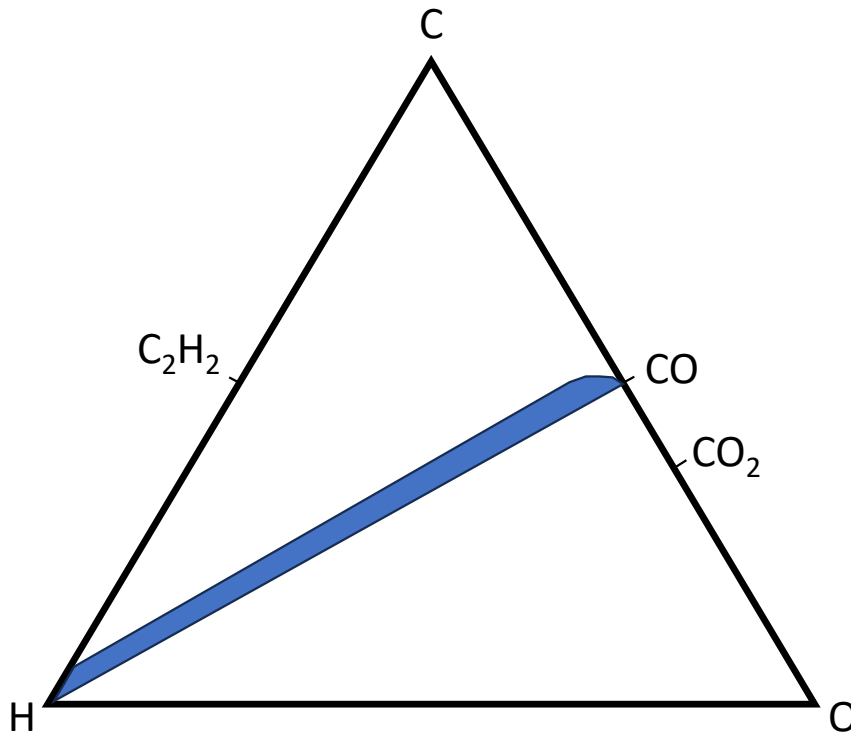
Figure 1.3: Bachman diagram with a blue line showing the region of diamond growth using CVD. The area above the blue line shows the region of graphitic growth, while the region below the line represents the region of no deposition. Figure adapted from [31].

shows the ratios of the respective elements (C, H, and O) required for CVD growth of diamonds. In this diagram, the blue region shows the ratios of each element that will allow for diamond growth, while the region above this is where carbon concentration is too high causing non diamond carbon to form, and below the ratio of oxygen to carbon is too high resulting in no growth [30].

Detonation or shock wave synthesis is a simple and quick way to produce nanodiamonds. These are typically between 5 nm and 100 nm in size, and are made up of sp3 bonded carbon as with bulk diamond, but surrounded by sp2 due to the latter parts of the formation at lower pressure/temperature. While this allows them to have similar properties to their bulk material counterparts, they have some benefits due to their size such as functionalised surface groups which allow for greater colloidal stability [32]. There is also a change to the phase diagram worth noting which applies at the nanoscale, and is dependant on the cluster size being produced. For smaller clusters the liquid phase occurs at lower temperatures, while the pressure for diamond formation increases due to the Gibbs free energy being dependant on the surface energy [33]. Detonation synthesis uses strong high explosives such as trinitrotoluene (TNT) and hexogene, causing extremely high pressures and temperatures for a very short period [34]. The resulting purity of the detonation nanodiamond (DND) has been shown to depend on the explosives mixture used, with 100% TNT yielding $< 4\%$ ND while a 60%:40% TNT:RDX mixture resulted in a yield of 8.4% ND [35]. The orange shaded region in Figure 1.2 shows the typical conditions under which detonation synthesis occurs.

1.1.3 Nanodiamond Milling

It is also possible to produce NDs from bulk material by a process known as ball milling. This method uses balls made typically of steel or tungsten carbide, to grind the bulk diamond down to sizes of less than 100 nm, and has been shown to produce NDs with a high yield of fluorescent defects [36, 37]. This occurs particularly when HPHT grown diamond is used as a precursor, but makes this technique suitable for production of NDs for bioimaging and medicine (as is discussed further in Section 1.1.5) [38].

1.1.4 Characterisation and Treatment Methods

During diamond synthesis it is common for defects to occur in the diamond lattice. As discussed previously, it is possible for non-diamond carbon to be deposited during CVD synthesis if incorrect gas mixtures are used. Initial measurements for finding an sp2/sp3 ratio of carbon in diamonds used Raman spectroscopy to determine whether microwave or hot filament CVD produced higher quality diamond films [39]. To do this, a diamond quality factor (f_q) was calculated from Raman spectra using the equation

$$f_q = \frac{100}{1 + 75 I_n d / I_d} \cdot \, , \tag{1.1}$$

where I_d is the area of the 1332 cm^{-1} Raman sp3 peak, and I_{nd} is the sum of the sp2 D and G peak areas. The G peak occurs at 1575 cm^{-1}, and is the primary Raman mode for sp2 bonded carbon, while the D peak can be seen at 1355 cm^{-1} which is the breathing mode for the sp2 rings and indicates the presence of defects in the sp2 structure. It was found that both synthesis methods produced diamond with similar f_q. This method has also been used to determine how the methanol concentration used during hot filament CVD affects the resulting film quality factor [40]. More recently, the possibility of using x-ray photoelectron spectroscopy (XPS) to determine the ratio of sp2 and sp3 carbon in diamonds has been explored. To do this the C1s XPS peak (which indicates the presence of C - C, C - O - C, and O - C = O bonds in a sample), carbon KVV auger spectra (standing for core-valence-valence and indicating the release of auger electrons which has been linked to the amount of sp2 carbon in a material [41]), and valence band spectra (providing information about the density and occupancy of electronic states in a material) were analysed and compared with f_q. It was found that the sp3 fraction calculated using all analysis methods showed good agreement with each other. However, the C1s and KVV auger analysis methods only allow for analysis at depths down to 2 nm and 1 nm into the films, respectively [42]. Prior to this, XPS had been used to determine the sp2 percentage present in HPHT grown nanodiamonds with sizes of < 10 nm by deconvolution of the C1s peak. It was found that as much as 25 wt% sp2 carbon was present in both shells surrounding the diamonds, and as stand alone dots in the lattice. Air annealing of the diamonds at temperatures of 450°C for 30 minutes was sufficient to remove this sp2 carbon [43].

As well as surface sp2, there are other defects that can be found in diamonds after synthesis. Other materials such as silicon, titanium, and ferrous salts have been found in NDs formed by detonation synthesis along with the sp2 shell which commonly surround these DNDs. Methods by which these defects can be removed from the diamonds have been studied, and it is possible to use acids such as hydrochloric acid and hydrofluoric acid to remove them [44]. Removing these defects

is particularly important for some applications, particularly biological ones, as these metals can change the behaviour of diamonds in aspects such as increasing cytotoxicity. In these circumstances, it is preferable to start with single crystal CVD grown diamond which are milled to produce nanodiamonds. However, it has been shown that using a tempered steel grinding bowl to do this can lead to iron impurities in the diamond, and the use of silicon nitride instead results in non-diamond carbon formation [45].

1.1.5   Biological Uses of Nanodiamonds

Diamonds have a number of applications outside of gem diamonds. Research into the use of nanodiamonds for biological applications has been one of them. Importantly for these applications, studies have shown that NDs (made up of sp3 carbon) have the lowest cytotoxicity when compared with sp2 carbon based nanoparticles such as carbon black, multi-wall carbon nanotubes, and single-wall carbon nanotubes [46]. Some previous studies have shown evidence that DNDs can cause the destruction of white blood cells by changing the kinetics of active oxygen generation [47], though this could have been due to high level of sp2 present on DND surfaces as discussed in Section 1.1.2. Results of studies into the effects of NDs on red blood cells showed that 5 nm DNDs and 100 nm HPHT grown NDs show no effects on red blood cell viability. It is worth noting that the NDs did affect the red blood cells in terms of their deformability which the authors suggest would need to be controlled during treatment [48]. Similarly, other studies have found that NDs which had undergone purification by oxidation in air and using strong oxidative acids, such that the surface was functionalised with a variety of different oxygen containing groups including carboxyl groups, cause minimal damage to human blood in vitro. Moreover, low ND concentrations do not affect red blood cell oxygenation and do not induce an immune response in an in vivo animal model [49, 50]. Further investigations into the cytotoxicity of NDs ranging from 2 - 10 nm in size found that diamond is also non-toxic to cell lines from macrophages and neuroblastomas [51].

Nanodiamonds can be used for a variety of biological applications including anticancer therapy, gene delivery, as antimicrobial agents, and for biomedical imaging [52]. To be used as an anticancer treatment, the surface of the NDs are functionalised to carry drugs which can then be released into tumour cells. A range of drugs have been studied for this purpose such as a combination of paclitaxel and cetuximab. This combination has been shown to bind specifically to colorectal cancer tumours, with the NDs subsequently being taken up by cells by a process known as macropinocytosis, causing inhibition of tumour growth and death of cancerous cells by inducing apoptosis [53]. Other drugs that have been studied are tetracyclines and 4-hydroxytamoxifen. An important aspect of this research is the adsorption and desorption to the nanodiamonds. A study published in 2016 showed that tetracycline binds strongly to ND surfaces functionalised with a COOH group. The desorption of this drug was found to be dependant on pH, as desorption was found to be lower at a more alkaline pH compared to acidic pH [54]. Another challenge to treatment of cancer is metastasis, in which a part of the initial tumour breaks away and travels to another part of the body, typically via either the bloodstream or the lymphatic system [55], and often occurs for chemoresistant tumours. Epirubicin has been investigated for its adsorption ability to NDs, as well as its effectiveness in killing chemoresistant cancer stem cells when delivered by NDs. In order to load the NDs with epirubicin, a basic solution was required and could be carried out with 20%

loading efficiency (the ratio of the amount of drug adsorbed on the NP compared to the total amount used in their preparation). The resulting NDs showed a high effectiveness at killing chemoresistant cancer stem cells as well as impairing tumour initiation [56]. It has also been shown that other types of drug resistant tumours such as MCF-7/ADR cells, commonly used to model breast cancer cells, could be treated with a combination of doxorubicin and malaridine at a ratio of 5 : 1 bonded to the ND surface [57].

Gene therapy is typically carried out using a viral vector, meaning that a virus is used to enter a cell and deliver DNA to cells in a process known as transfection [58]. One such example of this is the use of the *Rous sarcoma* virus transposing its DNA into eukaryotic cells [59]. Recently however, there has been research into the use of NPs for this purpose due to the cytotoxicity of the viral vectors. NP materials used include gold, silica, calcium phosphate, and diamond [33, 60]. It has been shown that NDs of 2 - 5 nm size purified using Fenton oxidation can cross HeLa cell membranes and diffuse into the nucleus of the cells, delivering a plasmid into the nucleus, and hence showing that NDs can be used for transfection of genetic material into cells [61].

NDs have also been loaded with carbohydrate and antibiotic drugs to treat bacterial infections. It was found that mannose functionalised NDs were effective in preventing the adhesion of *E. coli* to both biotic and abiotic surfaces, while also blocking biofilm formation [62]. However a subsequent study suggests that, while mannose functionalised NDs show some effect on the survival of *S. aureus* bacteria, they have little effect on *E. coli* [63]. More recently, research into the use of nanodiamonds embedded in *gutta percha*, functionalised with the antibiotic amoxicillin, has been carried out for use in root canal therapy. This is motivated by the enhanced mechanical properties of the ND over using unmodified *gutta percha* [64]. Clinical trials for the use of *gutta percha* reinforced with 5 nm NDs for root canal therapy began in 2016 and was due to be completed in December 2021 [65].

Beyond the uses of NDs using the functionalisation of the nanodiamond surface to carry a drug or material for treatment, their fluorescence is used in bioimaging. Most imaging methods using diamonds make use of particular defects in the diamond lattice, the most common of which are nitrogen vacancy (NV) centres. Though NV centres can occur naturally, vacancies can be created by either proton or electron irradiation, while nitrogen atoms can be directly implanted into the lattice. After implanting the nitrogen atoms and generating vacancies, the diamonds are annealed at temperatures above 500°C for several hours in vacuum to allow for the vacancies to migrate through the lattice to pair with a nitrogen atom, forming an NV centre [66, 67]. The structure of an NV centre in a diamond lattice can be seen in Figure 1.4. Typically, when imaging biological samples using NV centres, it is their fluorescence properties that are exploited. The most common NV centre produced during the irradiation and annealing method is the negatively charged NV^- centre, which absorbs strongly around 560 nm and fluoresces around 700 nm, while not suffering from photobleaching (though it is worth noting they can lose their charge to become a non fluorescent NV^0 centre) [68]. The non-toxicity and fluorescence of NDs containing NV centres has been tested, as well as NV containing NDs encased in both porous silica (PS) and mesoporous silica nanoparticle (MSN) shells. It has been shown that the addition of the PS and MSN shells do not significantly affect the non-toxicity of the NDs, and when using the MSN shell there are fewer electron traps at the ND surface due to the change in surface chemistry giving rise to an
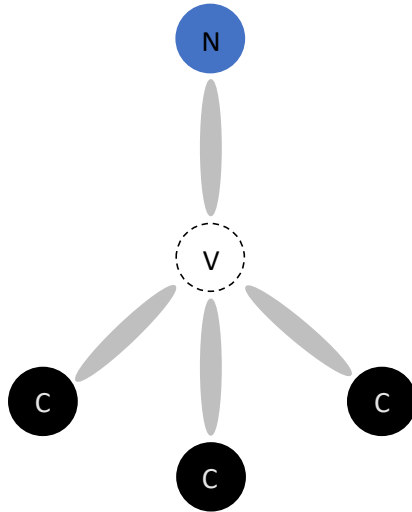
Figure 1.4: Diagram showing the structure of a nitrogen vacancy centre in a diamond lattice.

enhanced photo-luminescence signal. Further, it was shown that the porous silica coating allowed for better dispersion of NDs in aqueous solution leading to better uptake of NDs into cells [69]. An in-vivo study of the toxicity of fluorescent NDs has also been carried out in *C. elegans* worms. It was found that the NDs caused no increased morbidity or decreased reproductive potential in the worms [70]. The use of NDs containing fluorescent NV^- colour centres to track the spread of Alzheimer's disease has also been tested. NDs were functionalised with a peptide which can track amyloid β (Aβ) aggregates, a known biomarker for Alzheimer's. The results showed that the NDs were taken up into cells and allowed for detection of the Aβ aggregates, both in-vitro and in-vivo [71]. It is also possible to obtain other fluorescent vacancy centres, such as the silicon vacancy (SiV) centre and the europium vacancy (EuV) centre which show fluorescence peaks at 739 nm and 612 nm, respectively [72, 73]. Moreover, it has been reported that some surface groups can produce fluorescence signals such as hydroxyl, ketone, and ester groups which produce broad fluorescence peaks centred at around 500 nm, 520 nm, and 570 nm, respectively [74]. It is important to note that, during experiments into the efficiency of NV centres, surface sp2 has been shown to suppress the fluorescence signal from NV centres by removing the charge and forming NV^0 centres, while surface oxygen groups seem to activate NV centres [75, 76, 77].

Studies exploiting the Raman response of diamonds have shown an alternative to fluorescence to image NDs in cells. Non fluorescing single NDs have been imaged inside both fixed and live HeLa cells using the strong coherent anti-Stokes Raman scattering (CARS) signal from the LO phonon (a quantum of energy associated with a lattice vibration) diamond resonance at $1332 \, \text{cm}^{-1}$. This study also quantified the relationship between the CARS signal strength for single NDs, and their sizes found by quantitative differential interference contrast microscopy (qDIC) [78]. However, when using this method to image NDs, it is very important to eliminate any sp2 content in the diamond lattice. While sp3 has a very sharp Raman resonance peak, sp2 carbon has very broad resonances. It is also possible that the absorption of light by the sp2 bonds causes the sp3 bonds to relax into graphite, leading to ND instability.

From the discussed biological uses of NDs it is clearly important to know the amount of sp2 carbon present on the surface of single NDs. More generally, it is important to quantify this ratio as a quality control when manufacturing NDs. This is due to the difference in properties exhibited between sp2 and sp3 carbon, as applications of NDs require their sp3 properties, and hence should contain as little sp2 as possible.

1.2 Carbon Nanotubes

1.2.1 Structure and Formation

CNTs, discovered in 1991, are an allotrope of carbon with an sp2 structure rolled along the Bravais lattice vector, which can be either single walled (SWCNTs) or multi walled (MWCNTs) [79]. While single wall carbon nanotubes (SWCNTs) consist of a single layer of sp2 carbon bonds, MWCNTs consist of multiple SWCNTs sticking in each other and bonded by van der Waals forces. SWCNTs can have a range of electrical properties depending on their wrapping direction (n,m), which also determines a parameter known as their chirality. Chirality, in chemistry, refers to a molecule which is not able to be superimposed on its mirror image. For CNTs, as mentioned previously, the chirality is determined by two values n and m written as (n,m), which denote both the orientation and diameter of the tubes with the chiral vector, C_h, which is given in terms of the primitive lattice such that

$$\vec{C_h} = n\vec{a}_1 + m\vec{a}_2,\tag{1.2}$$

as can be seen in Figure1.5. The chiral angle, which denotes the orientation of the nanotube, is then given by

$$\theta = \tan^{-1}(\frac{\sqrt{3}m}{m + 2n}),\tag{1.3}$$

This therefore gives information as to how the atoms in an unwrapped tube would line up with those in a graphene sheet, with SWCNTs of smaller n,m values having a smaller diameter the equation for which depends on whether the nanotube is chiral, or achiral. While chiral nanotubes are those where the chiral angle is $0° < \theta \leq 30°$ while also having $m \neq n$ and a diameter, d, given by

$$d = \frac{a_0\sqrt{(m^2 + mn + n^2)}}{\pi}\tag{1.4}$$

with a_0 being the length of vector a_1 [80], there are two forms of achiral nanotubes. These are known as zig-zag, where either m or n is 0 meaning $\theta = 0$ and the diameter is given by

$$d = \frac{a_0 m}{\pi},\tag{1.5}$$

and armchair where $m = n$ therefore denoted as (n,n) [81] and the diameter is given by

$$d = \frac{\sqrt{3}a_0 m}{\pi}.\tag{1.6}$$

The lattice structure for these achiral CNTs can be seen in Figure 1.5. While calculations of the charge carrier densities of achiral SWCNTs have been shown to be between 10^{22} and $10^{23}\,\mathrm{cm}^{-3}$, meaning the electrical conductivity of these tubes is similar to that of metals, a study looking at the bandstructures of nanotubes
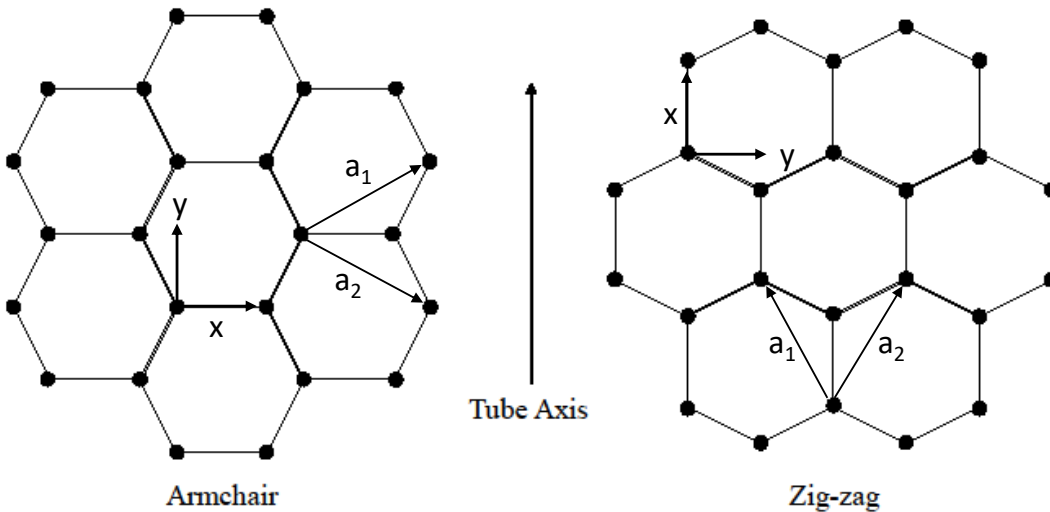
Figure 1.5: Lattice structures for both the armchair (Left) and zig-zag (Right) type achiral carbon nanotubes, with the tube axis going vertically from bottom to top of the figure. Based on Figure 12 in the paper by Sinnot et al. [81].

with a range of chiralities showed that SWCNTs can be split into three types, those with metallic properties, those with narrow bandgap semiconducting properties, and those with moderate bandgap semiconducting properties [82, 83]. A general rule in this regard is that, metallic CNTs will have a chiral index where $n = m$, while those with chiral indices of either $n \neq m$ or where $n - m$ is a multiple of 3 are narrow bandgap semiconductors. All others tend to be moderate band gap semiconductors. This broad range of electrical properties, as well as the tensile strength and thermal conductivity, make SWCNTs and MWCNTs very useful for a range of applications including many in biotechnology, such as in drug delivery, as biosensors, and in electrocardiography [84, 85, 86].

Methods for growth of CNTs include CVD, arc discharge, and high-pressure carbon monoxide disproportionation (HiPCO). Of these, CVD is the most common growth method as it allows for the most control over the growth procedure using C_2H_2 over an SiO_2-supported Fe catalyst. This method has been reported to produce uniform nanotubes with lengths up to 2 mm with very high purity [81]. HiPCO works by reacting CO with $Fe(CO_5)$ in a heated reactor, forming iron clusters which act as nucleation sites for SWCNTs. Optimal temperatures for SWCNT growth by this method are between 900°C and 1100°C, under pressures of around 30 atm to 50 atm, which provide growth rates of up to 10 g per day [87]. The oldest CNT production method is by arc discharge, which uses an electric current between two electrodes to produce temperatures of between 4000 K and 6000 K in order to generate a plasma from a gas. Carbon is then deposited onto the cathode after aggregating in the gas phase and drifting towards the cathode while cooling which form bundles of CNTs. Variations in the arc can result in impurities in the CNTs obtained, while adjusting the temperature allows for the growth of different diameter tubes [88].

1.2.2 Chirality Measurements of SWCNTs

An area of focus of current research is to find methods by which the chirality of nanotubes can be determined by optical microscopy. One metric by which this can

be determined is by the absorption cross section of the CNTs. Nanotubes with a chirality of (6,5) have been found to have an absorption cross section of around $1.7 \times 10^{-17} \, cm^2$ per C atom at a wavelength of 991 nm, using a combination of fluorescence and atomic force microscopy (AFM). This corresponds to an extinction coefficient of around $4400 \, M^{-1}cm^{-1}$ [89]. The absorption cross-section of the optical transitions for (6,5) SWCNTs has also been obtained using absorption microscopy, which found a value of $3.2 \times 10^{-17} \, cm^2$ per C atom [90]. Raman spectroscopy has also been used to characterise the chirality of SWCNTs. In 1997 a study focussed on armchair type SWCNTs which are non-chiral with chiral indices of (8,8), (9,9), (10,10), and (11,11). The first-order Raman active vibrational modes of the SWCNTs were measured and compared with those expected from theory, excited using five different laser wavelengths and powers. It was found that the observed peaks matched well with theory [91]. Raman breathing modes of semiconducting SWCNTs, ranging from 0.7 nm to 2.3 nm, have also been used to establish the dependence of tube chirality on their optical transitions. It was found that higher-order transitions scaled differently compared with the first (referring to transitions from the valence band to higher level conduction bands) and second order (referring to transitions from the valence band to lower level conduction bands) transitions due to a delocalised electron wave function [92]. Further measurements of the dependence of the diameter of SWCNTs on Raman breathing modes for a range of metallic and semiconducting SWCNTs have been carried out. These measurements found that the dependence of the tube diameter, d_t, and hence (n,m) on the frequency of the breathing modes is given by $\omega_{RBM} = A/d_t$, where A is a proportionality constant equal to $227 \, cm^{-1}nm$ which was determined to be in good agreement with the elastic properties of graphite [93].

1.3 Sizing Dielectric Nanoparticles

As has been discussed in Section 1.1 the uses of dielectric NPs, particularly NDs, have increased in recent years. With this comes the need to characterise the sizes of individual particles, especially for the medical field where NDs below 5 nm are required to enter cells [61]. This section provides a brief introduction to some of the methods that can be used to measure the sizes of dielectric NPs, from the currently established industry standard being electron microscopy, to scattering methods such as dynamic light scattering (DLS) and nanoparticle tracking analysis (NTA), as well as newer techniques including interferometric scattering (iSCAT), coherent bright-field (COBRI), optical extinction, and qDIC.

1.3.1 Electron Microscopy

The principle of accelerated electrons having an associated wavelength in the X-ray region of the electromagnetic spectrum dates back to 1924 and Louis de Broglie [94]. While this laid the foundations for the use of electrons for imaging, it wasn't until the later development of the electromagnetic lens which allowed for the focussing of electrons, which led to a prototype electron microscope being developed in 1931 [95]. There are three main types of electron microscopy, these being; transmission (TEM), scanning (SEM), and reflection (REM). The earliest of these to be developed was TEM, with the first commercial microscopes being produced by Siemens in 1939 [96]. TEM microscopes consist of an electron gun, producing a beam of electrons, which is collimated onto a specimen using condenser lenses to provide homogeneous

illumination. As with an optical microscope, this electron beam is then transmitted through the specimen to a series of objective and magnification lenses which project the image onto a detector [97]. REM works in a similar way, however, as the name suggests rather than being transmitted through the sample to a detector, the electron beam reflects off the surface of a specimen to the detector. SEM works differently in that, an electron gun and condenser lenses are used to produce focus on the sample, a deflection coil is used to deviate the path of the electron beam allowing for a raster scan pattern to be traced over the sample. An image can then be built up in one of two ways; by backscattered electrons, or by secondary electrons. The backscattered electrons are those which originate from the electron beam, and are elastically scattered back from the sample [98]. This detection modality is typically used to differentiate between areas with different chemical structures in samples due to the proportion of backscattered electrons being dependant on the atomic weight of elements. Secondary electrons, on the other hand, are produced by inelastic scattering of the incoming electrons by electrons in the sample, which after single or multiple scattering exit the sample, typically at low energies (below $50\,\text{eV}$) from the sample causing electrons to be released from the atomic structure of the sample. These secondary electrons are attracted by a low voltage and then accelerated and detected by a scintillator and photomultiplier, an arrangement called an Everhart-Thornley detector [99]. Both SEM and TEM have been used in the past to obtain the size and shape of nanometre sized particles and objects, having maximum resolutions of a few nm and $< 0.1\,\text{nm}$ respectively, with these techniques becoming the industry standard when characterising nanoparticles [100, 101, 102].

While there are a number of key drawbacks to these techniques, including cost and the need for a vacuum for measurements, one of the key issues is expertise required to effectively utilise electron microscopy. Particularly for SEM, sample preparation can be a limiting factor when it comes to usability due to the lack of standardised practice. While there are some efforts at standardisation, one such method shows the complexity involved, with spin coating of the sample onto a silicone wafer substrate for measurements to avoid aggregation of NPs being measured. This technique, however, requires understanding of the pH, zeta potential, and concentration, among other metrics of the sample material and dispersant in order to obtain statistically reliable results [103]. For SEM it is also necessary to have a conductive sample, as the technique requires a high electron density, therefore dielectric samples need to be coated with a conductive material prior to measurements. For TEM, the drawbacks are less due to difficulty and primarily based on cost of the equipment required.

1.3.2 Dynamic Light Scattering and Nanoparticle Tracking Analysis

Another technique often considered an industry standard is DLS. The setup of this technique is simple, with a laser shone onto a cuvette containing a dispersion of the sample, with the interference in the scattering of the light from different particles in the sample on a detector being used to determine their sizes. Determination of particle size using this technique exploits the Brownian motion of the particles, which gives information about their diffusion coefficient, and hence using the Stokes-Einstein equation the hydrodynamic radius of the particles can be calculated [104]. As with electron microscopy, DLS comes with a number of unique drawbacks. A key issue with this technique is the response to large particles arising due to the

dependence of Rayleigh scattering intensity increasing with the sixth power of the particles diameter, $I \propto d^6$. This means that, for measurements of nanoparticles, just a small number of relatively large particles can dominate over the signal of the sample intended to be measured [105]. Depending also on the characteristics of the particles being measured, such as surface charge, the hydrodynamic radius can overestimate the true radius of the particles as it can be measuring both the particle and water molecules bonded around it.

Initially made commercially available in 2006, NTA can overcome some weaknesses of DLS by utilising the Brownian motion of individual NPs to determine their trajectories and hence size. The technique typically uses a charge coupled device (CCD) camera to image the scattered laser light from the individual NPs, rather than from an ensemble as with DLS, and from the equation

$$(x, y)^2 = \frac{2k_B T}{3r_h \pi \eta} \tag{1.7}$$

where k_B is the Boltzmann constant, T is the temperature, $(x, y)^2$ is the mean squared displacement per time of the particle, and η is the medium viscosity, the hydrodynamic radius, r_h, can be determined [106]. Measurements of gold NPs down to 30 nm size have been carried out using NTA, while dielectric polystyrene (PS) beads of 60 nm can also be measured using this technique [107]. While these experiments have showed that small amounts of large particles, around 1000 nm size, mixed in with the sample does not affect the ability of NTA to accurately size dielectric NPs down to 60 nm in size, there are still limitations to the technique. Typically these limitations arise due to the refractive index of the sample particles being too similar to that of the dispersion medium, as well as large amounts of background signal from highly polydisperse samples as with DLS, therefore, sample preparation is still important to obtain accurate size measurements for NPs [108].

1.3.3   iSCAT and COBRI

The two techniques known as iSCAT and COBRI microscopy are both based around the principle of elastically scattered light from particles interfering with incident light. The difference comes down to where this interference occurs, with iSCAT being the scattered light interfering with incident light reflected from the interface between the glass and the mounting medium, while in COBRI interference occurs with transmitted incident light [109]. The first measurements of biomolecules using iSCAT were conducted in the early 90's to measure the bending of sliding microtubules [110]. Subsequently, iSCAT has been used for a broad range of applications such as label free imaging and detection, and particle tracking [111, 112]. Mass photometry, which uses scattering to obtain label free measurements of the masses for individual biomolecules [113], has also been carried out using iSCAT, providing high resolution and precise measurements [114].

Similarly, COBRI has also been utilised to track single nanoparticles, with both single metallic and dielectric nanoparticles being tracked using the technique. The authors of a study published in 2019 reported the ability to track single gold nanoparticles of 10 nm labelled to lipid molecules, as well as the ability to track dielectric silica nanoparticles with sizes of 50 nm and 100 nm with a sensitivity limit of around 30 nm [115].

Statistical analysis of both iSCAT and COBRI has since been carried out in order to obtain values for the lower bounds of the sensitivity for both techniques.

It was determined that iSCAT provided better axial localisation precision, which was expected to be due to the relative phase accumulated between the reference and signal fields being larger than for that with COBRI. However, for mass spectrometry, it was found that there was no difference in the sensitivities achieved by the two techniques due to these measurements relying less on phase change [109].

1.3.4   Optical Extinction Microscopy

Optical extinction occurs when light travels through a medium causing attenuation of the beam. This attenuation can be due to scattering (σ_{scat}) and absorption (σ_{abs}) from the medium, which add together to give the extinction cross section, given by the equation [116, 117]:

$$\sigma_{\mathrm{ext}} = \sigma_{\mathrm{abs}} + \sigma_{\mathrm{scat}}. \tag{1.8}$$

Given in units of area (typically nm^2), the extinction cross section thus describes the area that, when multiplied by the incident intensity, gives the power scattered and absorbed by a NP [118].

There are currently a number of techniques by which one or more of these cross sections can be found for individual NPs, the most common of which is dark field scattering microscopy [119]. This technique works based on the scattered light from NPs being detected against a dark background, and given its simplicity the technique has been used extensively for a range of applications including single particle tracking and measurements of NP morphology [120, 121]. It is, however, difficult to recover the quantitative scattering cross section from this method as all aspects of the optical setup, as well as particle size and shape, must be understood for this to be done [122, 123]. Other techniques such as near field microscopy can also be used to determine quantitative information about the scattering from nanoparticles. Near field methods use the nano-antenna effect, wherein subwavelength size NPs confine and enhance the electromagnetic field thus boosting the excitation rate and emission intensity [124]. Information of the phase of the scattered light can then be collected, which when analysed gives information for the local surface plasmon resonance for metallic nanoparticles. This has previously been used to measure the plasmon resonance of single gold nanoparticles [125]. While the above techniques can provide quantitative measurements of the scattering and extinction cross sections, they are unable to provide measurements for the absorption cross section of materials unless that for the scattering from materials is sufficiently small such that the extinction cross section is approximately equal to the absorption cross section [119].

Methods to determine the absorption cross section are typically non-linear, with the most common being photothermal methodologies. The principle of photothermal lensing and microscopy are discussed further in Section 1.5, however, they are used here due to there being no contribution to the signal due to direct scattering from the sample material which is useful for measurements on biological samples [126]. There is however, scattering from the photothermal lens produced. These techniques have been used to measure the absorption of gold NPs down to a size of 1.4 nm, and have been shown to be capable of measuring single NPs with absorption cross sections of less than 1 nm^2 [127].

A technique by which the extinction cross sections of single NPs can be measured has also been developed by Payne, et al. in 2013. In this technique, transmission images of gold NPs with sizes of 40 nm and 100 nm were obtained using wide field

microscopy. Defocussed images and background images were also obtained. These images were then used to derive the relative transmission image contrast $\Delta = (I_d - I_f)/I_d$ and from this the local background $\Delta_b = A_b^{-1}\int_{A_b}\Delta dA$, where I_d was the defocussed intensity, I_f was the focus intensity, and A_b was the area over which a spatial integration was calculated for the local background. From this the extinction cross section could be calculated using the equation

$$\sigma_{ext} = \int_{A_i}(\Delta - \Delta_b)dA, \tag{1.9}$$

where A_i was the area over which the integration was carried out to obtain the signal from the analysed particle, the radius of which was half that of A_b which encompasses the disk between r_i and r_b. It was concluded that this technique provided a viable way to obtain quantitative information regarding the extinction cross section of a nanoparticle using conventional wide field microscopy, with a sensitivity on the order of $100\,\mathrm{nm}^2$ [128]. In 2018, a method by which the sensitivity of this technique could be improved was developed. By using a lateral shift, rapid reference method 25,600 frames could be obtained in 1 minute when a frame rate of $400\,\mathrm{Hz}$ was achieved. Here the lateral shift was used rather than an axial shift to ensure the local background of the particles was not affected by artefacts possibly present at other focal positions while the rapid shifting reduced any background caused by the stage drifting during measurements. Consequently, the large number of averages provided by this method allowed for a much higher sensitivity to be obtained. This improved sensitivity has been demonstrated during measurements of $5\,\mathrm{nm}$ GNPs, wherein the background was measured in the same way as the particles and showed a signal equivalent to that which would be observed from a NP with an extinction cross section of $0.4\,\mathrm{nm}^2$ [129]. Further, this extinction protocol has been used to determine the absorption cross section of GNPs and hence determine the shape of the NP, be it a nanorod or sphere. To do this a combination of brightfield and darkfield measurements were obtained for individual particles, which gave the extinction and scattering cross sections, respectively. Equation 1.8 could then be used to calculate the absorption cross section of each particle [130].

1.3.5 Differential Interference Contrast Microscopy

Quantitative phase contrast techniques provide label free methods by which biological samples can be imaged, and as such have gained popularity in recent years. There are a number of methods available to obtain quantitative phase contrast measurements, such as transmission of intensity, ptychography, and differential phase contrast, among others [131]. The transmission of intensity equation (TIE) was first proposed in 1983 by Michael Teague as a way to computationally reconstruct the phase of a wave in optical microscopy [132, 133]. In recent years, this phase reconstruction technique has been applied to measurements of algal samples obtained using a cheap open source 3D printed microscope to distinguish between different species as well as non-biological samples [134]. Similarly, ptychography is another computational technique, however this uses coherent interference patterns from the scattering of light off of microscopic objects to generate images [135]. Due to the versatility of this phase reconstruction technique, it has been combined with the use of an electron microscope to obtain sub angstrom resolution of 2D materials [136]. One common method of differential phase contrast technique, and the one presented in this thesis due to its accessibility, is DIC.

DIC microscopy was developed in 1952 by Georges Nomarski [137], and makes use of interferometry to obtain information about the phase contrast of a material. This is made possible by the use of a modified Wollaston prism to convert the detected optical gradients in materials into an intensity difference. As with CARS microscopy of NDs, discussed in Section 1.1.5, nanodiamonds have been imaged using phase contrast techniques such as DIC and Hoffman modulation contrast (HMC) microscopy both inside of cells and on their own [138]. This gives evidence that large NDs can be used as optical scattering labels in cells without the need for colour centres or fluorescing molecules on the surface of the NDs. This technique however, is not inherently able to provide quantitative insight into the size of nanoparticles, though there are methods using further equipment and in depth analysis that can be used to recover this quantitative information. In 2008, a technique using a structured aperture wavefront sensor was developed. It was reported that by using this technique the amplitude and phase gradient data could be separated, providing a resolution of $2\,\mu$m and allowing for the imaging of birefringent samples [139]. Another method by which quantitative information can be resolved from DIC images is integrating phase-shifted DIC images in Fourier space. By using this method a minimum phase contrast of 0.25 radians was observed [140, 141]. Further, in a technique developed by McPhee, et al., quantitative information could be recovered using Wiener deconvolution and filtering (further information on this technique can be seen in Section 2.2.2). This technique has been used previously to obtain quantitative information about primarily biological samples, such as measuring the lamellarity of giant lipid vesicles [142], and measuring the thickness of lipid bilayers with 0.1 nm precision [143]. This method has also been shown to be able to provide measurements for thickness changes in lipid bilayers of around 1 nm [144]. Dielectric particles have been investigated using this technique, as a way to obtain measurements for the volume of nanodiamonds in order to obtain a quantitative relationship between nanodiamond size and CARS signal strength, as mentioned previously in Section 1.1.5 [78]. However, to date, no comprehensive calibration of this qDIC method has been shown for dielectric particles, nor has there been any calibration of the sensitivity limit. Therefore, an in depth calibration of this method for imaging dielectric particles has been carried out and is reported in Chapter 3. This allows for accurate size measurements of dielectric particles such as nanodiamonds to be carried out in future experiments without the need to recalibrate the technique for each measurement.

1.4   Raman Scattering

1.4.1   Background Knowledge

In 1928, after a series of observations of liquids including methanol, ethanol, and ether, C. V. Raman published work on a new type of scattering, known now as Raman scattering [145]. In the same year, this same effect was independently observed in quartz crystals [146]. Unlike Rayleigh scattering, which is elastic, Raman scattering is an inelastic scattering of photons from a molecular structure, which can be categorised further into Stokes and anti-Stokes. Stokes Raman scattering occurs when an incident photon is scattered off of a material losing an amount of energy ($h\nu$), which is correspondingly gained by a molecular vibration. In anti-Stokes Raman scattering, the opposite occurs whereby a photon scattered from a

material gains energy and a molecular vibration correspondingly loses energy [147]. An example of Rayleigh, Stokes Raman, and anti-Stokes Raman scattering can be seen in Figure 1.6 using a quantum mechanical picture and an energy level diagram, whereby no real electronic transitions need to be involved. This Raman effect is used extensively to identify materials using a technique known as Raman spectroscopy [148]. Measurements of the Raman spectra for both sp3 and sp2 carbon were carried out independently in 1969. In a study by S. A. Solin and A. K. Ramdas, the first-order (between 1000 and 1700 cm^{-1} involving a single phonon transition) and second order (between 2300 and 3300 cm^{-1} involving a two phonon transition) Raman spectra of diamond were investigated using both an Ar ion and He-Ne lasers. It was concluded that the first-order Raman spectrum showed a single sharp peak at 1332 cm^{-1} [149, 150]. Similarly, an experiment was conducted to find the Raman peaks of both single crystal graphite and polycrystaline graphite by F. Tuinstra and J. L. Koenig, using an Ar ion laser. They found that there are two first order peaks associated with graphite, the first being a peak at 1575 cm^{-1} which was associated with the single crystal graphite (known as the G peak), and the second occuring at 1355 cm^{-1} was associated with the polycrystaline graphite (known as the D peak) [151]. Second order Raman modes have also been studied for carbonaceous materials, providing information about the vibrational states throughout the Brillouin zone as opposed to first-order Raman modes which only contain vibrations at the Γ point [152]. A number of second order peaks have been attributed to diamond in the past, with early observations recording 10 distinct peaks ranging from 2176 cm^{-1} to 2666 cm^{-1} [153]. More recent observations of synthetic HPHT grown microdiamonds have shown a second order resonant peak at 2619 cm^{-1} [154]. There are currently a number of different techniques which exploit Raman scattering. In particular, beyond spontaneous linear Raman scattering, coherent non-linear Raman has attracted significant interest, in the form of coherent anti-Stokes Raman scattering CARS, and stimulated Raman scattering (SRS) [155]. Interest in these techniques has arisen due to the weak response that spontaneous Raman scattering provides, with signals typically having a cross section per illuminated area of between 10^{-6} and 10^{-7}. This is due to the modulation of the refractive index by phonons being very small compared to the resonant excitation of electrons during absorption, and depends on the orientation of the crystal relative to the polarisation of the incident light [149].

1.4.2 Stimulated Raman Scattering

Stimulated Raman scattering (SRS) was first observed accidentally in 1962 during an experiment, conducted by Woodbury and Ng, in which nitrobenzene was introduced to a ruby crystal, causing a strong emission to be seen other than that expected at 694.3 nm from the laser. While initially mistaken for fluorescence, it was later shown to have been caused by a higher order photon process [156]. Unlike spontaneous linear Raman scattering, which is a single photon process, SRS is a three photon process (third order non-linearity), whereby a pump photon with frequency, ω_p, excites a material to a virtual energy state (as in Figure 1.7) while a second beam known as the Stokes beam, which is temporally and spatially synchronised with the pump beam, is used to stimulate relaxation of the system to the vibrational excited state, E_2. The frequency of this Stokes beam is given as ω_s, with the difference between the pump and Stokes frequencies being that of the vibration energy gap,
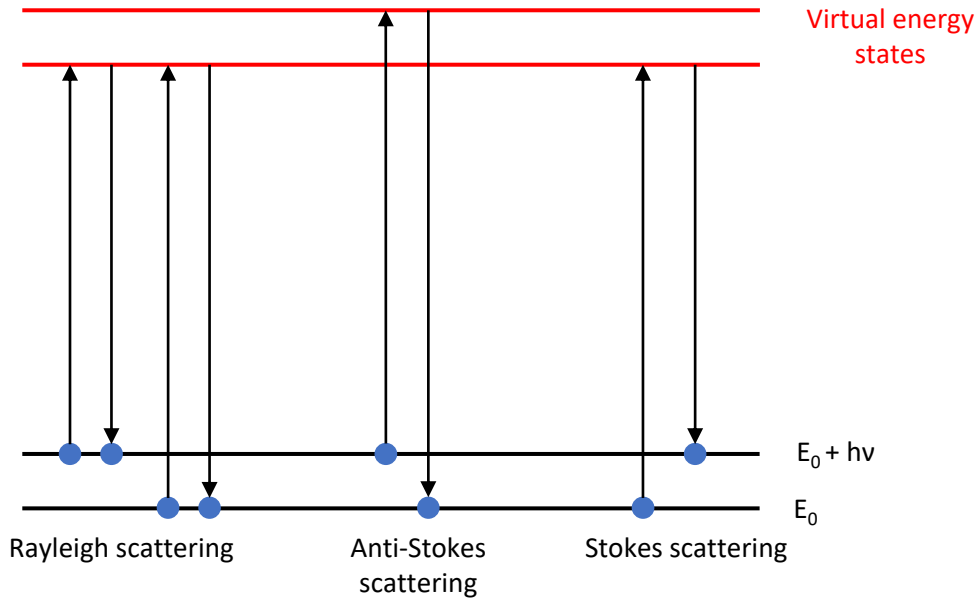
Figure 1.6: Diagram showing Rayleigh (Left), anti-Stokes (Centre), and Stokes scattering (Right) using a quantum mechanical energy level diagram, with vibrational energy levels (E_0 and $E_1 = E_0 + h\nu$) and virtual electronic states.

ω_v, between E_1 and E_2

$$\hbar\omega_v = \hbar(\omega_p - \omega_s). \tag{1.10}$$

This process results in a loss of pump intensity, while simultaneously resulting in a gain in Stokes intensity [157]. Therefore, measurements of signal in SRS microscopy can either be of a gain in stokes power, known as stimulated Raman gain (SRG), or as a loss of pump power known as stimulated Raman loss (SRL) [158]. As such, the main benefit of using SRS is that the efficiency of the weak Raman interaction is increased [159].

As well as its benefits over spontaneous Raman scattering, SRS also offers benefits over CARS microscopy. Particularly as it is background free (as discussed in Section 1.4.3) and provides a chemical contrast which is simple to interpret making it ideal for imaging biological samples. In this area it has been used to successfully differentiate between healthy tissue and tumours, with in vivo experiments conducted on mice showing SRS to be more effective at determining tumour margins than conventional white light illumination, correlating well with histopathology [160].

1.4.3   Coherent Anti-Stokes Raman Scattering

CARS is a wave mixing technique which, similarly to stimulated Raman scattering (SRS), makes use of a pump and Stokes beam to obtain a vibrational contrast equal to the difference between the pump and Stokes frequencies. The first step of this process is exactly as with SRS, with the pump and Stokes beam acting as in Figure 1.7. However, following this, the sample is once again pumped to a higher virtual state from which the molecules 'relax' back to the molecular ground state producing an anti-Stokes signal, as with the anti-Stokes interaction seen in the left panel of Figure 1.8. As alluded to previously, one disadvantage of this technique over SRS is that it has a larger background signal. During CARS measurements, it is possible to
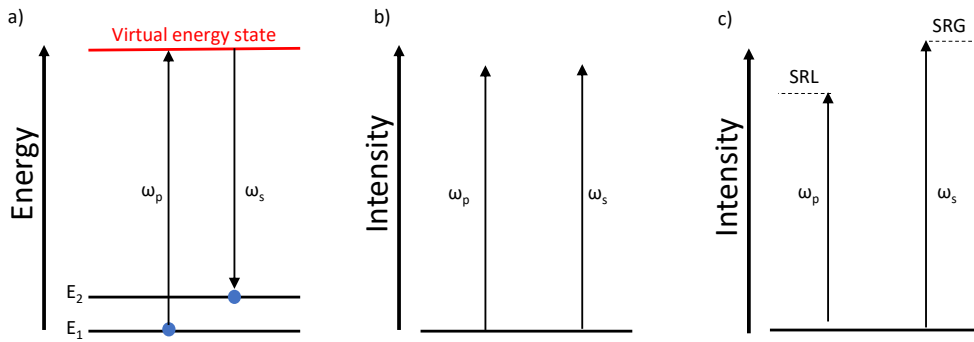
Figure 1.7: (a) Quantum mechanical energy level diagram showing the excitation to a virtual energy state caused by the scattering of the pump photon (ω_p) to a Stokes photon (ω_s) from a molecule, with vibrational energy levels E_1 and E_2 separated by $\hbar\omega_v$. (b) Input power of the pump and Stokes beams. (c) Output from SRS scattering showing a decrease in pump power representing SRL, and the increase in the Stokes power representing SRG.

obtain a non-vibrationally resonant background (NVRB) the process for which can be seen in the right panel of Figure 1.8. It is worth noting that, if the virtual energy state seen in this figure is near to a real electronic energy level, this interaction can become a resonant four wave mixing process for which the signal is very strong. These NVRB interactions occur when the anti-Stokes frequency, ω_{as}, is given by [161]

$$\omega_{as} = 2\omega_p - \omega_s. \tag{1.11}$$

One particular benefit of CARS, and SRS, over spontaneous Raman scattering in particular, is that the signal is enhanced by several orders of magnitude. This is due to the coherent nature of the induced vibrations, whereby atoms oscillate with the same phase [162].

Due to the strong signal obtained from CARS measurements, it is possible to carry out label free measurements of single nanoparticles. As has previously been discussed in Section 1.1.5, one such experiment showed that single nanodiamonds, without the presence of fluorescent NV centres, were observed using a CARS setup. It was shown that, not only could single non-fluorescent NDs be observed using CARS, but by making use of correlative qDIC, sizing of the NDs was also possible using CARS with the smallest detectable particles having a size of 27 nm. This was taken further, with quantitative CARS measurements of NDs being obtained in HeLa cells, showing the possibility of tracking non-fluorescent dielectric NPs in biological tissue [78].

1.5 Photothermal Microscopy

The photothermal effect was first reported on in depth in 1965 and made use of a Raman scattering setup to investigate the heating effect of a laser on liquid and solid samples. The authors concluded that localised heating around the laser beam of the samples caused a lensing effect due to a refractive index gradient across the sample [163]. In 1976 a new absorption spectroscopy technique based on thermal lensing (photothermal effect) was developed. The experiment for which this technique was reported measured the temperature increase of liquids when illuminated
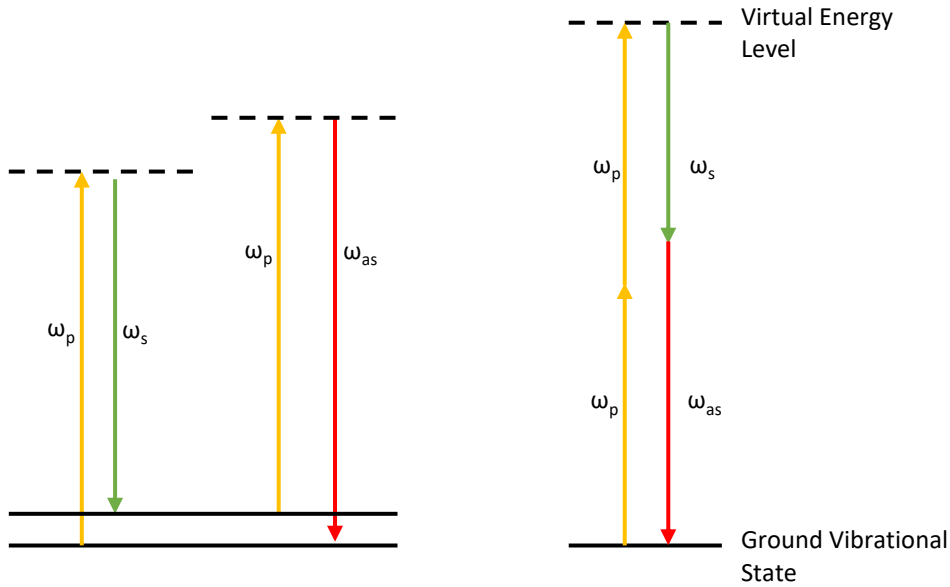
Figure 1.8: Quantum mechanic energy level diagram showing the CARS process (left) and the NVRB interaction (right). Excitation to a virtual energy state in both cases is caused by the scattering of two pump photons (ω_p) to a Stokes and anti-Stokes photon (ω_s) with the molecule relaxing back to the ground state.

using both a single laser beam, and a dual laser beam. The results showed accurate values for the C-H stretching vibrations, as well as measurements for the absorption of anthracene which matched well with previously obtained measurements [164]. More recently, the photothermal effect of NPs such as gold nanoparticles (GNPs) both with and without graphene coatings have been investigated under near infrared illumination. It was found that the graphene coated GNPs showed enhanced photothermal effects [165]. The photothermal effect has been applied to optical microscopy, leading to a number of photothermal microscopy techniques. An initial proposal for photothermal microscopy measurements of absorbing nanoparticles was published in the 1990's, and subsequently used to detect individual nanometre sized NPs [166]. Advancements in the technique were reported in 2006, with a heterodyne photothermal method developed and used to image individual silver NPs. Further discussed was the theoretical ability of the technique to obtain absorption spectra for gold NPs [167]. Beyond simple detection of particles, photothermal microscopy has been shown to be a viable method for the tracking of NPs by a technique known as single nanoparticle photothermal tracking (SNaPT). To do this, laser induced scattering was utilised around nano-absorbing materials allowing for the detection of 5 nm gold beads in live cells [126]. Further, investigations into dielectric nanoparticle have also been carried out using photothermal microscopy, which allowed for sizing of aggregated and non-aggregated NDs [168].

Photothermal artefacts have been observed in SRS measurements, appearing as an enhanced background signal, due to this being a third order non-linearity with a second order heating process and a third order transmitted field. During such measurements, the Stokes beam can be absorbed by the sample which can induce a thermal lensing effect around the particle. This in turn causes a change of divergence of the pump beam, hence creating an SRL signal detected due to aperture

clipping [169]. Artefacts have been observed in measurements of polystyrene beads, and more recently in gold [170, 171]. Practical use of photothermal lensing during SRS measurements include detection of trace gases, most notably hydrogen, with sensitivities of 9 parts in 10^6 [172]. In this report, the principle of photothermal lensing observed during SRS measurements is applied to the determination of sp2/sp3 ratios in single NDs.

1.6 Motivation

The main motivation for this project was to develop new optical microscopy methods to quantify the sp2/sp3 ratio in individual nanodiamonds and to measure the morphometric characteristics, specifically (n,m), of individual carbon nanotubes. As discussed in the previous section, it has been shown that NDs have potential applications in a variety of fields with particular focus on medical applications. To that end, a quantitative knowledge of the the sp2 carbon content of individual NDs is important due to the increased cytotoxicity of sp2 carbon based materials compared to that of sp3 carbon, as discussed in Section 1.1.5. The presence of sp2 carbon in the diamond lattice also increases the tendency of diamonds relaxing to graphite during laser scanning imaging. Current methods to obtain the ratio of sp2 to sp3 carbon in individual NDs are limited in capability, as discussed in Section 1.1.4. The main aim of this project was to develop a method by which the sp2/sp3 ratios of single NDs could be measured accurately and with high sensitivity, this was accomplished using a combination of three optical microscopy techniques. Calibration of the qDIC method for dielectric NPs was carried out which allowed for accurate sizing of single NDs. Correlative photothermal and qDIC measurements of NDs provided an understanding of the sp2 content of individual NDs which is absorbing light and thus generating a photothermal effect, however initially these were qualitative measurements and required a calibration of the response. Photothermal measurements were carried out using an SRS setup (described in Section 2.4.1). Subsequent correlative extinction and photothermal measurements of graphene were conducted to calibrate the response of the photothermal method for a pure sp2 sample, and hence obtain quantitative measurements for the sp2/sp3 ratios of individual nanodiamonds. It is worth noting that, obtaining the ratio from optical extinction alone would not be possible due to the significant light scattering from NDs. Therefore, it was necessary to measure the absorption due to sp2 free of the dielectric sp3 background separately from the sp3 response free of the sp2 absorption background.

Further to this, (n,m) measurements of SWCNTs using extinction microscopy based on conventional wide field microscopy were carried out. As discussed in Section 1.2.2, current methods to determine the chiral index of nanotubes require Raman spectroscopy, or a combination of other techniques such as fluorescence microscopy and AFM. As part of this project, optical extinction microscopy using a wide field microscope setup was planned to be carried out on SWCNTs of both known and unknown chiralities. The aim of this was to provide quantitative measurements of the chirality of SWCNTs using a conventional wide field microscope. However, due to time restrictions, brought about by the Coronavirus pandemic, these measurements were not completed. In this thesis, the initial sample preparation and experimental results are presented in Chapter 5.

Chapter 2

Samples and Methods

2.1 Samples

2.1.1 Hydrogen Peroxide Glass Cleaning

The hydrogen peroxide cleaning method used for all coverlips and slides during this work was developed previously. This method involves initially wiping the glass surfaces with clean room wipes, after which coverslips and slides were immersed in toluene while being sonicated for 20 minutes, followed by immersion in acetone and again being sonicated for 20 minutes. They were then immersed in water and boiled for 3 minutes, before finally being immersed in hydrogen peroxide and sonicated for a final 20 minutes. The coverslips and slides could then be left immersed in hydrogen peroxide in a refrigerator until required.

2.1.2 Polystyrene Beads

PS beads with $200\,\mathrm{nm}$ diameter and 3% coefficient of variance (cv) (Alpha Nanotech) were used to calibrate the qDIC analysis. PS bead samples were dispersed in DI (deionised) water to a concentration of $4{\times}10^9$ particles/ml, and drop cast onto $24 \times 24\,\mathrm{mm}$ #1.5 Menzel Gläser glass coverslips which had been cleaned using the hydrogen peroxide cleaning protocol described in Section 2.1.1. Once dried using a hot plate at $60°$C with the samples covered, $20\,\mu$l of the chosen mounting medium was pipetted onto the coverslip and then degassed for 10 minutes to remove and slow down the future formation of air bubbles from the oil. As mounting medium, silicone oil (with refractive index, $\mathrm{n}, = 1.518$) (Sigma Aldrich, AP 150 Wacker) or water immersion oil ($\mathrm{n} = 1.334$) (Zeiss, Immersol W 2010) were used. Once degassed, the sample coverslips were mounted on slides with the immersion medium between them, which had also undergone the hydrogen peroxide cleaning procedure, and sealed using clear nail varnish. Prior to being sealed, any mounting medium that had been squeezed out from under the coverslip was cleaned using cleanroom wipes.

In order to show the precision and sensitivity of the qDIC technique, samples similar to those of the $200\,\mathrm{nm}$ PS beads were prepared using fluorescing $30\,\mathrm{nm}$ diameter PS beads (Sigma Aldrich, L5155) with fluorescence excitation and emission peaks at $470\,\mathrm{nm}$ and $505\,\mathrm{nm}$, respectively (as seen in Figure 3.24).

2.1.3   Graphene

For calibration of the photothermal response to pure sp2 samples, nominally $500\,nm$ sized pristine graphene flakes (PGFs, Graphene Supermarket) dispersed in ethanol were used. The PGFs were diluted in ethanol to a concentration of 10^{12} particles/ml before being drop cast onto a $24 \times 24\,mm$ #1.5 Menzel Gläser glass coverslip cleaned using the hydrogen peroxide cleaning protocol. $20\,\mu l$ of silicone oil ($n = 1.518$) was then pipetted onto the coverslip, which was subsequently mounted on a hydrogen peroxide cleaned slide, with the coverslip and slide being squeezed together by hand. The edges were then sealed using clear nail varnish.

2.1.4   Nanodiamonds

ND samples, grown using high pressure high temperature (HPHT) synthesis and milled to sizes of 0-50 nm, 0-150 nm, and 0-250 nm (Nanodiamant MSY 0-$0.05\,\mu m$, 0-$0.15\,\mu m$, and 0-$0.25\,\mu m$) were used as samples to determine sp2/sp3 ratios of single NDs. For each size range, a treated and untreated sample was prepared. Treatment of the nanodiamond samples was carried out previously by Ryan Lewis (a postgraduate student at Cardiff University). Treatment consisted of etching the samples using sulfuric acid, nitric acid, and piranha solution for 2 hours before air annealing was carried out at 600°C for 6 hours. Each of the nanodiamond samples were dispersed in water to desired concentrations, which were pipetted onto hydrogen peroxide cleaned $24 \times 24\,mm$ #1.5 Menzel Gläser glass coverslips, before being mounted in silicone oil ($n = 1.518$) on a hydrogen peroxide cleaned slide and sealed using clear nail varnish.

2.1.5   Carbon Nanotubes

SWCNTs of which $> 40\%$ had a chiral index of (6,5), while the remaining $\leq 60\%$ was not defined by the manufacturer, and a mean diameter of $0.78\,nm$ (Sigma Aldrich) were used for extinction measurements, in order to calibrate the technique for obtaining the chiral index of CNTs. For this the samples were dispersed in water using a SWCNT water dispersant (US Research Nanomaterials) and wet cast onto hydrogen peroxide cleaned $24 \times 24\,mm$ #1.5 Menzel Gläser glass coverslips, as discussed further in Section 5.2. In order to find the sample plane during setup for the extinction measurements, 50 nm gold nanoparticles dispersed in water at a concentration of 4×10^9 particles/ml were spin coated onto the sample surface after the CNTs had been wet cast. The samples were then mounted in silicone oil ($n = 1.518$) on a hydrogen peroxide cleaned slide and sealed using clear nail varnish.

2.2   qDIC Microscopy

2.2.1   Setup

In order to obtain DIC images of the PS bead and ND samples, an inverted Nikon Ti-U microscope was used with a Hamamatsu Orca 285 CCD camera (with 18,000 electrons full well capacity, 7 electron read noise, [and at minimum gain used throughout] 4.6 electrons per count and 192 counts offset, 12 bit A/D converter) which produced images of 1344×1024 pixels with pixel size of $6.45\,\mu m$. In order to laterally and axially position the sample relative to the objective, a Prior Proscan III with a stepper motor driven x-y stage ($0.04\,\mu m$ step size), and an objective focus drive (2

nm step size) were used. For transillumination, a Nikon 100 W tungsten halogen lamp (Nikon V2-A LL 100 W) was used with a Schott BG40 filter used to remove wavelengths above 650 nm as the DIC polarisers are not suited to wavelengths above this, and a Nikon green interference filter (GIF) to produce light with a peak emission wavelength of 550 nm and a full width at half maximum (FWHM) of 53 nm. Light then passed through a de Sènarmont compensator (a rotatable linear polariser followed by a quarter-wave plate, Nikon T-P2 DIC Polariser HT MEN51941) and a N2 Nomarski prism (Nikon N2 DIC module MEH52400 or MEH52500 used for the dry condenser and oil condenser, respectively). In this setup, the angle between the linear polariser used in the de Sènarmont compensator and the fast axis of the wave plate, θ, could be controlled such that at $\theta = 0°$ the light was linearly polarised along the fast axis of the wave plate meaning linearly polarised light exited the compensator, for most other cases of θ the light exits the compensator elliptically polarised. The light was then focussed onto the sample using either a dry or a high numerical aperture (NA) oil-immersion condenser, depending on the objective used to ensure NA matching as much as possible. The dry condenser (0.72 NA, MEL56100) was used for the $20\times$ 0.75 NA, (MRD00205) dry objective in conjunction with a 1.5x tube lens, while the high NA oil condenser (set to either 1.27 NA or 1.34 NA, MEL41410) was used with the $60\times$ 1.27 NA (MRD70650) water immersion objective and the $100\times$ 1.45 NA (MRD01905) oil immersion objective. The maximum NA of the oil condenser of 1.34 NA was used for the 1.45 NA objective. Prior to the tube lens, light passed through a second Nomarski prism (DIC sliders MBH76220, MBH76264, and MBH76190 used for the 0.75 NA, 1.27 NA, and 1.45 NA objectives, respectively), and another linear polariser (Nikon Ti-A-E DIC analyser block MEN 51980) referred to as the analyser, before passing through the tube lens and to the camera. This setup can be seen in Figure 2.1 below. For each sample, stacks of 256 images were obtained at positive and negative polariser angles, with the linear polariser used in the de Sènarmont compensator being rotated to provide these angles as mentioned previously, with a 120 ms exposure time per image and 0 ms delay between images. The lamp intensity for each stack was set to result in an average of around 2900 counts on the camera, to avoid saturation while being close to the FWC to minimise shot noise.

2.2.2 Recovering Quantitative Phase Information

The technique used to recover quantitative phase information about a sample, developed previously and initially reported on by McPhee, et al. [142] uses light, with a peak wavelength of 550 nm, passed through a de Sènarmont compensator (as described in Section 2.2.1) which allows the angle between the fast axis of the waveplate along the direction (1,1) and the polariser, θ, to be adjusted to control the polarisation state of the light. This can be shown by the Jones vector equation

$$\vec{E} = E_0 \frac{1}{\sqrt{2}} \begin{pmatrix} 1 \\ e^{i2\theta} \end{pmatrix} \tag{2.1}$$

where $\vec{E}$ is the electric field vector, and E_0 is the field amplitude. Using this setup, when $\theta = 0$ the light is linearly polarised along the diagonal (1,1), which is also the fast axis of the quarter waveplate. While in general the light is elliptically polarised, at angles of 90 and 180 degrees it is linearly polarised and at 45 degrees it is circularly so. The first Nomarski prism shown in Figure 2.1 consists of two birefringent crystals
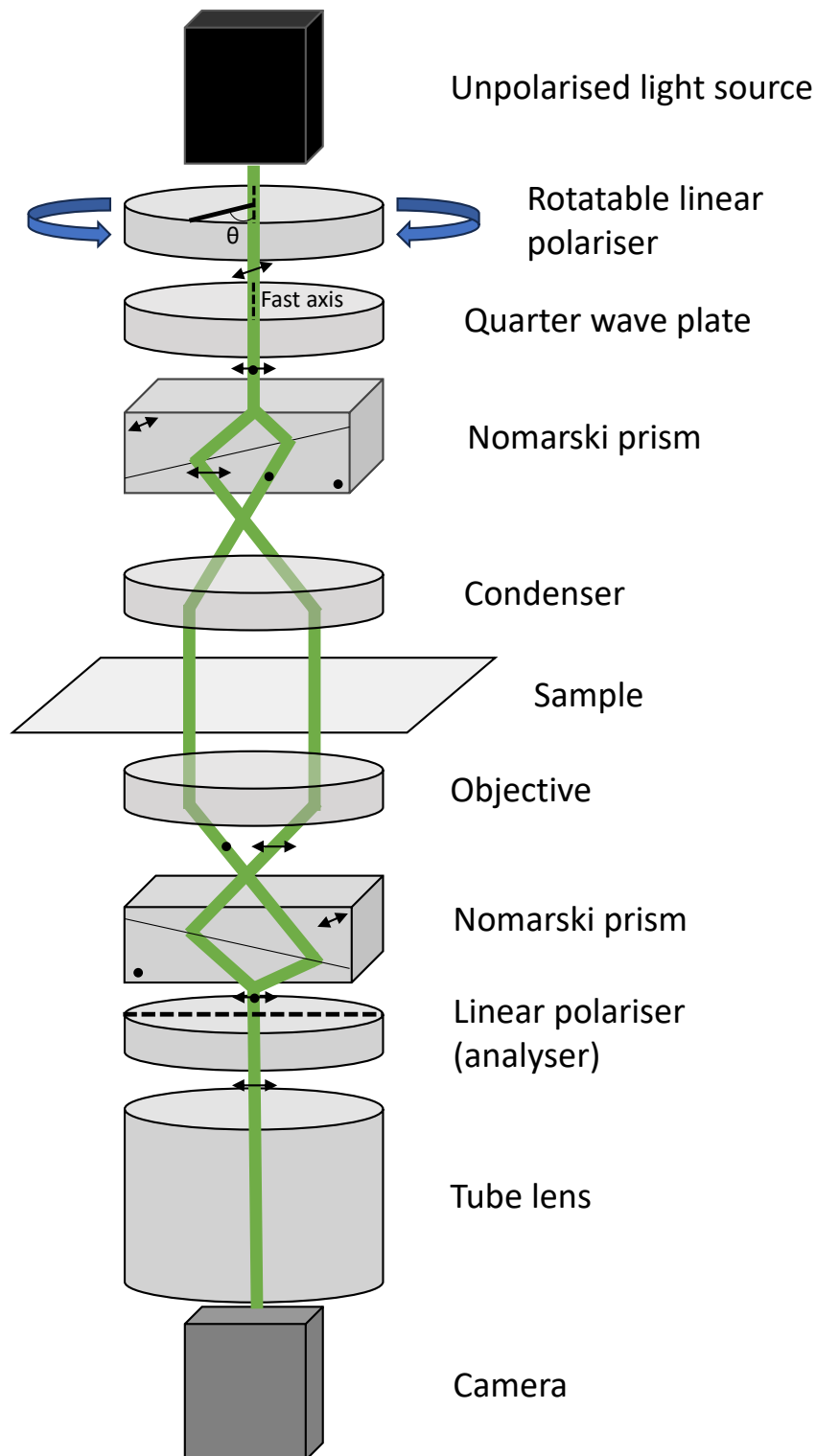
Figure 2.1: Sketch of the principal optical elements of microscope setup used to obtain DIC images of the polystyrene beads and nanodiamond samples with the arrows and dots indicating the polarisation state of the light. Here it is shown that the linear polariser in the de Sènarmont compensator can be rotated creating an angle, θ, to the fast axis of the quarter wave plate. The analyser is then shown orthogonal to the fast axis of the wave plate.

arranged such that their optical axes are at an angle causing the incident beam to split into two orthogonally linearly polarised components, separated by a small angle. The beams are then focused onto the sample by the condenser, where the directional split times the condenser focal length creates the shear distance, $\vec{s}$, which is similar to the diffraction limited lateral resolution. As the beams pass through the sample, they each undergo a phase shift, ϕ, proportional to the optical thickness of the part of the sample they pass through. The phase difference, $\delta(\vec{r})$, of the beams at a position, $\vec{r}$, is therefore given by

$$\delta(\vec{r}) = \phi\left(\vec{r} + \frac{\vec{s}}{2}\right) - \phi\left(\vec{r} - \frac{\vec{s}}{2}\right). \tag{2.2}$$

Once through the sample, the beams pass through the objective and are recombined in a second Nomarski prism. A Nomarski prism is a type of Wollaston prism, however, in this type of prism the beams immediately diverge due to the different directions of the group velocity of the beams. Once at the crystal boundary, the beams are refracted towards each other such that they converge at an interference plane. The second polariser, known as an analyser, which is aligned orthogonally to the fast axis of the quarter wave plate allows the orthogonally polarised beams to interfere. Any phase difference of the beams after passing through the sample results in a change of polarisation state of the beams causing variations in the intensity after the polariser dependent on gradients of optical thicknesses across the sample. Finally the transmitted beam is imaged by a tube lens onto the camera and the image intensity, I_{DIC}, at each point of the sample is then given by

$$I_{\text{DIC}}(\vec{r}, \theta) = \frac{I_{\text{ex}}}{2}(1 - [\cos(2\theta - \delta(\vec{r}))]). \tag{2.3}$$

The angle θ used controls the image contrast. If the angle is set to be too large for a sample with a small phase shift, the image contrast will be too low, equally if the angle is set too low for larger phase shifts then the image contrast could be too high as can be predicted from Equation 2.3. For quantitative analysis, and to remove spatial inhomogeneities, the dependence on the term I_{ex} is eliminated as follows. Images, $I_{\pm}(\phi)$, are obtained at positive and negative angles, $+\psi$ and $-\psi$, and the contrast, $I_c(\vec{r})$, is calculated as

$$I_c(\vec{r}) = \frac{I_{+\psi}(\vec{r}) - I_{-\psi}(\vec{r})}{I_{+\psi}(\vec{r}) + I_{-\psi}(\vec{r})}. \tag{2.4}$$

This can be rewritten as

$$I_c(\vec{r}) = \frac{\sin(2\theta)\sin(\delta)}{\cos(2\theta)\cos(\delta) - 1}. \tag{2.5}$$

The phase difference, $\delta(r)$, can be obtained by rearranging Equation 2.5 to give

$$\sin(\delta) = I_c \frac{\cos(2\theta)\sqrt{1 - I_c^2} - 1}{\sin(2\theta)} \frac{1}{1 + I_c^2 \cot^2(2\theta)}. \tag{2.6}$$

A Wiener filtering process is then used, where the image is integrated in the Fourier domain with the phase difference of the image being described as a convolution, denoted by star, between the phase profile, $\phi(\vec{r})$, with two Dirac delta functions separated by the shear vector, $\vec{s}$. The initial equation for the phase difference described above is given by

$$\delta = \left[\delta\left(\vec{r} + \frac{\vec{s}}{2}\right) - \delta\left(\vec{r} - \frac{\vec{s}}{2}\right)\right] * \phi(\vec{r}), \tag{2.7}$$

for which the Fourier transform of this equation is

$$\mathcal{F}(\delta) = \int_{-\infty}^{\infty} \left[\delta \left(\vec{r} + \frac{\vec{s}}{2} \right) - \delta \left(\vec{r} - \frac{\vec{s}}{2} \right) \right] e^{-2\pi i \vec{r} \vec{\nu}} d\vec{r} \cdot \mathcal{F}(\phi). \tag{2.8}$$

Given then that the Fourier transform (denoted by $\mathcal{F}$) of a Dirac delta function is $\mathcal{F}(\delta(x+a)) = e^{2\pi i \nu_x a}$, where $\vec{\nu}$ is the spatial frequency, equation 2.8 can be rewritten as

$$\mathcal{F}(\delta) = [e^{i\pi \vec{\nu} \vec{s}} - e^{-i\pi \vec{\nu} \vec{s}}] \mathcal{F}(\phi). \tag{2.9}$$

By substituting in the wave vector, $\vec{k}$, for $\vec{\nu}$ ($\vec{\nu} = \frac{\vec{k}}{2\pi}$) the DIC tranform of the sample phase map in the Fourier domain can be expressed as

$$\mathcal{F}(\delta) = \xi \mathcal{F}(\phi) \tag{2.10}$$

where $\xi = 2i \sin \left(\frac{\vec{s} \cdot \vec{k}}{2} \right)$. There are however, issues that can arise when $\mathcal{F}(\delta)$ is divided by ξ when trying to calculate the phase, ϕ, for a given point. At regions where $\vec{s} \cdot \vec{k}$ are equal to an integer multiple of π, a division by zero results. Further, this method does not take into account any limitations of the camera being used, in which a noise component is always present which is amplified when $|\xi| << 0$. Wiener deconvolution can be used to deal with these issues.

In Wiener deconvolution, an estimated signal to noise ratio of the data when deconvolved, κ, is used to limit the enhancement of noise in the image. The Wiener filter is given by

$$W = \frac{1}{\xi + (\kappa \xi^*)^{-1}}, \tag{2.11}$$

and hence Equation 2.10 is changed to

$$W\mathcal{F}(\delta) = \mathcal{F}(\phi) \tag{2.12}$$

from which the phase can be recovered by applying an inverse Fourier transformation to both sides of Equation 2.12. When using this method, it is important to carry out a systematic investigation into the best value for κ to be used. This is due in part to the final signal to noise ratio in the deconvolved image not being known at this point, but also because of the stripes arising at large values of κ. The shape and intensity of these artefacts are determined by the value of κ used, with higher values typically elongating the stripes (scaling as $\sqrt{\kappa}$). Examples of the effect of increasing κ can be seen in Figures 3.1 to 3.3.

Once the phase image has been obtained using this method, the integrated phase area was found for each particle in the image using an in house written ImageJ script, as described in Payne, et al. [128]. The integrated phase area of each particle in the phase images could then be calculated using

$$A_\phi^m = \int_0^{r_{\mathrm{i}}} \phi(\vec{r}) \, 2\pi r \, dr, \tag{2.13}$$

where r_i is the radius of the region around the particle used for the integration. This was carried out in the analysis software as a sum of all the pixel values within the r_i region around each particle. The local background around each particle is found by using the same integration from r_{i} to $2r_{\mathrm{i}}$. By substituting in the equation for optical phase,

$$\phi(\vec{r}) = \frac{2\pi \, (n_p - n_m) t(\vec{r})}{\lambda_{ex}}, \tag{2.14}$$

wherein n_p is the refractive index of the particles, n_m is the refractive index of the surrounding medium, and t is the thickness, the volume can be found by rearranging the resulting equation

$$A_\phi^m = \frac{2\pi(n_p - n_m)V}{\lambda_{ex}}. \tag{2.15}$$

For a spherical particle its radius can then be expressed as $R = \sqrt[3]{\frac{3V}{4\pi}}$.

2.3   Extinction Microscopy

2.3.1   Setup

Extinction measurements of the graphene sample was carried out using the same microscope and illumination as in Section 2.2.1. A green bandpass filter (Thorlabs FBH-550-40) and neutral colour balance filter (Nikon NCB) were used to obtain illumination with a peak wavelength of 550 nm and FWHM of 40 nm. Home built azimuthal and radial polarisation filters were used to achieve negligible or strong axial polarisation at the sample to confirm the presence of graphene flakes. These were made using 3D printed disks with 6 segments each, into which aluminium wire-grid foil (MLP-WG, MeCan, USA) was mounted. This polarising film was oriented such that the polarisation direction was along the centre of each segment for the radial polariser, and across the centre for the azimuthal polariser as can be seen in Figure 2.2. Unpolarised measurements were also obtained to find the size of the graphene flakes. Light was focussed onto the sample using the oil condenser, and the 1.45 NA objective was used and a 1x tube lens in conjunction with a water cooled scientific-CMOS camera (PCO Edge 5.5, with 30,000 electrons full well capacity, 1.69 electron read noise, [and at minimum gain used throughout] 0.54 electrons per count and 98 counts offset, 16 bit dynamic range) to image the transmitted light. For the measurements obtained using the radial polariser, a home-made dark-field illumination ring blocking the 0-1 NA range was used, replacing the PH1 module of the oil immersion condenser. This setup can be seen in Figure 2.3.

Radial Polariser   Azimuthal Polariser
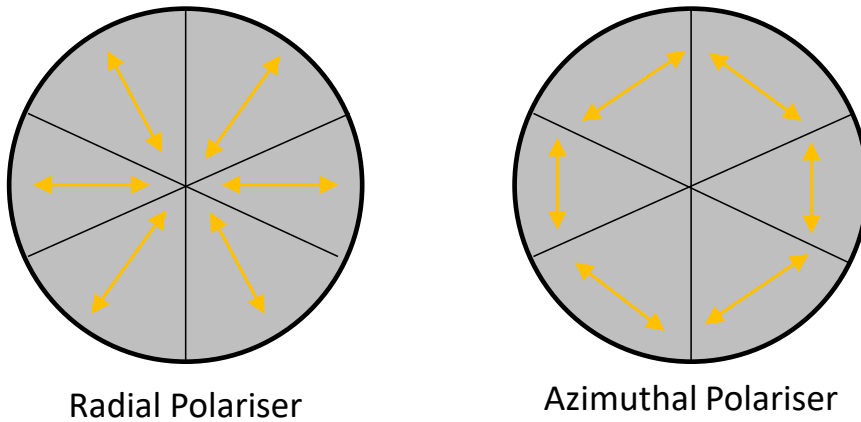
Figure 2.2: Diagrams showing the home built, six segmented, radial (left) and azimuthal (right) polarisers, with their respective polarisation directions given by yellow arrows.
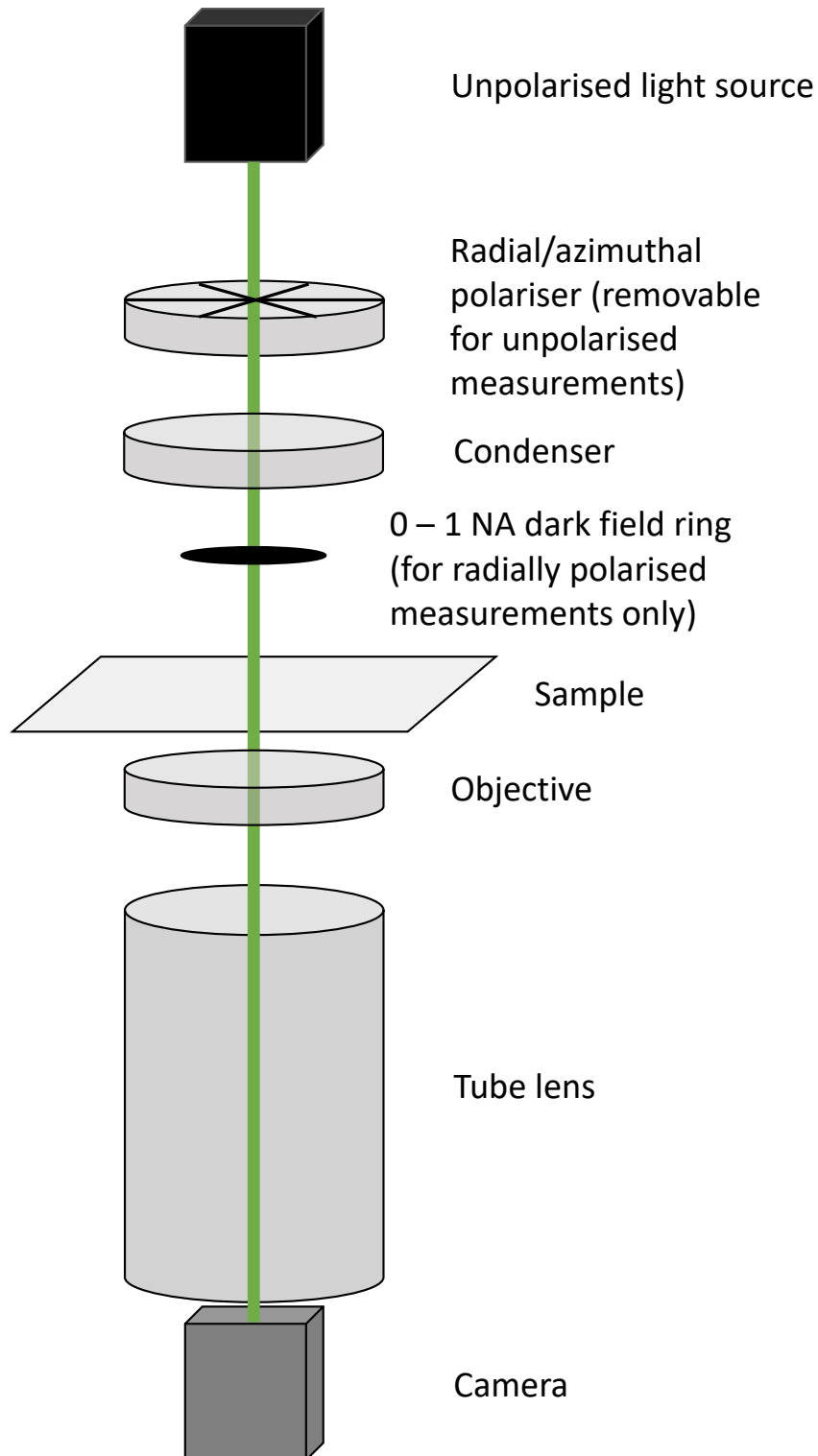
Figure 2.3: Diagram showing the key components used for the extinction measurements described here. The radial and azimuthal polarisers could be inserted and removed between measurements, or removed entirely for unpolarised measurements, while the dark field ring after the condenser was used only for the radially polarised measurements.

2.3.2 Extinction Image Development

The procedure for extinction microscopy followed was the same as that described in [128] and [129]. A series of images were obtained, with the sample being shifted back and forth by $1.4\,\mu$m in the x direction to provide an average over $N_a = 12800$ frames per stack of images. Given an excitation wavelength, λ, of 550 nm, along with a pixel pitch, d_{px}, of 6500 nm, a magnification, M, of 100, and the camera full well capacity, N_{fw}, of 30000 electrons, the shot noise, σ_{n}, for these measurements was calculated to be around $3\,\mathrm{nm}^2$ using [128]

$$\sigma_{\mathrm{n}} = \frac{3\lambda d_{\mathrm{px}}}{2M\mathrm{NA}}\sqrt{\frac{\pi}{N_a N_{\mathrm{fw}}}}. \tag{2.16}$$

An image subtraction method was then applied such that the intensities of the images from the initial, I_0, and shifted, I_s, positions could be used to find the relative extinction contrast image, Δ, of the particles

$$\Delta = \frac{(I_s - I_0)}{I_s}. \tag{2.17}$$

Once this relative extinction image was found, the extinction cross section of the particles could be found in the same way as the integrated phase area was calculated for the qDIC measurements. Integration at a radius around the particle, r_i, such that this radius encompassed the second airy ring (this was chosen as the majority of the signal is encompassed by this area) given by $r_i = \frac{3\lambda}{2\mathrm{NA}}$, allowed for the extinction cross section to be calculated using

$$2\sigma_{ext} = \int_{A_i} \Delta_0 dA + \int_{A_i} \Delta_s dA. \tag{2.18}$$

2.4 Photothermal Microscopy

2.4.1 Setup

In order to obtain photothermal measurements of the nanodiamond and graphene samples a stimulated Raman setup was used. The laser source consisted of a Ti:Sa (MaiTai HP, Spectra Physics) pulsed laser with a centre wavelength of 820 nm, optical pulses of 150 fs, and 80 MHz repetition rate pumping an optical parametric oscillator (Inspire OPO, Radiantis), from which the idler was used as a Stokes beam, as well as providing the pump for SRL. The Stokes beam was then passed through a glass block before a travelling wave acousto-optic modulator (IntraAction ATM-781A2) was used, with the +1 diffracted order selected, to modulate the beam amplitude at 2.5 MHz while also shifting its frequency by 78 MHz. The pump beam was sent down a separate beam path from the OPO, with a PI linear delay stage allowing a delay to be set between the Stokes and pump beams in the photothermal microscopy experiment, the beams did not overlap in time and therefore no stimulated Raman effect could be seen, meaning any signal was due to the photothermal modulation of the pump beam. Once through the delay line, the pump beam was then recombined with the Stokes beam path using a dichroic mirror, DBS1, (MellesGriotLWP-45-RP808-TP1064-PW-1025-C) which transmitted wavelengths above 950 nm while reflecting those between 780 and 870 nm. Once recombined, the pump and Stokes beams were passed through a second glass block,
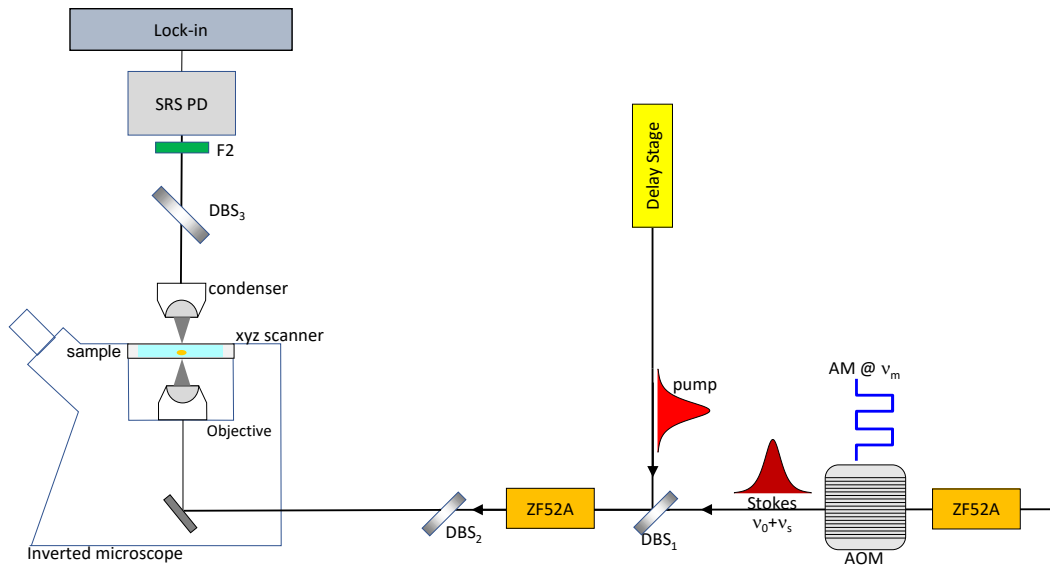
Figure 2.4: Diagram showing the beam-paths and microscope setup used to obtain the photothermal measurements. The Stokes beam is shown passing through the acousto-optic modulator (AOM) providing the frequency shift ν_s from its initial frequency ν_0. A dichroic beam splitter (DBS) can then be seen which recombines the pump and Stokes beams prior to passing through the glass block (ZF52A), and through the microscope optics to the detector. Figure provided by Prof. Borri and Prof. Langbein.

providing control of the linear chirp and spectral focusing of the beams as discussed in [170], before passing through the microscope optics to the sample.

For all measurements a 1.45 NA, 100x oil immersion objective (Nikon CFI Plan Apochromat lambda, MRD01905) was used, with the sample mounted on an inverted Nikon Ti-U microscope stand. The beam was scanned by x-y galvo mirrors relayed into the objective back focal plane. An oil immersion condenser with adjustable NA, and maximum 1.34 NA, was used to collect the photothermal signal. The pump beam is then separated from the Stokes beam using a shortpass filter, F2, (Semrock FF01-945/SP) allowing the modulation of the pump beam to be detected with an SRS photodiode (Hamamatsu S6976), which has an 86% quantum efficiency at 820 nm, and a home built 2.5 MHz resonant circuit (with a DC impedence of 3.6 Ω). Detected modulation of the pump beam was analysed using a dual phase lock-in amplifier (Zurich Instruments HF2LI). This setup can be seen in Figure 2.4.

2.4.2 Photothermal Modulation

Using the setup as described above, the Stokes beam was set to have a wavelength of 1080 nm with the glass blocks adjusted to provide a pulse duration of 1.12 ps and a spectral resolution of $34\,\mathrm{cm^{-1}}$, while the pump beam had a wavelength of 820 nm. This allows a reference SRS signal for the silicone oil mounting medium to be found at $2904\,\mathrm{cm^{-1}}$, the spectrum for which can be seen in Figure 2.5, away from the first order diamond and graphite SRS signals at $1332\,\mathrm{cm^{-1}}$ and $1575\,\mathrm{cm^{-1}}$, respectively. This was also away from the second order graphite Raman peaks at $2700\,\mathrm{cm^{-1}}$ and $3250\,\mathrm{cm^{-1}}$. Once the peak SRS signal was found, the phase of the lock-in could be set such that the signal phase relative to the electronic reference was

zero (i.e. in phase). The delay line could then be set to allow the Stokes beam to arrive at the sample first, followed by the pump beam at a prescribed time later (in this case 2.69 ps) such that a photothermal signal could be obtained while avoiding any Raman signal from either the Raman vibrations of diamond or graphite. This photothermal signal occurred due to absorption of the Stokes beam by sp2 bonds in the samples, which in turn caused heating of the oil surrounding each particle hence changing the refractive index of said oil. The change in refractive index subsequently modulated the pump beam profile (photothermal lensing) causing a pump loss (due to the clipping of the mode in the collection geometry) which could be measured by the SRS photodiode. For each measurement, the in-phase and in-quadrature components of the signal were acquired and here called real, $\Re$, and imaginary, $\Im$, parts from which the photothermal signal amplitude, S_{LI}, measured by the lock-in could be found using the equation

$$S_{LI} = \sqrt{\Re^2 + \Im^2}, \tag{2.19}$$

while the phase of the photothermal signal, ϕ, can be calculated by

$$S_{LI} = |S_{LI}|\exp(i\phi). \tag{2.20}$$

To obtain the real and imaginary signals from a measured image, a mask was applied to the background using imageJ as can be seen in Figure 2.6, and the sum of all pixels making up an individual particle was obtained using the Raw Integrated Density function. By then applying the known pixel area, A_{px}, the integrated amplitude of the particle could be calculated using

$$A_{LI} = A_{px}S_{LI}. \tag{2.21}$$

Also acquired was the DC signal, S_{DC}, which could be used to calculate the relative modulation of the pump beam. By also taking into account the point spread function (PSF), the peak relative modulation, M_{rel}, for each particle could then be obtained using

$$M_{rel} = \frac{3.6 \times 10^{-4} A_{LI}}{A_{PSF}S_{DC}}, \tag{2.22}$$

where 3.6×10^{-4} was the relative impedance between S_{DC} ($3.6\,\Omega$) and A_{LI} ($10\,\mathrm{k\Omega}$), and the average PSF area being $A_{PSF} = (0.26\,\mu\mathrm{m})^2$ for typical particles. While this was the average A_{PSF}, for individual particles this could vary between $(0.1\,\mu\mathrm{m})^2$ and $(0.5\,\mu\mathrm{m})^2$ depending on their size. Due to the higher impedance of the photodiode, the relative impedance is applied such that the DC signal matches that of the photodiode.

2.4.3   Photothermal Lifetime

To find the photothermal lifetime, which is the time taken for the photothermal lensing to dissipate, it was assumed that the resulting photothermal signal due to instantaneous heating, S(t), has an exponential decay such that the signal is given by

$$S(t) = S_0 \frac{e^{\frac{-t}{\tau}}}{1 - e^{\frac{-T}{\tau}}}, \tag{2.23}$$

over a period $0 \leq t \leq T$ (in this case 400 ns from the 2.5 MHz modulation), where τ is the photothermal lifetime, and S_0 is the instantaneous photothermal signal. From
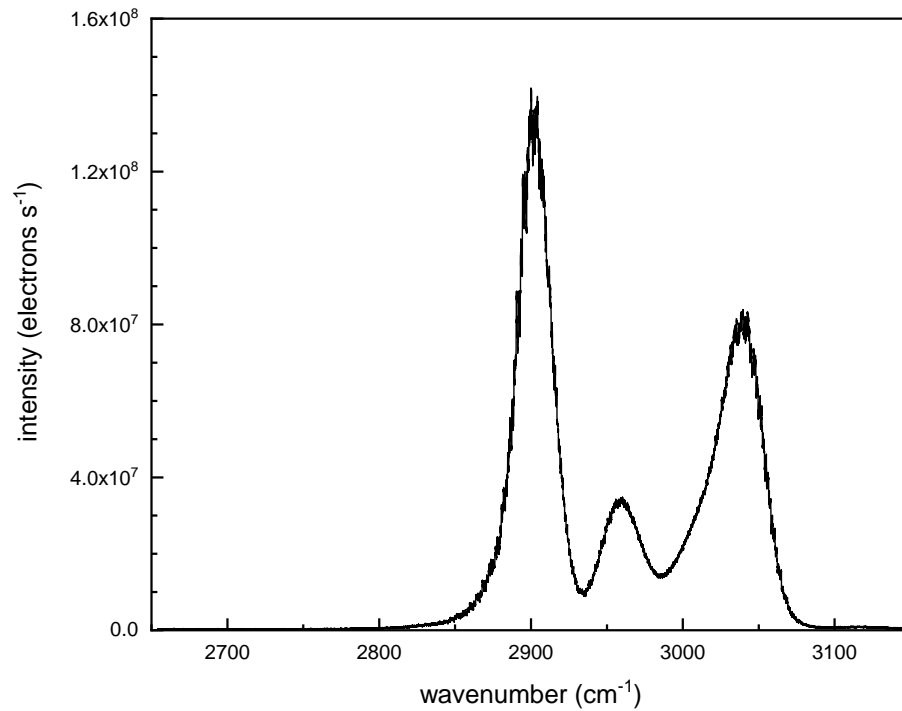
Figure 2.5: Raman resonance peaks for silicone oil between $2650\,\mathrm{cm}^{-1}$ and $3150\,\mathrm{cm}^{-1}$.
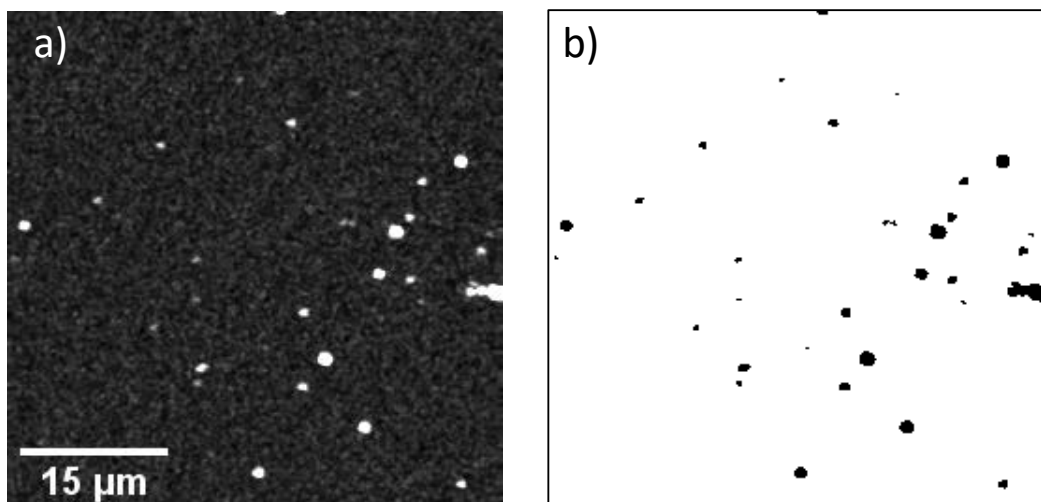
Figure 2.6: Photothermal image of the untreated 250 nm ND sample (a, gray scale from $m = 0$ V [black] to $M = 0.3$ mV [white]) and an image of the same region with a threshold applied and displayed using a binary (black/white) colour map for analysis (b).

this the complex lock-in signal amplitude measured at the fundamental frequency, S_{LI}, could be described as as

$$S_{LI} = \frac{\sqrt{2}}{T} \int_0^T S(t)e^{-2\pi i\tau/T}d\tau. \tag{2.24}$$

By integrating this equation and introducing the value $\alpha = \frac{T}{\tau}$, the equation

$$S_{LI} = S_0 \frac{e^{-\alpha} - 1}{(-2\pi i\alpha)(1 - e^{-\alpha})} \tag{2.25}$$

could be obtained, which can be simplified to $S_{LI} = \frac{S_0}{\alpha + 2\pi i}$, allowing the instantaneous photothermal signal to be found using

$$S_0 = \frac{S_{LI}}{\alpha - 2\pi i}. \tag{2.26}$$

Finally, the following equation can be rewritten to find the photothermal lifetime

$$\frac{\alpha}{2\pi} = \frac{\Re(\frac{1}{S_{LI}})}{\Im(\frac{1}{S_{LI}})}, \tag{2.27}$$

first by substituting in $\alpha = \frac{T}{\tau}$ which gives

$$\tau = \frac{T}{2\pi} \frac{\Im(\frac{1}{S_{LI}})}{\Re(\frac{1}{S_{LI}})}, \tag{2.28}$$

and then by using the identity $\frac{\Im(\frac{1}{S_{LI}})}{\Re(\frac{1}{S_{LI}})} = \frac{-\Im(S_{LI})}{\Re(S_{LI})}$, Equation 2.27 can be written as

$$\tau = \frac{T}{2\pi} \frac{-\Im(S_{LI})}{\Re(S_{LI})}, \tag{2.29}$$

from which the photothermal lifetime can be calculated.

Chapter 3

Sizing individual dielectric nanoparticles using qDIC microscopy

3.1 Introduction

With growing uses of dielectric nanoparticles (NPs) such as nanodiamond in a wide variety of applications, ranging from biomarkers and drug delivery in medicine to quantum and industrial applications, accurate sizing of these particles has become ever more important [52]. Particularly in the case of biomarkers and drug delivery in medicine, the size of a NP is especially important as the uptake into cells is highly dependant upon it [61]. Currently the industry standard when it comes to sizing NPs is electron microscopy, however, this comes with drawbacks [101, 102]. In general, electron microscopy is a low throughput technique capable of imaging only a limited number of particles at a time and must be carried out in a vacuum. More specifically, when sizing organic dielectric materials, electron microscopy is limited due to a lower electron density when compared with metallic materials [103]. Another common technique for sizing NPs is DLS as has been discussed in (Section 1.3.2). Limitations of DLS can be seen if large particles are present mixed in with the analyte, which can significantly skew the results due to them dominating the scattering response. As a result of this, and given the measurements are for particle ensembles, the technique is low resolution thus requiring separation of polydispersed samples prior to measurement [105]. Further, the technique does not measure the geometric size of the sample, but rather the hydrodynamic size which can cause an overestimation of the particle sizes.

Using wide-field optical microscopy to measure the sizes of NPs requires knowledge of the optical properties of the materials being measured to link the strength of the optical signals to NP sizes. This is due to the diffraction limit of optical microscopy, meaning a spatial resolution of around 200 nm, which is larger than most NPs being measured, in other words the size of a NP cannot be directly resolved under a light microscope. However, the benefits of using wide-field optical setup include a high throughout, simplicity, and low cost. Due to this, there are several techniques which now make use of the benefits listed for NP sizing. As discussed previously in Section 1.3, extinction microscopy, iSCAT, COBRI, and a number of DIC techniques have been developed to measure quantitative properties (including sizes) of dielectric NPs. Extinction microscopy for instance, has been shown to be

effective at measuring GNPs down to 2 nm, however, for dielectric NPs the sensitivity of this technique is limited to much larger particles such as PS beads on the order of 100 nm [128]. This is because, in the small size limit, the optical extinction technique is more sensitive to particles that strongly absorb light such that the extinction cross section is roughly equal to the absorption cross section. Given then their negligible absorption of visible light, extinction microscopy is not well suited for measurements of small dielectric NPs. Alternatively, phase contrast techniques such as iSCAT and COBRI have been used to measure single dielectric NPs, with the former being used to observe biological macromolecules, and the latter being used to track silica NPs down to 50 nm size with a sensitivity limit down to 30 nm [115].

A number of methods to recover DIC images have been developed, as discussed in Section 1.3.5. While DIC still has all the benefits of wide field microscopy, it is also a simple and widespread interferometric technique with few specific components being required that are not commercially available. Previously, the qDIC analysis technique (see Section 2.2.2) has been used to measure quantitative properties of biological samples, such as the lamellarity of giant lipid vesicles and the thickness of lipid bilayers [142, 143, 144]. This chapter shows the optimisation and calibration of this technique for measuring 100 nm and 15 nm radius PS beads. Parts of this chapters content is published in [173].

3.2 κ and r_i Optimisation

$\delta(\vec{r})$ phase images of the 100 nm radius PS beads mounted in silicone oil (SO), using 1.45 NA, 1.27 NA, and 0.75 NA objectives at a phase offset of $\psi = 30°$, are shown in Figures 3.1a, 3.2a, and 3.3a, respectively. A shadow-cast pattern, typical of DIC images, can be seen with no blemishes or vignetting showing the capability of removing the I_{ex} dependence in the image contrast. The peak and dips present in the stripe pattern in the retrieved $\phi(\vec{r})$ (see Equation 2.12) images (Figure 3.1b, c, and d) are due to the elongation of the PSF, with the two beams used being elongated orthogonal to each other along and across the shear. This effect is less pronounced when the 0.75 NA objective was used, as can be seen in Figure 3.3. If further quarter waveplates were to be added after the first prism and before the second prism, the light would be circularly polarised causing a circular PSF to be seen and hence eliminate the effect.

In order to calibrate the qDIC analysis, the values used for κ and r_i from Equation 2.11 and Equation 2.13 were varied to determine their effect on the obtained value for the measured integrated phase area (A_ϕ^m) of the beads. To achieve this, analysis was carried out varying κ from 0.5 to 10^5 and r_i from 1 to 9 pixels for the 0.75, 1.27, and 1.45 NA objectives using a phase angle of $\psi = 30°$ and the PS bead sample mounted in either silicone or water oil. As can be seen in Figure 3.4, the value obtained for A_ϕ^m for the sample measured with the 1.45 NA objective increases as κ increases up to $r_\mathrm{i} = 4$ before starting to level off at values of $\kappa > 50$. A similar pattern was observed for each objective. The values (κ, r_i) found for the point at which saturation occurred were found to be $(10^5, 4)$, $(1000, 8)$, and $(1000, 8)$ for the 0.75 NA, 1.27 NA, and 1.45 NA objectives, respectively. The dependence of κ and r_i on A_ϕ^m for the 1.45 NA objective can be seen in Figure 3.4a. However, it is clear from Figure 3.4b that the signal to noise ratio (SNR), calculated using $\mathrm{SNR} = A_\phi^m/\sigma$, obtained at these values is very small. Due to this, the (κ, r_i) values

Figure 3.1: DIC images of the PS bead sample mounted with silicon oil imaged with 1.45 NA and a phase offset of $\psi = 30°$. (a) $\delta(\vec{r})$ on a grey scale as shown, from $m = -0.05$ to $M = 0.05$. The shadow cast impression of DIC is evident, with the shear $s = 0.23(1,1)/\sqrt{2}\,\mu$m in the (x,y) coordinates with x horizontal and y vertical. $\phi(\vec{r})$ images showing a region of $(2.71 \times 2.07)\,\mu$m^2 around a selected bead indicated by the dashed circle in (a) are shown for $\kappa = 1$ (b, $m = -0.015$ to $M = 0.03$), $\kappa = 200$ (c, $m = -0.02$ to $M = 0.04$), and $\kappa = 1000$ (d, $m = -0.03$ to $M = 0.03$), with the red and blue circles having the radii r_i and $2r_i$, respectively. $r_i = 2.5$, 4, and 8 pixels in b, c, and d, respectively. Adapted from [173].
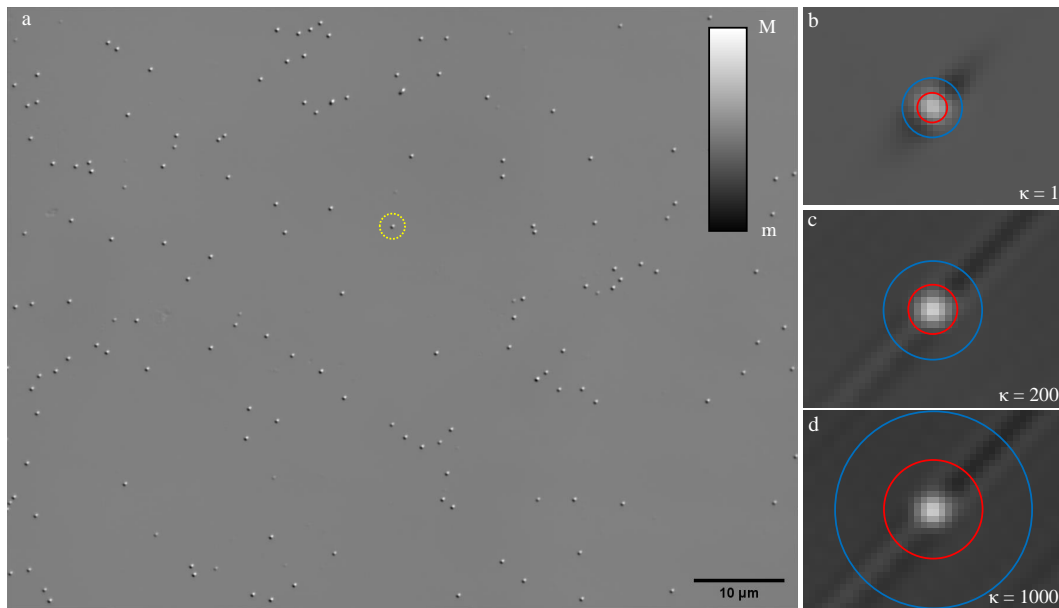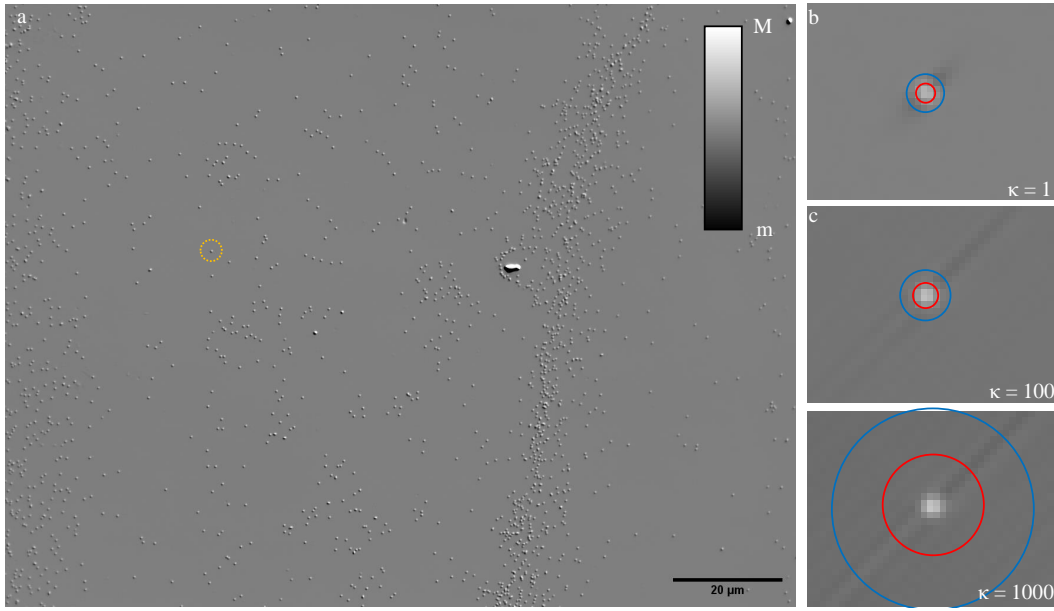
Figure 3.2: DIC images of the PS bead sample mounted with silicon oil imaged with 1.27 NA and a phase offset of $\psi = 30°$. (a) $\delta(\vec{r})$ on a grey scale as shown, from $m = $ -0.050 to $M = 0.050$ (black scale bar $= 30\,\mu$m). $\phi(\vec{r})$ images showing a region of $(4.30 \times 3.33)\,\mu$m^2 around a selected bead indicated by the dashed circle in (a) are shown for $\kappa = 1$ (b, $m = $ -0.041 to $M = 0.041$), $\kappa = 100$ (c, $m = $ -0.050 to $M = 0.060$), and $\kappa = 10000$ (d, $m = $ -0.039 to $M = 0.059$), with the red and blue circles having the radii r_i and $2r_i$, respectively. $r_i = 1.5$, 2, and 8 pixels in b, c, and d, respectively.

for which the best SNR using each objective were found (SN). To do this, 1000 background points (points where no particle was visible) were analysed using the same procedure for the same κ and r_i range, and the integrated phase area for each point was calculated. The resulting distributions were then fitted with a Gaussian to find the standard deviation of the background (σ). The SNR for each κ and r_i pair was then calculated. Figure 3.4b shows that, for the 1.45 NA objective, the SNR increases with r_i from zero due to the increasing A. However, after a certain r_i value, in the case of the 1.45 NA objective $r_i > 2.5$, the SNR decreases again due to the increasing σ of the background. At $\kappa > 1$ for all objectives, the SNR again decreases as the σ obtained for the background continues increasing while A_ϕ^m starts to saturate as κ increases. The values found as the SN pairs were (1, 1), (1, 1.5), and (1, 2.5) for the 0.75 NA, 1.27 NA, and 1.45 NA objectives, respectively. The highest SNR decreases with the NA, with the values of 550, 400, and 130 for the 1.45 NA, 1.27 NA, and 0.75 NA objectives, respectively.

A third pair of values was subsequently chosen for each objective to obtain a good SNR while minimising systematic errors (SE) due to a minimised sensitivity to the shape of the PSF. The r_i values were chosen for each objective such that it corresponded to the PSF size, as can be seen in Figure 3.4c, with the κ value being chosen to give a good SNR at the selected r_i values. Hence, the pairs chosen for this were (100, 2), (100, 2), and (200, 4) which gave SNR values of 49, 180, and 160 for the 0.75 NA, 1.27 NA, and 1.45 NA objectives, respectively. The respective SNR values for each objective at saturation were found to be 6, 14, and 20. Plots similar to Figure 3.4, showing how A_ϕ^m and SNR vary with r_i, for the 1.27 NA and 0.75 NA
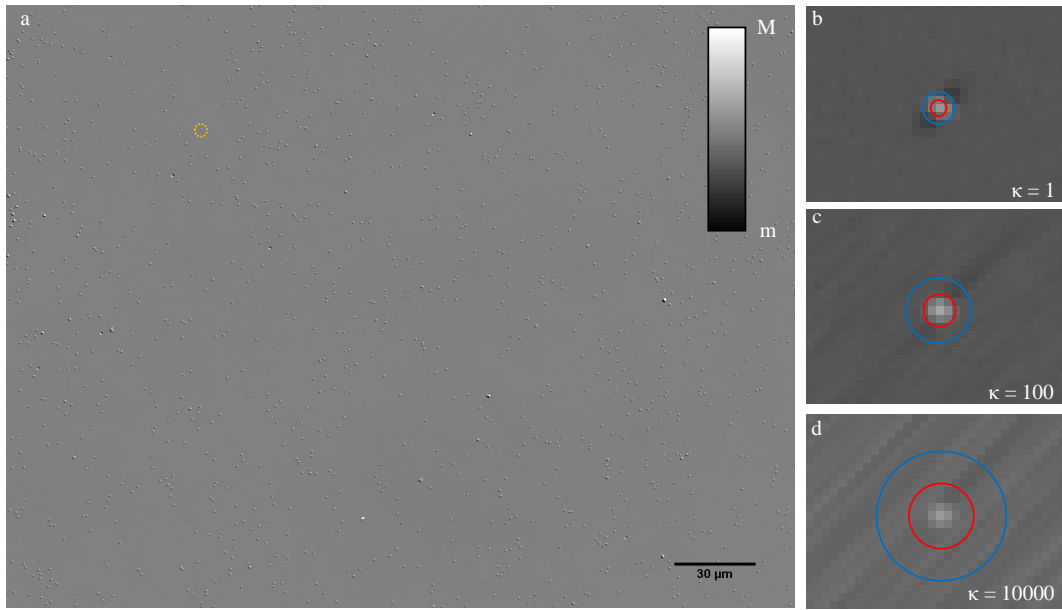
Figure 3.3: DIC images of the PS bead sample mounted with silicon oil imaged with 0.75 NA and a phase offset of $\psi = 30°$. (a) $\delta(\vec{r})$ on a grey scale as shown, from m = -0.015 to M = 0.015 (black scale bar = $30\,\mu$m). $\phi(\vec{r})$ images showing a region of $(6.92 \times 5.19)\,\mu$m^2 around a selected bead indicated by the dashed circle in (a) are shown for $\kappa = 1$ (b, m = -0.005 to M = 0.010), $\kappa = 100$ (c, m = -0.010 to M = 0.021), and $\kappa = 10000$ (d, m = -0.021 to M = 0.030), with the red and blue circles having the radii r_i and $2r_i$, respectively. $r_i = 1$, 2, and 4 pixels in b, c, and d, respectively.
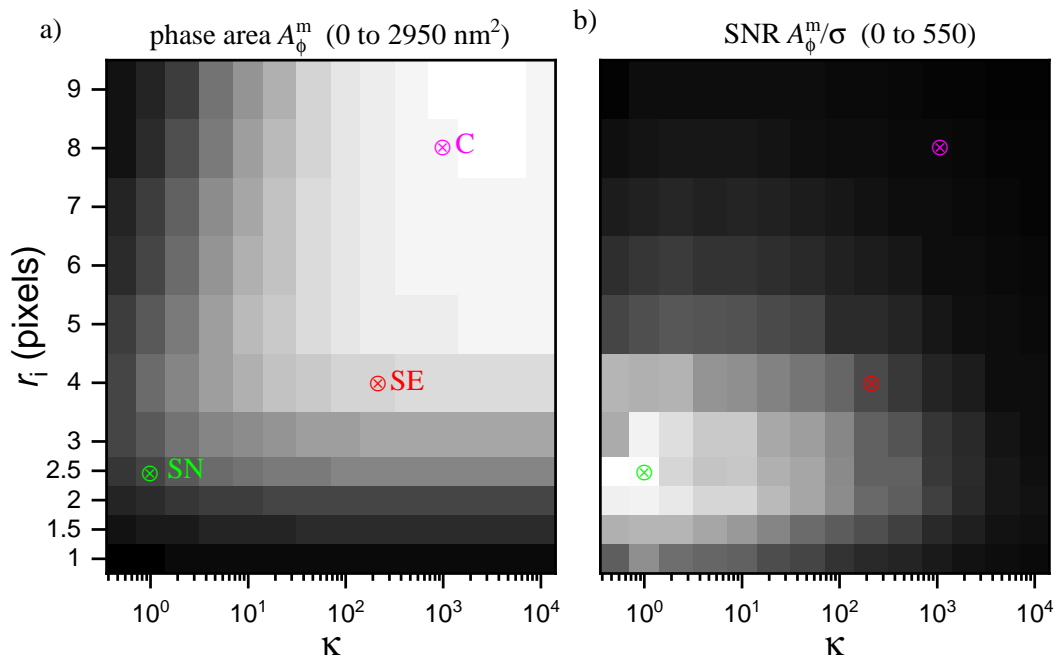
Figure 3.4: Phase area A_ϕ^m (a, m = 0 to M = $2950\,$nm^2) and SNR A_ϕ^m/σ (b, from m = 0 to M = 550) as function κ and r_i for a PS bead mounted in silicone oil and imaged using the 1.45 NA objective. The chosen SN, SE and C pairs are indicated.
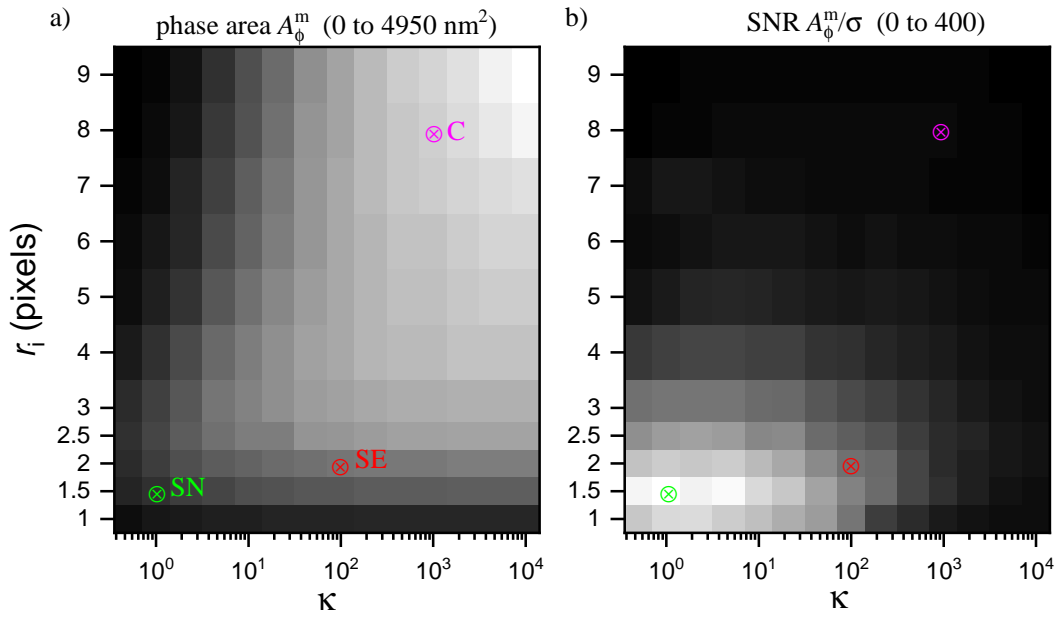
Figure 3.5: Phase area A_ϕ^m (a, m = 0 to M = 4950 nm^2) and SNR A_ϕ^m/σ (b, from m = 0 to M = 400) as function κ and r_i for the 1.27 NA objective.
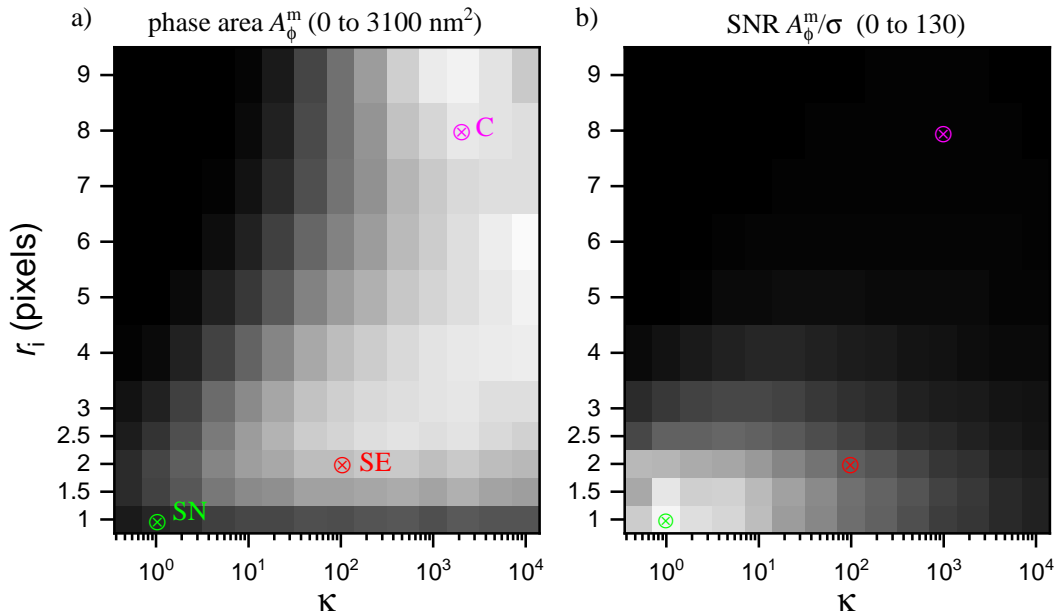
Figure 3.6: Phase area A_ϕ^m (a, m = 0 to M = 3100 nm^2) and SNR A_ϕ^m/σ (b, from m = 0 to M = 130) as function κ and r_i for the 0.75 NA objective.

can be seen in Figures 3.5 and Figure 3.6, respectively, with the relevant the SN, SE, and C pairs marked.

3.3 PS Bead Refractive Index

While the refractive index of polystyrene is known to be about n = 1.59, the exact value depends on the packing density of the polymer. Therefore, measurements of the refractive index of the beads were carried out as follows. The average measured integrated phase areas (A_ϕ^{m}) for both the PS beads mounted in water oil (WO) and silicone oil (SO) were found by fitting a Gaussian distribution to the measured A_ϕ^{m} of the beads imaged using a polariser angle of $\psi = 30°$ and analysed using the C pair for each objective. The C pair was chosen for analysis here as it had the lowest systematic errors of the three possible pairs, also (as is also discussed later in Section 3.4) a correction factor is required when using the SE and SN pairs which had yet to be obtained. The average A_ϕ^{m} in this case was proportional to the difference in refractive index between the particles and mounting medium, $n_p - n_m$, such that

$$A_\phi^{\mathrm{m}} = C(n_p - n_m),\tag{3.1}$$

where n_p and n_m represent the refractive index of the PS beads and medium, respectively, and C was the constant of proportionality. From Equation 2.15 it is expected that the phase area is proportional to the medium refractive index with x intercept (the point at which the obtained integrated phase of the PS beads would be zero) being the refractive index of the PS beads, as at this point the refractive index of the PS beads and its surrounding medium would be the same. From rearranging Equation 3.1, the refractive index of the beads can also be calculated using

$$n_p = n_{wo} \left(\frac{1}{\frac{A_\phi^{so}}{A_\phi^{wo}} - 1} \right) \left(1 - \frac{n_{so}}{n_{wo}} \right),\tag{3.2}$$

where n_{wo} and A_ϕ^{wo} is the refractive index of the water oil and the phase area of the beads mounted in water oil. n_{so} and A_ϕ^{so} are the refractive index of silicone oil and phase area of the beads mounted in silicone oil. The error for the particle refractive index, Δn_p, could be found from the error in phase area for both mounting media, A_ϕ^{wo} for the water oil mounted beads and A_ϕ^{so} for those in silicone oil, such that

$$\Delta n_p = \sqrt{\left(\frac{\partial n_p}{\partial A_\phi^{wo}} \cdot \Delta A_\phi^{wo} \right)^2 + \left(\frac{\partial n_p}{\partial A_\phi^{so}} \cdot \Delta A_\phi^{so} \right)^2}.\tag{3.3}$$

As can be seen in Figure 3.7, the values obtained for the refractive index of the PS beads were $n_p = 1.5884 \pm 0.0005$, $n_p = 1.6007 \pm 0.0016$, and $n_p = 1.5984 \pm 0.0013$ for the 0.75 NA, 1.27 NA, and 1.45 NA objectives, respectively. This is in good agreement with the expected refractive index for polystyrene at the wavelength used for these measurements, as such for all measurements going forward $n_p = 1.59$ was used for the PS beads.

3.4 Correction Factor and Radii

Due to the lower A_ϕ^{m} value obtained at the SE and SN values compared to that of the C pair, a correction factor needed to be found in order to obtain an accurate value
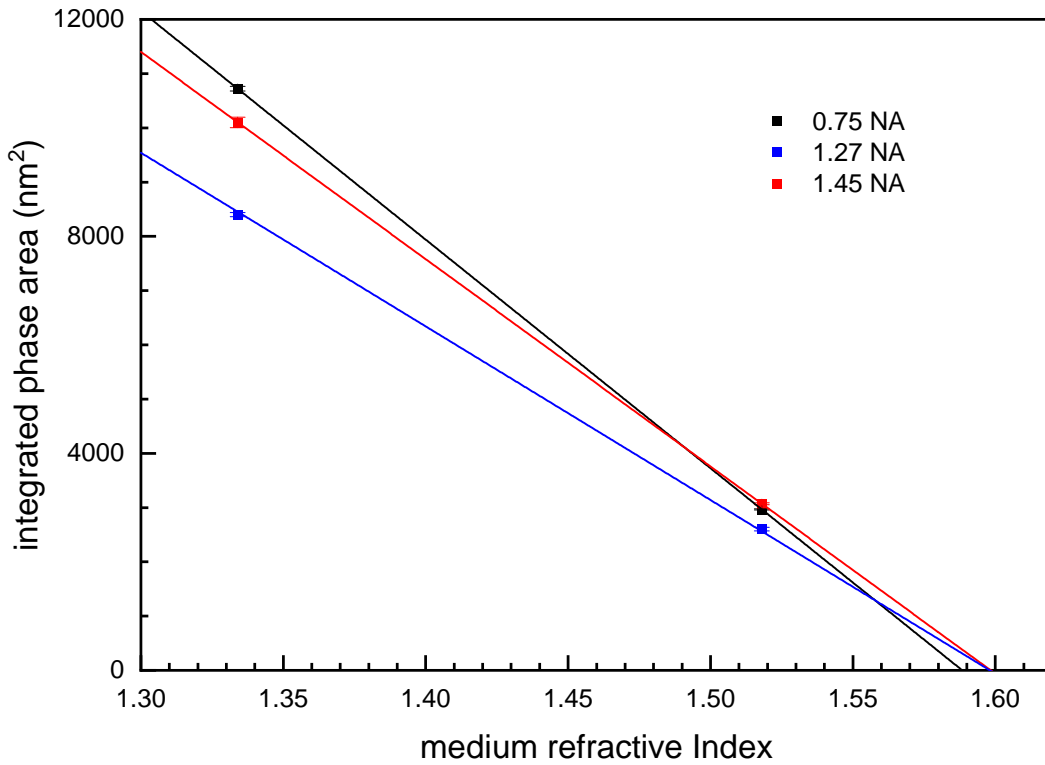
Figure 3.7: Average integrated phase area, A_ϕ^m, of 100 nm radius PS beads in oil and water immersion media for the 0.75 NA (Black), 1.27 NA (Blue), and 1.45 NA (Red) objectives with fits using Equation 3.1.

for the phase area and hence volume, and radius of the beads. This was achieved by calibration, comparing the A_ϕ^m value for the particles in each image at the SE, SN, and C pairs. The value obtained for each particle using the C pair was then divided by those of the SE and SN pairs, resulting in correction factors for each individual particle. These were then plotted as a histogram and a Gaussian fit was applied. The resulting distributions and fit for the silicone oil mounted sample, imaged using the 1.45 NA objective, can be seen in panels a and c of Figure 3.8 for both the SN and SE pairs. The resulting correction factors for this combination were $\rho = 3.48 \pm 0.27$ and $\rho = 1.25 \pm 0.07$ for the SN and SE pairs, respectively. Similar plots for the other objectives and samples can be seen in panels a and c of Figures 3.9 to 3.13, with the resulting correction factors for each plot being found in Table 3.2.

Once the correction factor for each case was found from analysis of all particles in a single field of view for the 0.75 NA objective and 4 fields of view for the 1.27 NA and 1.45 NA objectives, it was applied to the obtained A_ϕ^m for each particle to such that a corrected phase area for each (A_ϕ^c) could be found using $A_\phi^c = \rho A_\phi^m$. From A_ϕ^c the volume and hence radius for each particle was calculated using Equation 2.15 using the refractive index found previously (n = 1.59). The corrected radii were then plotted as histograms to which a fit was applied to obtain the mean size of the individual beads and their standard deviation as can be seen in panels b and d of Figures 3.9 to 3.13, to be compared with the manufacturers specifications. It was expected that the distribution of bead sizes would be Gaussian in nature, with the aggregate size decreasing in a Poissonian manner dependant on the number of beads per aggregate. As such, the fit used comprised a series of eight Gaussians, ensuring

a significant number of aggregate distributions were taken into account, such that

$$p(r) = \sum_{n=1}^{8} \frac{B_n}{\sigma_n \sqrt{2\pi}} \exp\left(-\frac{(R - R_n)}{2\sigma_n^2}\right), \tag{3.4}$$

where R_n was the effective radius of an n-bead aggregate given by $R_n = \sqrt[3]{n}R_1$, σ_n was the n-bead aggregate standard deviation given by $\sigma_n = \sigma_1 n^{-1/6}$, and B_n was applied to give a Poisson distribution of bead aggregates using the equation

$$B_n = B\frac{\lambda^n e^{-\lambda}}{n!}. \tag{3.5}$$

Here, B is a normalisation factor, with λ representing the average number of beads per aggregate. To derive the equation for R_n, the beads are assumed to be spherical such that

$$R_n^3 = n\frac{3V}{4\pi}. \tag{3.6}$$

Given then that $R_1^3 = 3V/4\pi$, this could be rewritten as

$$R_n^3 = nR_1^3. \tag{3.7}$$

So that $R_n = \sqrt[3]{n}R_1$. Similarly, to derive the equation for σ_n, the standard deviation of a single particle volume is defined as

$$\sigma_1^V = \sigma_1 \frac{\partial V}{\partial R}|_{R_1}, \tag{3.8}$$

from which the standard deviation of an n particle aggregate can be written as

$$\sigma_n^V = \sigma_1 \sqrt{n}\frac{\partial V}{\partial R}|_{R_1}. \tag{3.9}$$

The corresponding radius deviations are then given by

$$\sigma_n = \frac{\partial R}{\partial V}|_{R_n} \sqrt{n}\frac{\partial V}{\partial R}|_{R_1}\sigma_1, \tag{3.10}$$

and given that $\partial V/\partial R \propto R^2$ this can be rewritten as

$$\sigma_n = \frac{1}{R_n^2} \sqrt{n}R_1^2\sigma_1. \tag{3.11}$$

Given then the relationship for the number of beads and effective radius this can be simplified to

$$\sigma_n = \frac{\sigma_1}{\sqrt[6]{n}}. \tag{3.12}$$

Figures 3.8c and d show the corrected radii histograms for the sample mounted using silicone oil, imaged using the 1.45 NA objective, and analysed using the SN and SE pairs, respectively. The fits for the plots yielded values of $R_1 = 101.2\,\text{nm}$, $\sigma_1 = 2.2\,\text{nm}$, and $\lambda = 0.01$ for the SN pair, while for the SE pair $R_1 = 100.5\,\text{nm}$, $\sigma_1 = 3.0\,\text{nm}$, and $\lambda = 0.03$. Similar plots for the other mounting medium and objectives can again be seen in Figures 3.9c and d to 3.13c and d. The resulting PS bead radii and standard deviations from all plots can be seen in Table 3.2. For most cases, the standard deviation obtained was higher for the SN pair as compared to

Figure 3.8: Histograms of the correction factors and corrected radii for the 100 nm radius PS beads immersed in silicone oil imaged using the 1.45 NA objective and analysed using the SN (a, b) and SE (c, d) pairs.

Figure 3.9: Histograms of the correction factors and corrected radii for the 100 nm radius PS beads immersed in water oil imaged using the 1.45 NA objective and analysed using the SN (a, b) and SE (c, d) pairs.
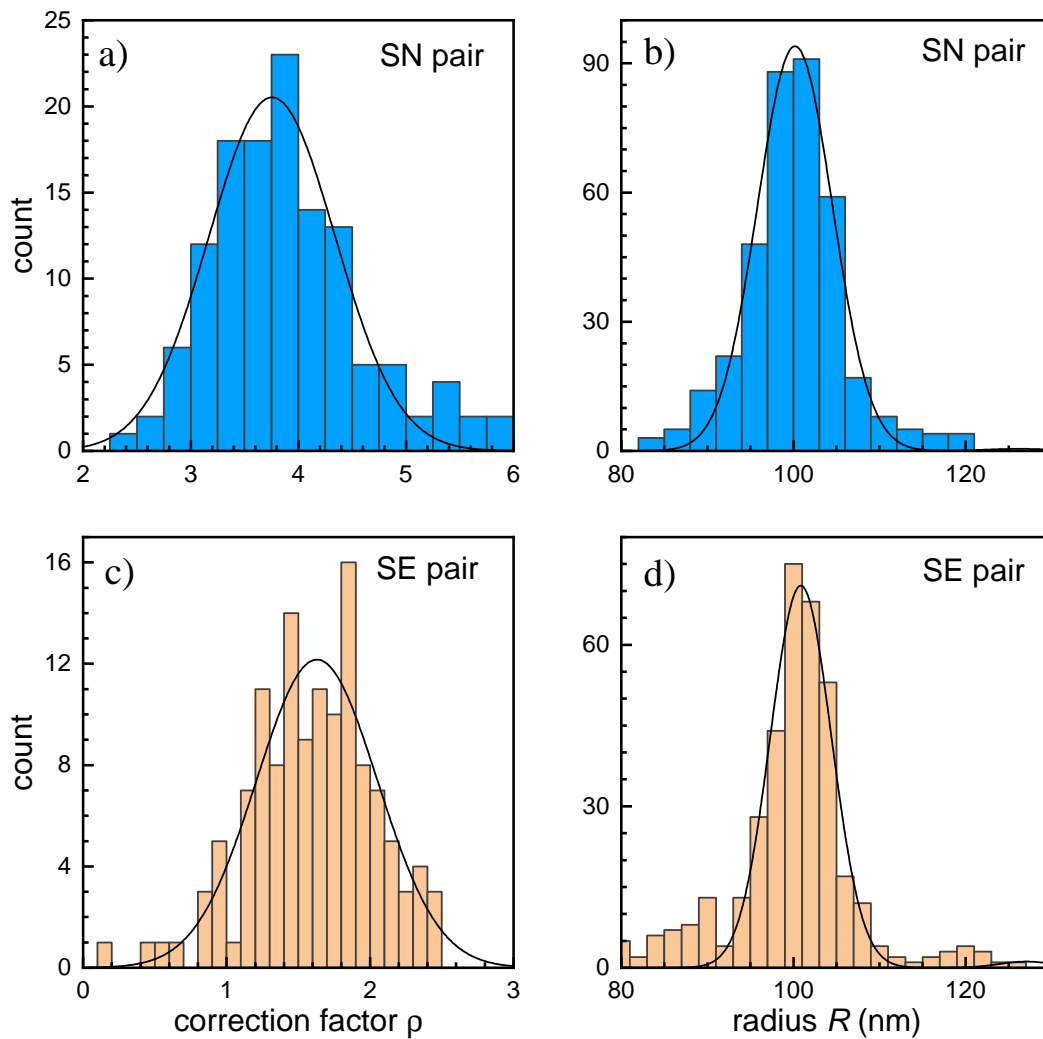
Figure 3.10: Histograms of the correction factors and corrected radii obtained for the 100 nm radius PS beads immersed in silicone oil imaged using the 1.27 NA objective and analysed using the SN (a, b) and SE (c, d) pairs.
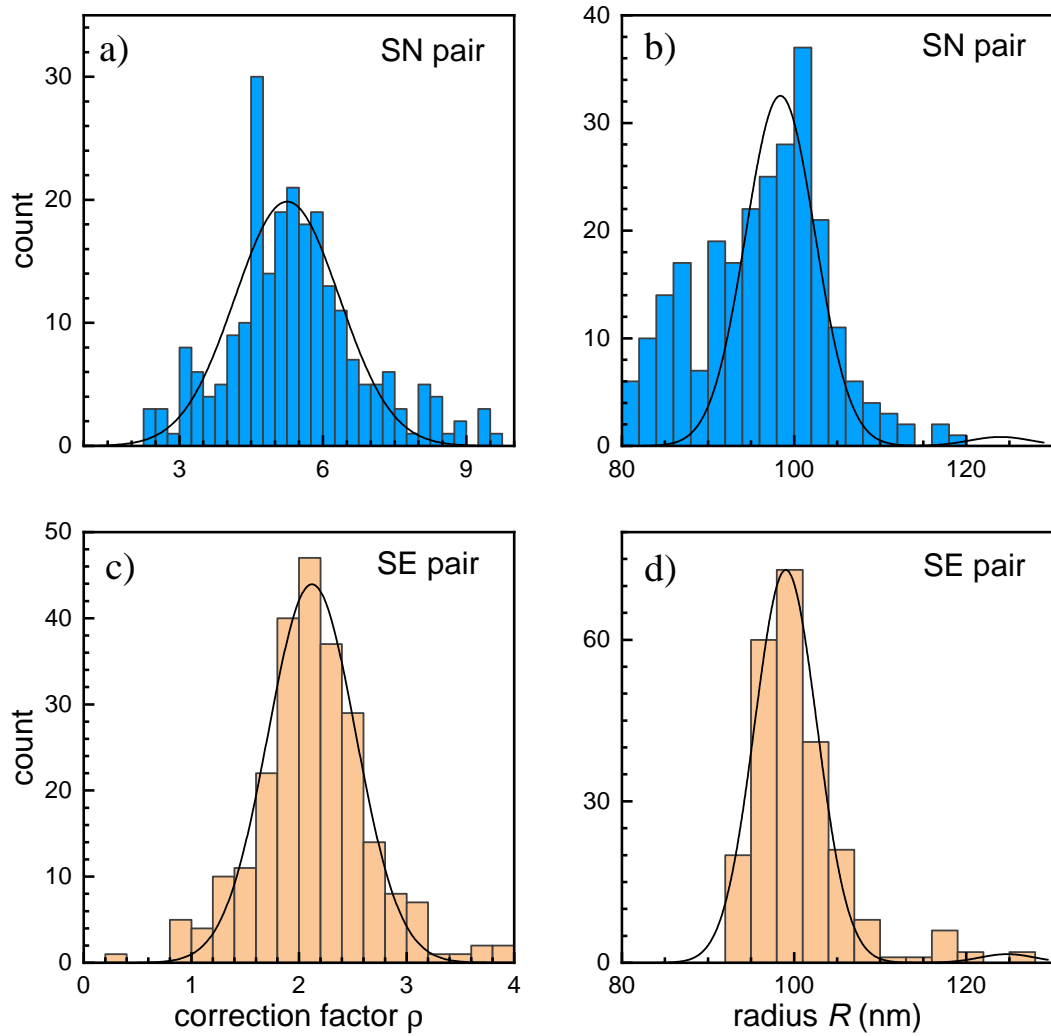
Figure 3.11: Histograms of the correction factors and corrected radii for the 100 nm radius PS beads immersed in water oil imaged using the 1.27 NA objective and analysed using the SN (a, b) and SE (c, d) pairs.
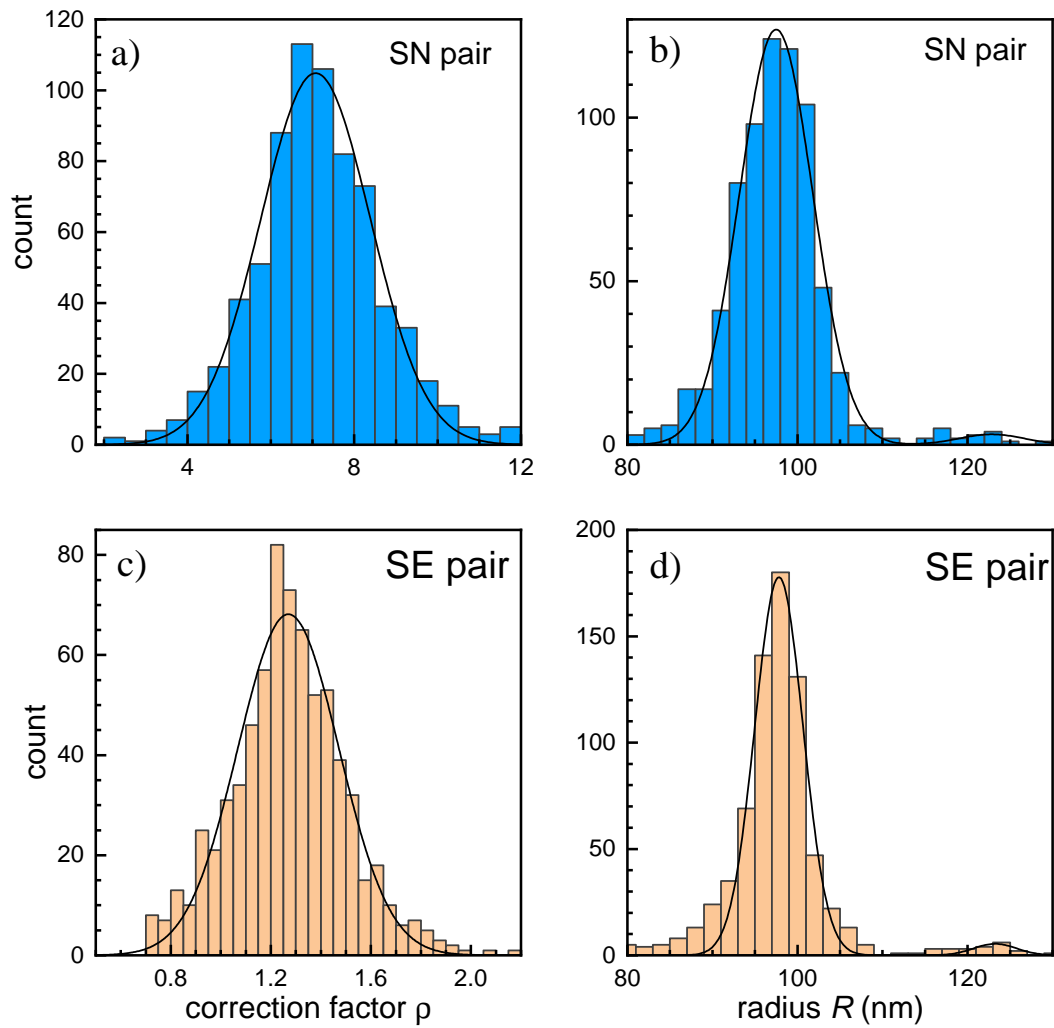
Figure 3.12: Histograms of the correction factors and corrected radii for the 100 nm radius PS beads immersed in silicone oil imaged using the 0.75 NA objective and analysed using the SN (a, b) and SE (c, d) pairs.
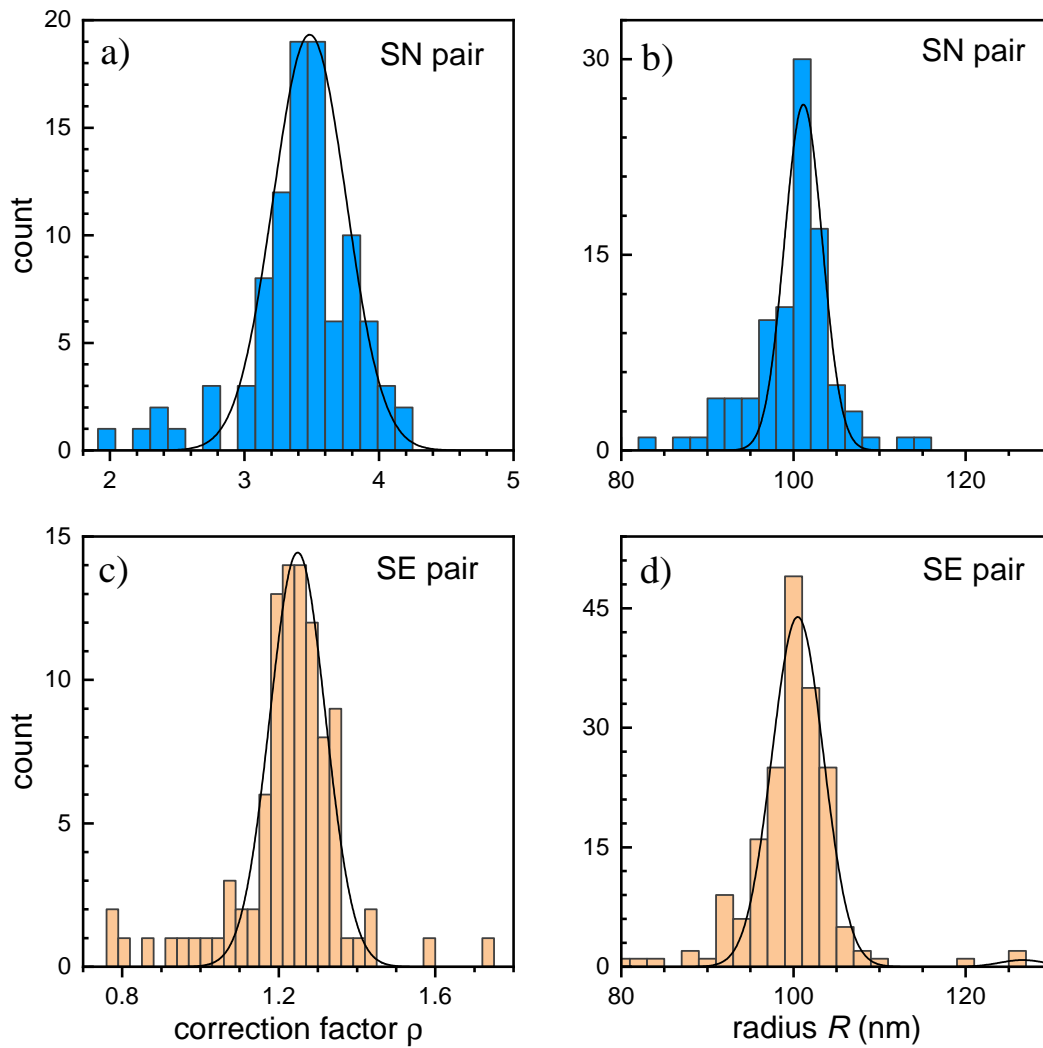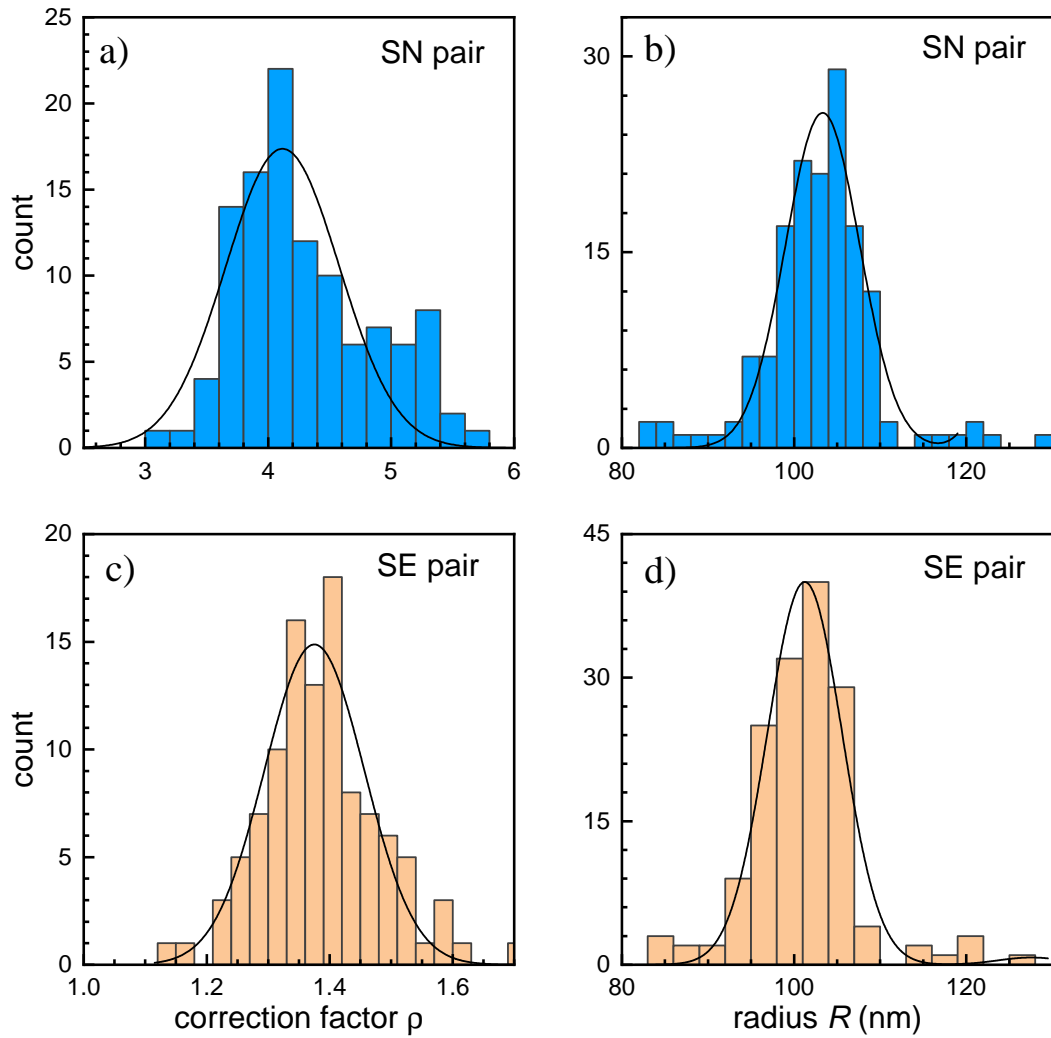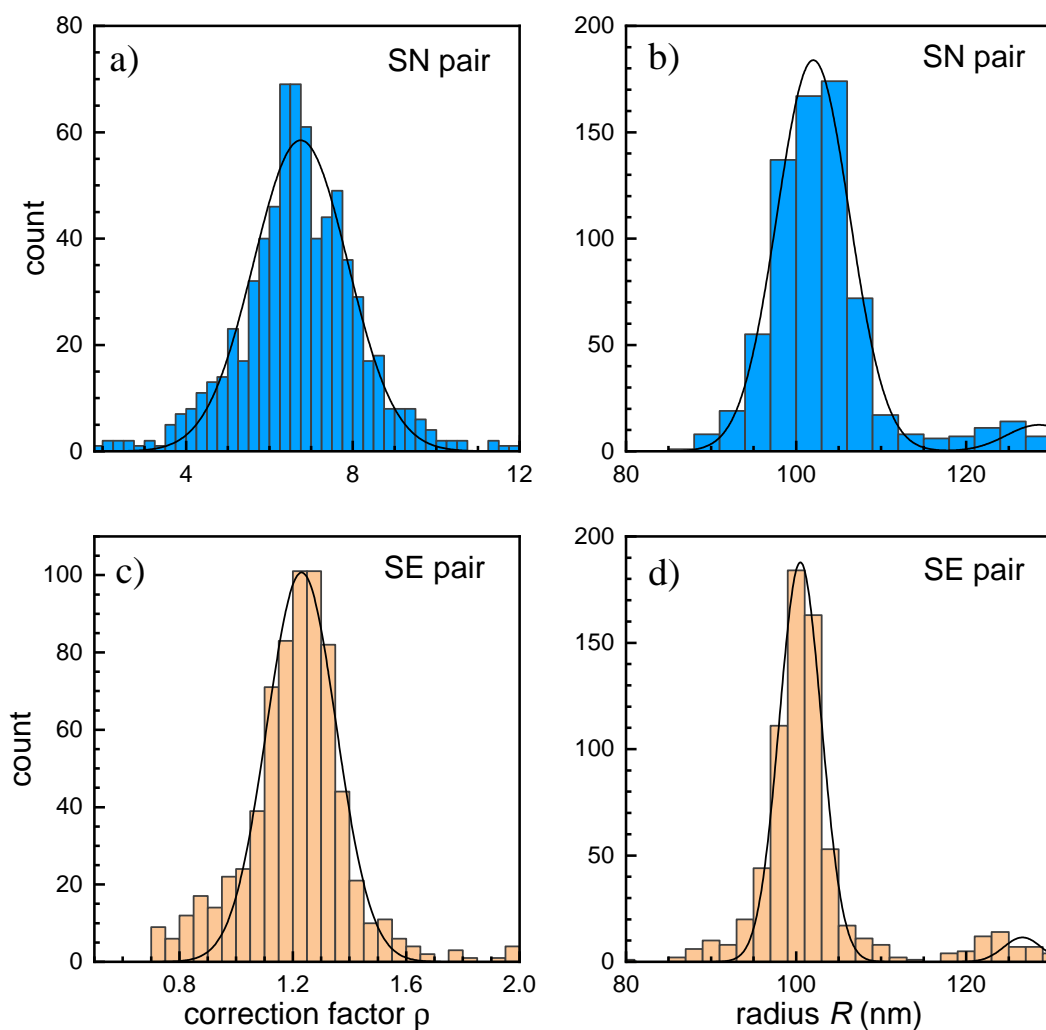
Figure 3.13: Histograms of the correction factors and corrected radii for the 100 nm radius PS beads immersed in water oil imaged using the 0.75 NA objective and analysed using the SN (a, b) and SE (c, d) pairs.
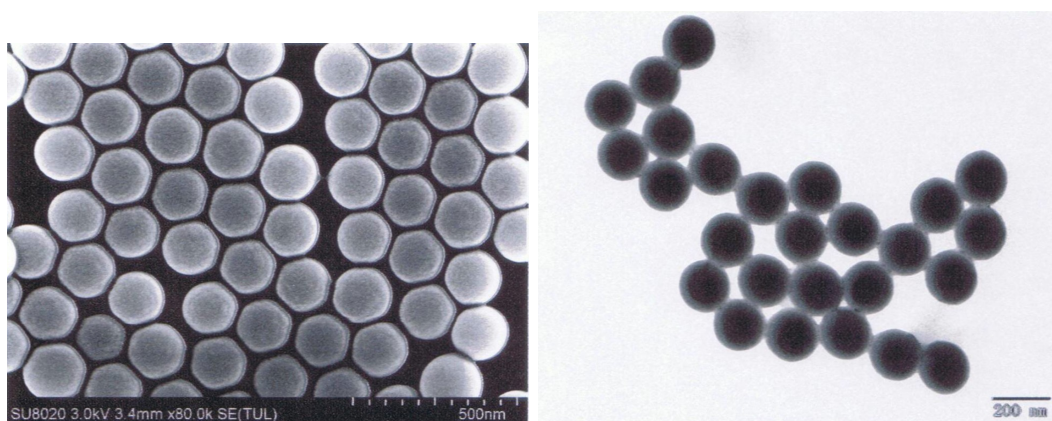

Figure 3.14: Scanning electron microscopy (Left) and transmission electron microscopy (Right) images of the 200 nm diameter PS beads obtained by the manufacturer.
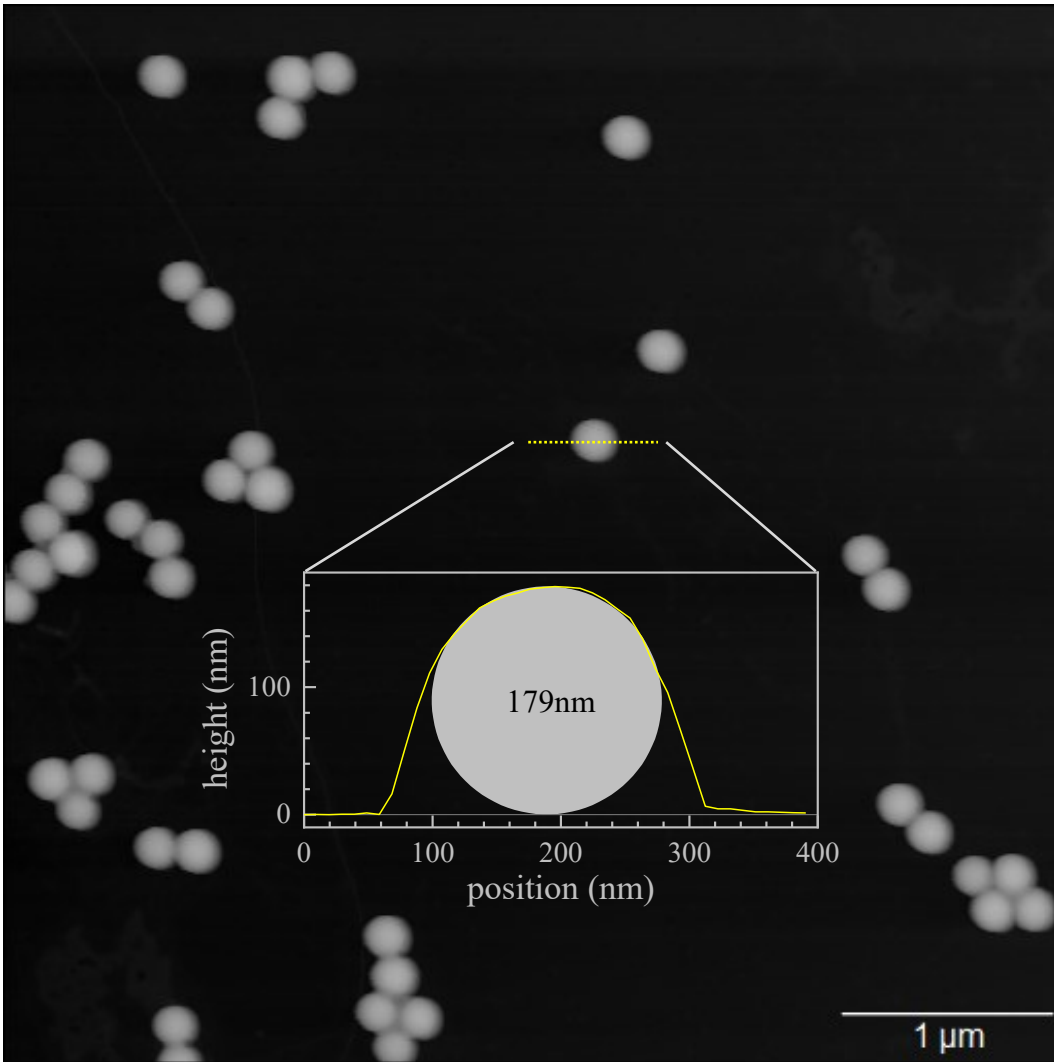
Figure 3.15: Atomic force microscopy image (m = 0 nm to M = 300 nm) showing the 200 nm radius PS bead sample. The height profile of a single bead with a diameter of 179 nm across the yellow dashed line, is shown in the inset with a 1:1 aspect ratio.

that obtained with the SE pair. This was caused by the correction factor of these SN pair measurements having a broader histogram, and therefore would cause increased error in the corrected radii obtained for individual beads.

When compared with the manufacturers specifications (radius of 100 nm with a cv of 3%), the sizes obtained here match well. This was confirmed by scanning electron microscopy (SEM) and transmission electron microscopy (TEM) images obtained by the manufacturer of the beads, as can be seen in Figure 3.14, which showed mean radii of 95 nm and 93.5 nm, respectively. Also obtained were atomic force microscopy (AFM) measurements using a Bruker Dimension Icon, seen in Figure 3.15, which showed a 5% smaller mean radius (89.5 nm) when compared to the SEM and TEM measurements. The slightly elliptical nature of the beads observed in the AFM image is most likely due to the tip used for the AFM measurements which has a finite sharpness, causing the width of the beads appear greater than their height.

3.5 Background and Shot Noise

Having determined the accuracy of the technique, it was also important to determine the precision of the measurements. This was determined by the photon shot noise, and the background due to additional structures on the sample such as glass roughness.

Discussing first photon shot noise, we know that the shot noise in I_c, σ_c is dependant upon the number of acquisitions, N_a, as well as the number of photoelectrons detected per pixel per readout such that $\sigma_c = 1/\sqrt{2N_eN_a}$. From this we can calculate from the maximum number of frames acquired here, $N_a = 256$, and given the number of photoelectrons on the order of 10^4, that $\sigma_c = 0.04\%$. Analysing also how the phase angle can have an impact on the noise Equation 2.5 can be used to find that

$$\sigma_c = \sigma_\delta \left| \frac{dI_c}{d\delta} \right| = \sigma_\delta \left| \frac{\sin(\psi)}{1 - \cos(\psi)} \right|. \tag{3.13}$$

This shows that the noise can be reduced by decreasing the phase angle used for the measurements, however, there is a trade off with this as at lower values of ψ the transmitted intensity of light is also reduced. Measurements using this setup have also shown that the optics are not ideal and of particular note is that some light is still transmitted at $\psi = 0$ degrees without sample present. This transmission was characterised for the objectives used, using measurements of the transmitted intensity obtained at phase angles of $\psi = \pm20$, ±30, ±60, and ±90 degrees, as well as at $\psi = 0$ degrees. The values for the mean intensity for the phase angles given, at regions with no particles present in the sample, and using all objectives discussed here were obtained and are shown in Table 3.1. Using the equations $\eta = f(\psi)\frac{1-\cos(\psi)}{2}$ and $f(\psi) = \frac{\langle I_0 \rangle}{\langle I_\psi \rangle - \langle I_0 \rangle}$, the background transmission fraction, η, was calculated for each phase angle and objective. The average background transmission fraction was found to be $\eta = 0.80\%$, 0.64%, and 0.86% for the 1.45 NA, 1.27 NA, and 0.75 NA objectives, respectively. Notably, from Equation 2.3 it can be calculated that for the lowest phase angle used, $\psi = 30°$, the transmitted intensity is only 6.7% that of I_{ex} meaning the background transmission found here makes up a significant proportion of the ideal transmission. It was therefore necessary to correct for η during the analysis by subtracting the background from the measured intensity, $I_\pm^m$, such that

$$I_\pm = I_\pm^m - \frac{\langle I_\pm^m \rangle 2\eta}{(1 - \cos(\psi))}. \tag{3.14}$$

To determine the noise due to the background, such as glass roughness, the integrated phase area for 1000 points were measured in regions with no polystyrene beads present. These background points were analysed in the same way as the beads using the SN and SE pairs. To determine then the standard deviation, σ, of the background a Gaussian fit was applied to the histograms plotted, as can be seen in the inset of Figure 3.16. This analysis was done for $N_a = 1$, 10, 100, and 256 frames. The resulting values for σ were fitted with the function

$$\sigma = \sqrt{\frac{\sigma_s^2}{N_a} + \sigma_b^2}, \tag{3.15}$$

where σ_s was the single frame shot noise, and σ_b was the background error, as seen in Figure 3.16.
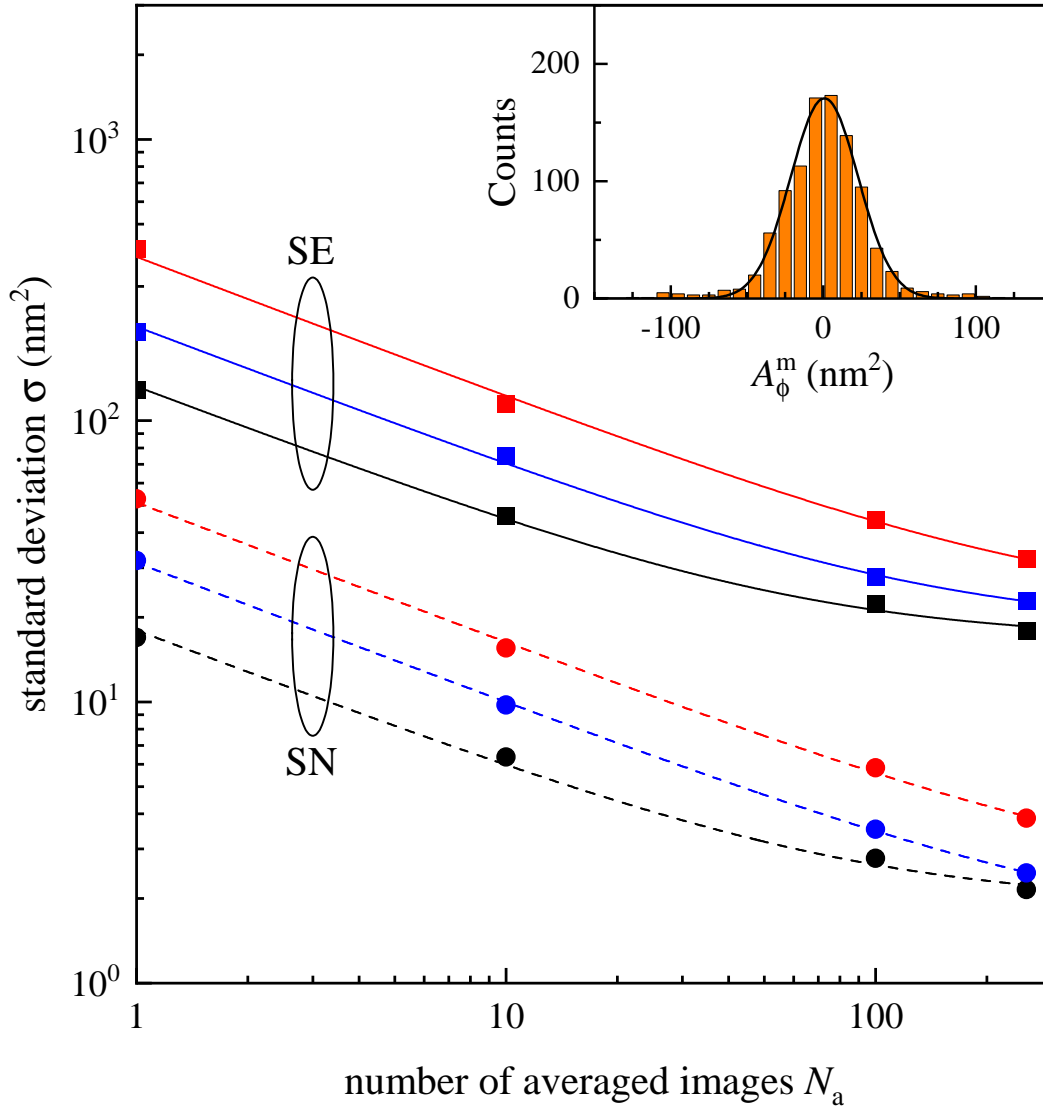
Figure 3.16: Standard deviation σ, from the distribution of A_ϕ^m in regions of the sample without PS beads, versus number of averages N_a, for PS beads mounted in silicone oil imaged using the 1.45NA objective and phase offsets ψ of 30 (black), 60 (blue), and 90 (red) degrees. The inset shows the histogram of A_ϕ^m for $N_a = 100$, analysed using the SE pair imaged at $\psi = 30$ degrees, and the fitted Gaussian distribution (black line).
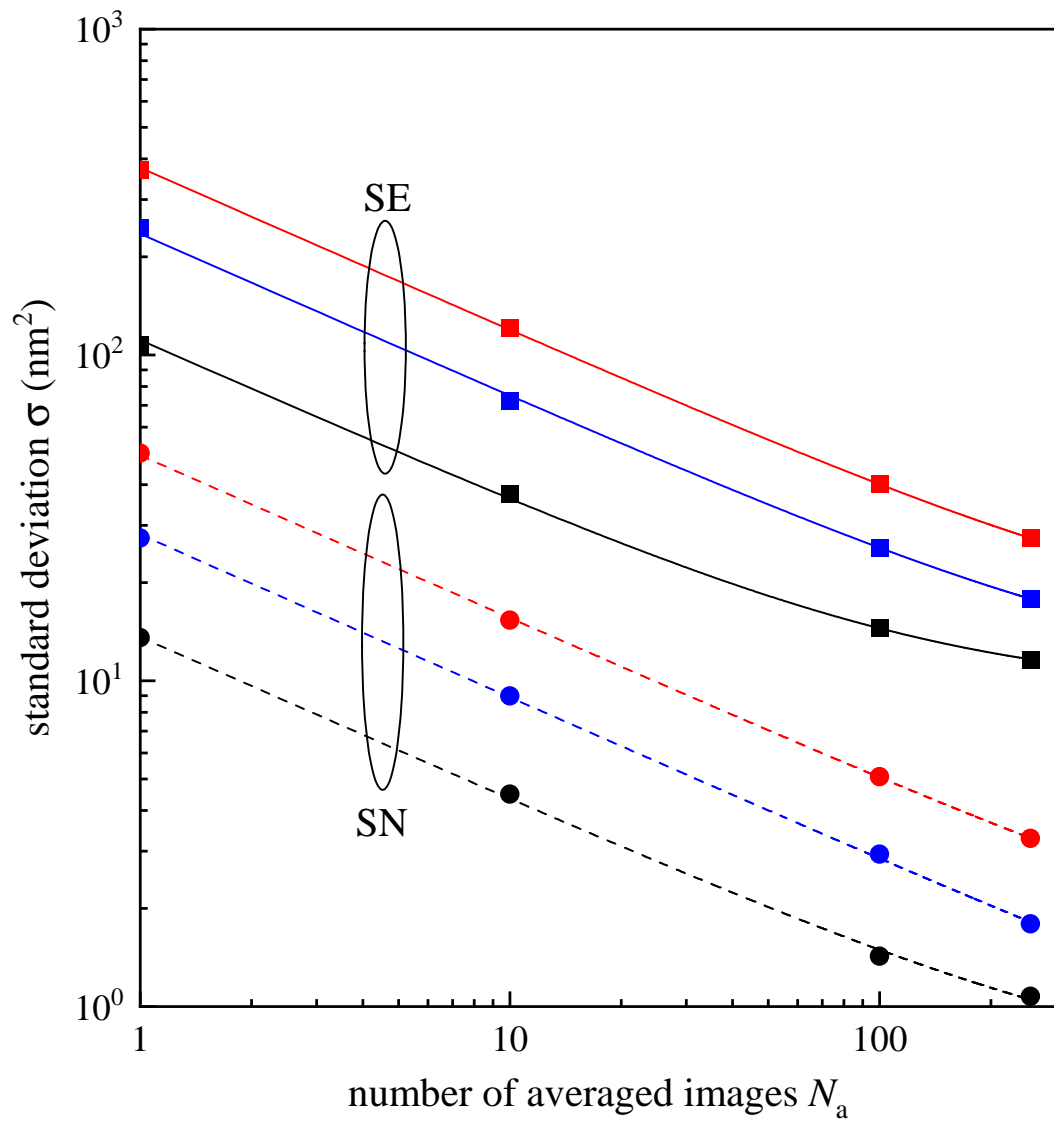
Figure 3.17: As Figure 3.16, but for the 1.27 NA objective
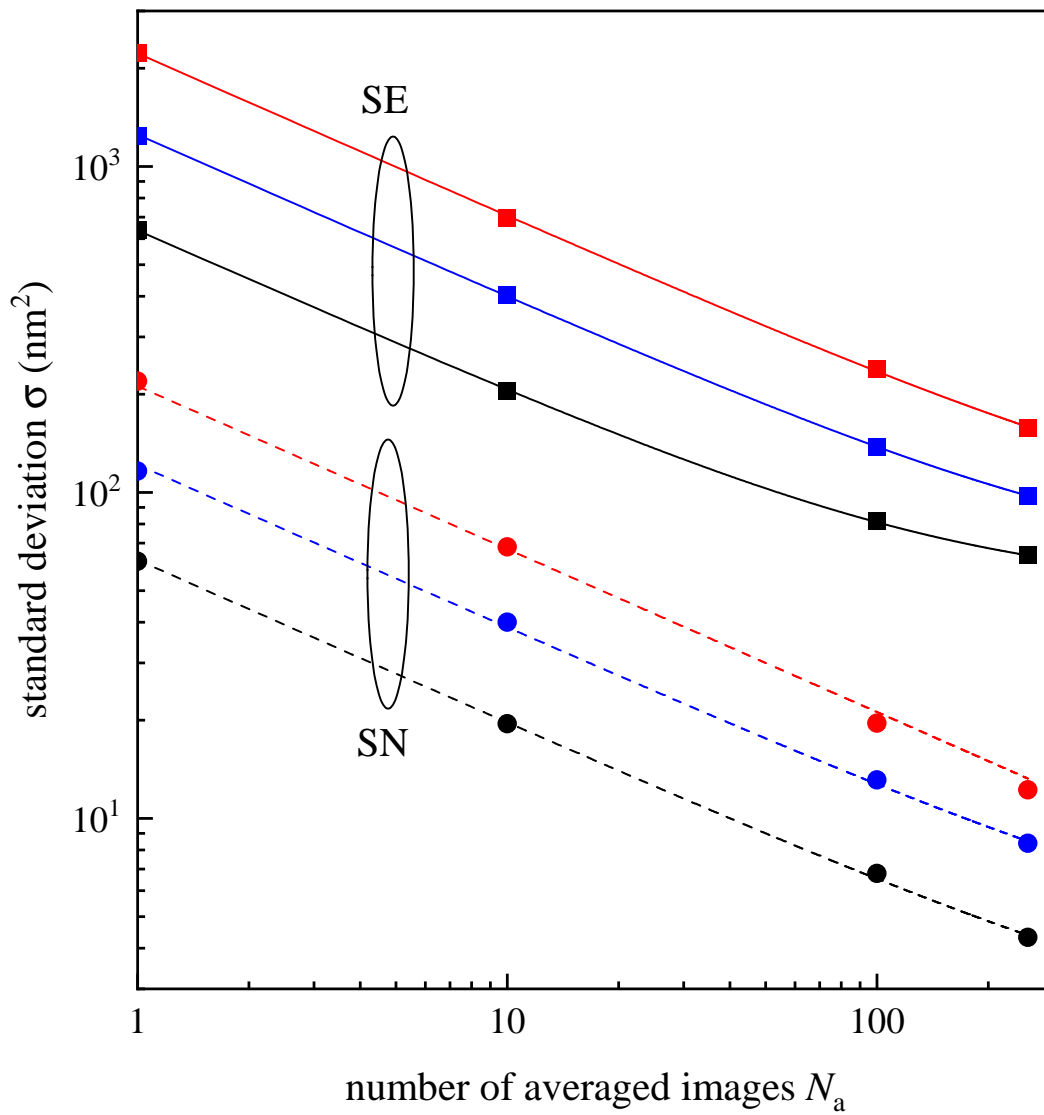
Figure 3.18: As Figure 3.16, but for the 0.75 NA objective
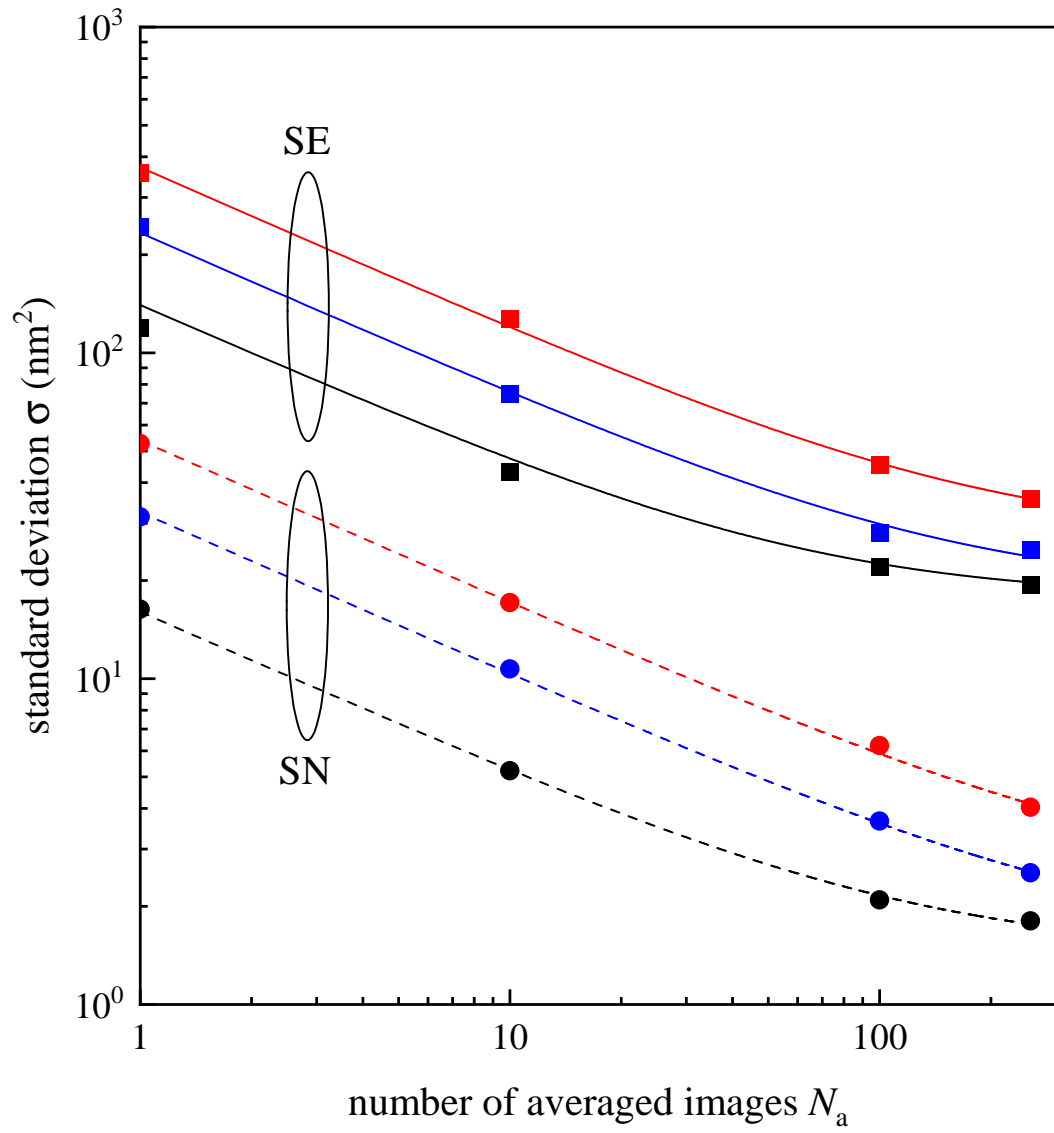
Figure 3.19: As Figure 3.16, but for the water oil mounted sample.
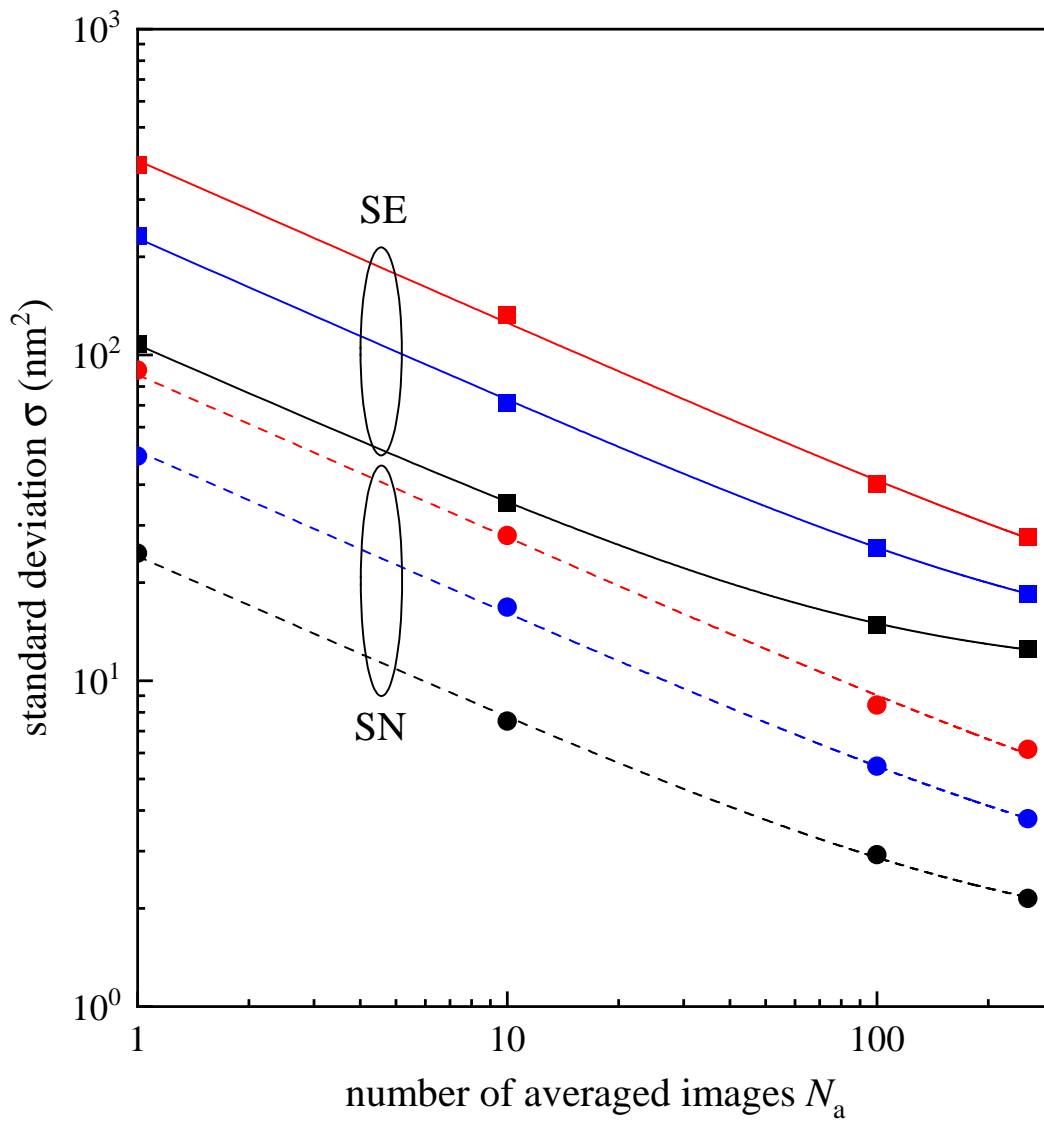
Figure 3.20: As Figure 3.17, but for the water oil mounted sample.
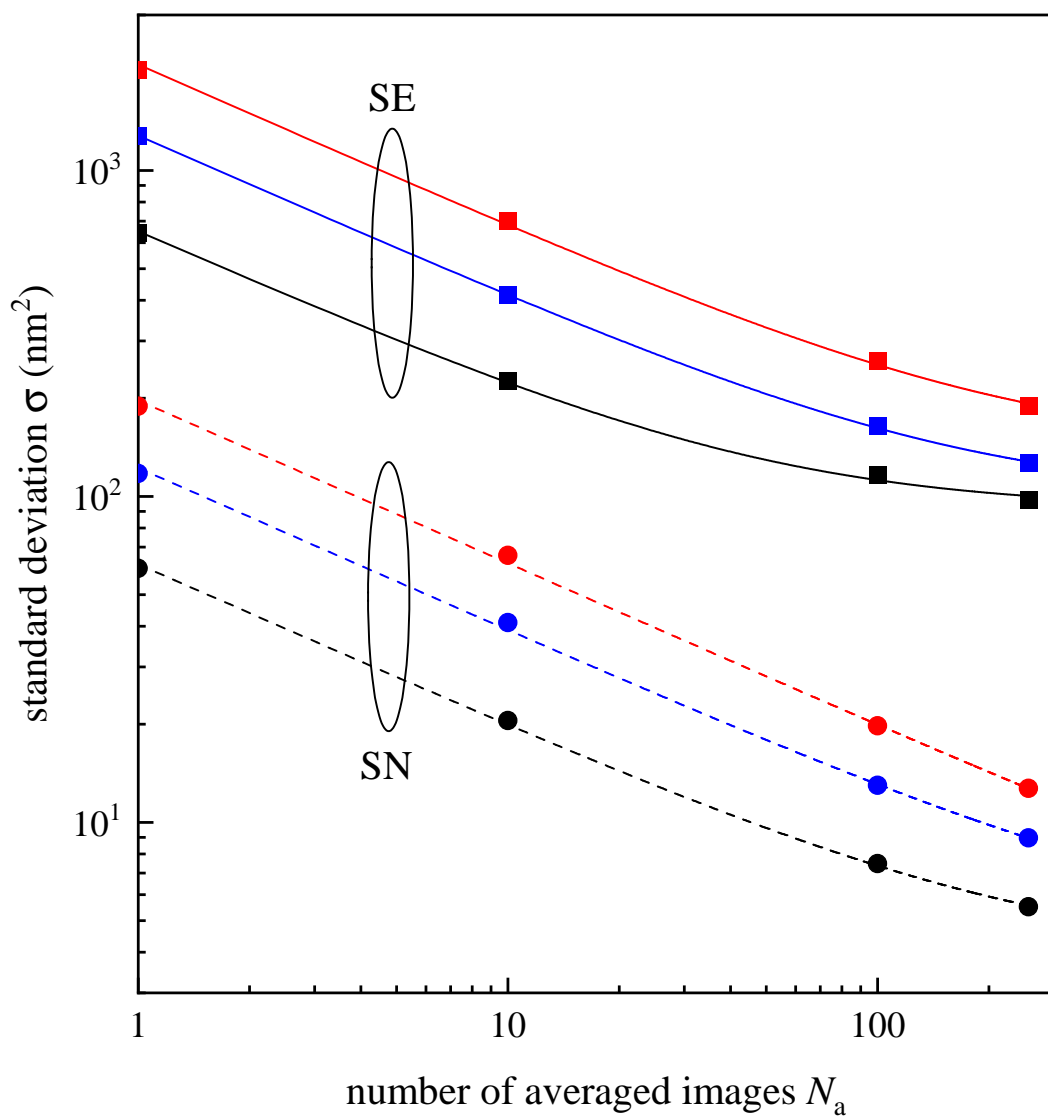
Figure 3.21: As Figure 3.18, but for the water oil mounted sample.
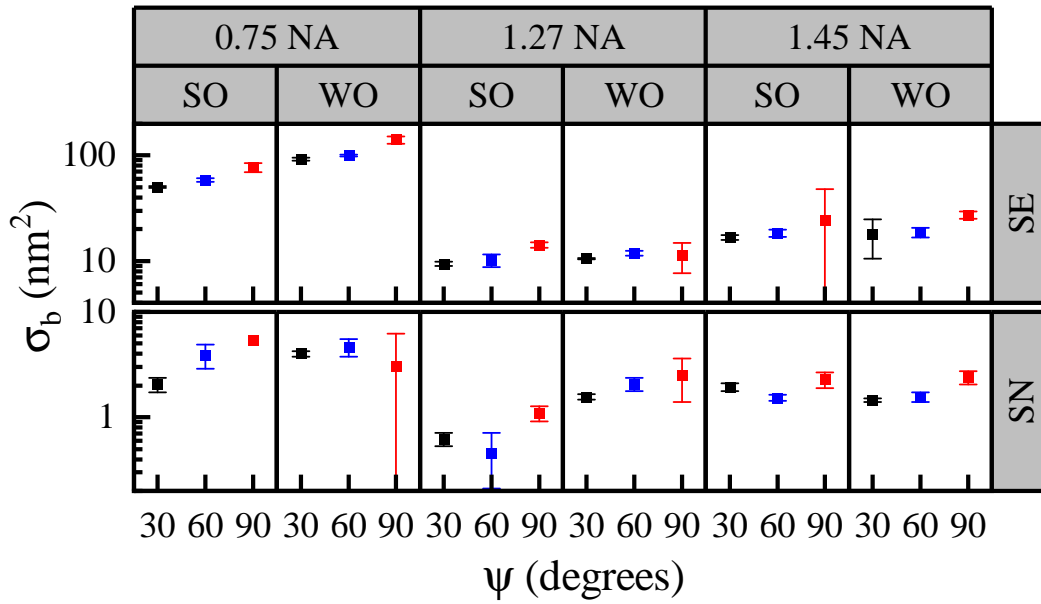
Figure 3.22: Overview of the background error σ_b for different phase angles ψ, objectives 0.75, 1.27, and 1.45 NA, water oil (WO) and silicone oil (SO) immersion, and analysis pairs SE and SN.

This showed that the noise decreased with the number of averages until $N_a > 100$ at which point a saturation is visible, indicating that the background error limit was reached. For the 1.45 NA objective, with the sample mounted in silicone oil, this background error was found to be $\sigma_b = 1.94$ and $16.66\,\mathrm{nm}^2$, corresponding to PS bead radii of 13 and 18 nm, when the SN and SE pairs were used for analysis, respectively. The values for σ_b for the other objectives and mounting oil can be seen in Table 3.2. From this it is clear that, given enough averages, the shot noise of the images can be lowered to a point such that the sensitivity limit is determined by the background error alone. In general, this background error is not limited by the phase angle used, as seen in Figure 3.22. However, for the 0.75 NA objective the background error appears to increase with increasing phase angle, though this is likely due to systematic errors in the measurements. Also strange is the similarity in values for σ_b between immersion oils. It was expected that, due to the similarity in refractive index between water oil and glass, the silicone oil measurements would have a higher background error due to the glass roughness being visible. The similarity in σ_b suggests that the background limit is likely due to residual impurities on the glass surface leftover from the cleaning procedure. Evidence of this can be seen from the similarity in smallest detectable radii found for the 1.27 NA objective, which were 8.8 and 8.7 nm for the silicone oil and water oil mounted samples, respectively. The best way to get around this background limit would be to have particles that could attach and detach from the coverslip surface. By doing this, there would be no glass roughness to limit the background error, as well as minimising the impurities seen in these measurements, allowing a sensitivity given by shot noise only.

To visualise the scaling of the shot noise presented in Equation 3.13, the single frame shot noise values found from Figure 3.16 were plotted against the phase angle. This can be seen in Figure 3.23, and shows the sensitivity increases as expected with

decreasing phase angle. The function

$$\sigma_s = \sigma_{s0} \left| \frac{1 - \cos(\psi)}{\sin \psi} \right| \tag{3.16}$$

is shown, with the noise at $\psi = 90$ degrees being σ_{s0}. Good fits were found for all objectives, with $\sigma_{s0} = 55$, 89, and $198 \, \text{nm}^2$ for the 1.45 NA, 1.27 NA, and 0.75 NA objectives, respectively. When using the SN pair for analysis, lower values for the single frame shot noise can be obtained, as seen in Table 3.2, with the lowest found being $\sigma_s = 14 \, \text{nm}^2$ equivalent to a 25 nm radius PS bead mounted in silicone oil. This was obtained when the 1.27 NA objective was used, with the sample mounted in silicone oil, and analysed using the SN pair. For the sample mounted in water oil, the smallest single frame shot noise was found when using the 1.45 NA objective at $\sigma_s = 16 \, \text{nm}^2$, equivalent to a PS bead of radius 17.5 nm. It is thus clear that σ_s can be reduced in three ways for this technique, these being to increase the NA of the objective which in turn improves the spatial resolution of images, to use the SN pair for analysis rather than the SE pair which improves the signal to noise ratio (as shown in Section 3.2), and to decrease the phase offset used for measurements giving an increased phase contrast for the particles. It can also be seen that due to the increased refractive index difference when using water oil as opposed to silicone oil, the size limit can also be reduced due to the increased refractive index difference. By using the example presented earlier where particles can detach from the surface of the coverslip, hence assuming the measurements are not limited by σ_b, and by increasing the number of averages obtained to $N_a = 1000$ it would be feasible to increase the sensitivity to observe PS beads of 3.8 nm radius for a phase offset of $\psi = 30$ degrees. An example of how this sensitivity could be improved further, assuming ideal optics where $\eta = 0$, would be to use a phase offset of $\psi = 1$ degree, to give a radius limit of 1.8 nm. It should be noted that the dependence described in Equation 3.16 only holds when the transmitted signal on the camera can be kept at the same level, meaning for the $\psi = 1$ degree example a lamp intensity of $100\times$ greater than would be required for measurements at $\psi = 10$ degrees is necessary due to the transmitted intensity scaling with $1/\psi^2$. As such this dependence breaks down the closer one gets to a phase offset of 0 degrees as it becomes harder to obtain sufficiently high transmitted signal on the camera.

3.6 30 nm PS Bead Measurements

In order to confirm the sensitivity of the qDIC technique, measurements of fluorescing 30 nm diameter PS beads, with a size distribution between 20 and 40 nm were carried out. For these measurements, a 1.49 NA $100\times$ objective was used with a phase offset of $\psi = 20°$. Fluorescence measurements of these beads were also carried at the same regions to confirm the position of the beads, as can be seen in Figure 3.25 (details of the measurements provided below). Analysis of the region seen in Figure 3.25a showed a noise of $\sigma = 1.6 \, \text{nm}^2$, with the dependence on the number of averages fitted by Equation 3.15 with $\sigma_s = 13.3 \pm 0.8 \, \text{nm}^2$ and $\sigma_b = 1.4 \pm 0.1 \, \text{nm}^2$. The errors for σ_s and σ_b discussed here were taken from the standard error of the fits applied in Origin graphing software, using Equation 3.15. The polystyrene bead which is clearly visible above the noise in the inset of the same Figure was found to have a radius of 24 nm. Figure 3.27a shows the distribution of measured particles (green histogram) and the background distribution (orange histogram) which had

Table 3.1: Table showing the median counts obtained for the different objectives and phase offsets ϕ, the resulting background fraction f, and background transmission factor η, as well as the average of η for each objective, $\bar{\eta}$.

ψ	$\langle I_0 \rangle$	$\langle I_{+\psi} \rangle$	$\langle I_{-\psi} \rangle$	$\langle I_{\psi} \rangle$	f	η (%)	$\bar{\eta}$ (%)
0.75 NA Objective						
30		467.54	401.70	434.62	0.13		
60	48.82	1524.29	1306.77	1415.53	0.04	0.89	
90		2898.64	2449.13	2673.89	0.02		
20		501.61	429.02	465.32	0.26		
30	95.83	891.65	764.52	828.09	0.13	0.86	
60		2904.75	2461.42	2683.08	0.04		0.86
10		655.61	517.93	586.77	1.10		
20	307.74	1597.09	1346.04	1471.56	0.26	0.85	
30		2808.64	2313.66	2561.15	0.14		
10	573.249	1220.24	953.61	1086.93	1.12	0.83	
20		2780.06	2648.03	2714.05	0.27		
1.27 NA Objective						
30		441.54	404.11	422.83	0.10		
60	37.33	1475.73	1366.07	1420.90	0.03	0.68	
90		2865.59	2523.26	2694.43	0.01		
20		465.95	426.96	446.46	0.19		
30	72.30	836.83	787.66	812.24	0.10	0.64	
60		2795.25	2517.54	2656.40	0.03		0.64
10		592.30	555.38	573.84	0.79		
20	253.68	1536.80	1493.51	1515.15	0.20	0.63	
30		2810.12	2635.14	2722.63	0.10		
10	495.112	1139.14	1106.46	1122.80	0.79	0.61	
20		2817.31	2937.73	2877.52	0.21		
1.45 NA Objective						
30		444.16	406.59	425.37	0.12		
60	46.77	1454.97	1297.56	1376.26	0.04	0.87	
90		2823.39	2417.96	2620.68	0.02		
20		477.74	428.47	453.11	0.25		
30	90.87	882.57	778.77	830.67	0.12	0.82	
60		2766.27	2502.96	2634.62	0.04		0.80
10		659.17	579.45	619.31	0.94		
20	299.38	1546.78	1461.34	1504.06	0.25	0.77	
30		2786.52	2579.88	2683.20	0.13		
10	568.738	1221.61	1097.11	1159.36	0.96	0.75	
20		2809.55	2738.49	2774.02	0.26		
1.49 NA Objective						
20	411	2801	1467	2134	0.24	0.72	0.96
30	337	2717	1619	2168	0.18	1.2	
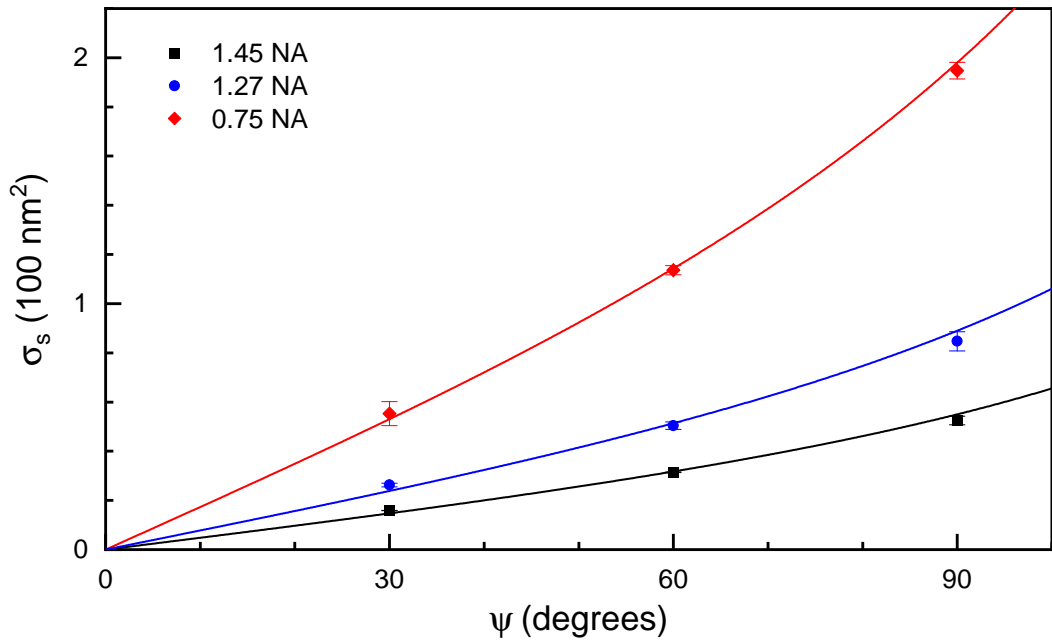
Figure 3.23: Single frame shot-noise σ_s of A_ϕ^{m} for the different objectives and phase offset angles, ψ, when analysed using the corresponding SN pair. The lines are fits using Equation 3.16.

been determined in the Extinction Suit software. The particles were identified by the software using the ImageJ prominence function, whereby the value for the smallest particle discernible by eye was chosen such that particles were analysed only when the prominence was above this value. The software then selected and analysed 1000 background positions which had not been identified as particles to obtain the background distribution. While the resultant distributions overlap, it can be seen that at $A_\phi^m > 4\sigma$ above the noise, the probability of obtaining this phase area without the presence of a particle is $p = 3 \times 10^{-5}$. As such, for a single field of view (assuming a spatial resolution, s, of around 300 nm) only two detections are expected without the presence of a particle, since $s/\sqrt{p} = 53\,\mu$m. This then means that the smallest reliably observable particle would need to have a phase area greater than the aforementioned 4σ limit which in the case of PS beads, with a refractive index of 1.59, corresponds to an 18 nm radius as shown in the grey shaded region of Figure 3.27b. From the particle size distribution, it can be seen that the number of particles with radii larger than 18 nm is decreasing, meaning the beads must have a mean radius < 18 nm, thus supporting the nominal 15 nm radius of the beads.

Measurements of the 30 nm beads showed they had peak excitation and emission wavelengths of 470 nm and 505 nm, respectively (as seen in Figure 3.24), measured using a spectrophotometer (Cary Eclipse). As such wide field epi-fluorescence measurements were carried out using a metal-halide lamp (Prior Scientific, Lumen L200/D) set at 10% of the maximum power. A Semrock GFP-A-Basic-NTE filtercube with an exciter filter transmitting the wavelength range 452-487 nm, and an emitter filter transmitting the range 510-549 nm, were used to limit the excitation and emission wavelengths to those required. This setup resulted in an illumination intensity of about $4\,\mathrm{W/cm}^2$ at the sample and allowed the positions of the beads to be confirmed. From Figure 3.25a and b, it can be seen that the particle present in the inset discussed before can also be seen in fluorescence indicating that a PS bead
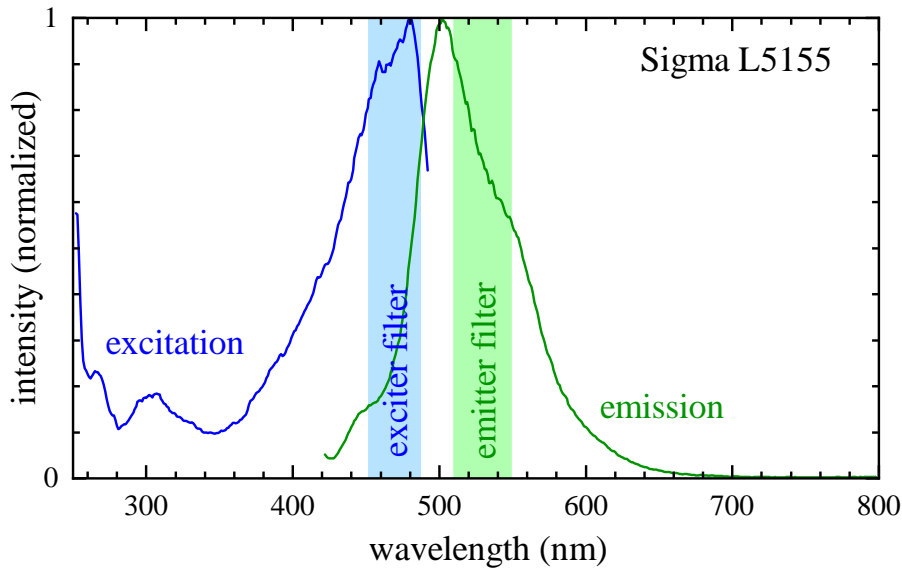
Figure 3.24: Fluorescence excitation and emission spectra of the 30 nm diameter beads.

is present in this position. Analysis of the particles observed in fluorescence was carried out in the same way as with the DIC measurements, using the dual radius integration method, such that the integrated fluorescence (A_{fl}) was obtained and converted from units of counts to photoelectrons. Figure 3.27c shows that there is a linear relationship between A_{fl} and A_ϕ^{m}, as was expected. It is worth noting that the beads lost their fluorescence on a timescale of hours when immersed in silicone oil, this was believed to be due to the lack of water tension allowing the fluorophore to disperse into the oil which could account for the apparent background fluorescence in Figure 3.25b. When the correlatively observed beads were plotted, as seen in Figure 3.27d, there were a significantly smaller number of beads observed below a radius of 20 nm when compared with qDIC measurements alone. This is likely due to the loss of fluorophore lowering the measured fluorescence of the small beads to below that of 4σ above the background A_{fl}.

As with the 200 nm diameter PS beads, measurements of 30 nm beads mounted in water oil were also carried out and can be seen in Figures 3.26 and 3.28. These measurements gave very similar results to those carried out in silicone oil for the bead radii, though the fluorescence distribution can be seen to be very different. It was also found that the detection limit for these measurements was very similar to those of the silicone oil mounted samples, which was likely due to the impurities on the glass surface. Also carried out were AFM and DLS measurements, as before, to confirm the size distribution of the beads. The histogram showing the size distribution found using AFM can be seen in Figure 3.30, and showed a mean size of 16 nm with a broad cv of 44%. Similarly to the 200 nm beads, the finite sharpness of the AFM tip has caused the beads to appear elliptical, though in this case the effect is more obvious, as can be seen in Figure 3.29. DLS measurements of these beads showed a mean of 24 nm and cv of 52%, this large mean size can be explained by the the large size distribution of the beads as has been demonstrated from the AFM results discussed previously. The broad distributions found for both the AFM and DLS measurements in this case, however, support the size distribution found from the qDIC measurements.
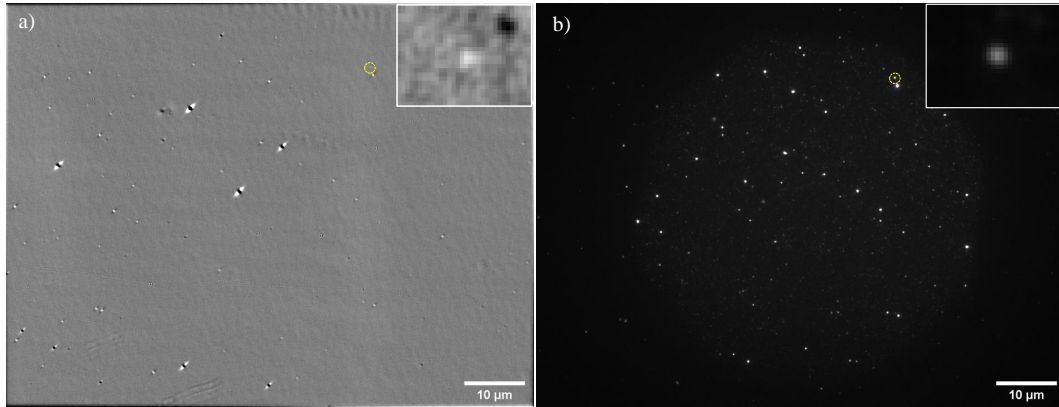
Figure 3.25: (a) qDIC phase $\phi(\vec{r})$ on fluorescent PS beads of nominally 15 nm radius, drop cast onto glass and surrounded by silicon oil, imaged with a 1.49 NA objective at a phase offset of $\psi = 20$ degrees and analysed using $\kappa = 1$ and $N_a = 256$. Grey scale from m = -1 mrad to M = 1 mrad. The inset shows a region of $(2.07 \text{ x } 1.55)\,\mu\text{m}^2$ around a bead highlighted by the yellow dashed circle, on a greyscale from m = -0.4 mrad to M = 0.4 mrad. This bead has an A_ϕ^m corresponding to a radius of 24 nm. (b) epi-fluorescence intensity I_{fl} (average of 5 frames with 3 s exposure time each) of the same sample region, on a greyscale from m = 41 to M = 1647 phe (photoelectrons). The excitation area was limited to the discernible disk region by a field aperture. Inset as in (a), greyscale m = 37 to M = 4177 phe.
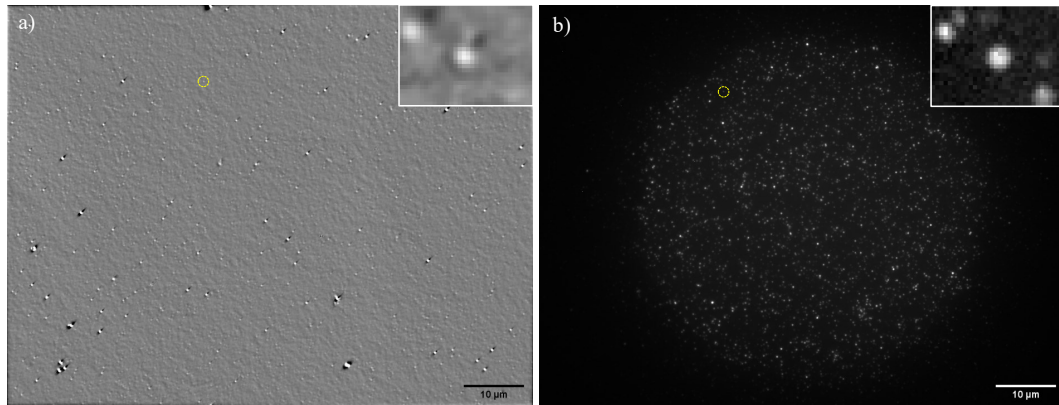
Figure 3.26: (a) qDIC phase $\phi(\vec{r})$ on fluorescent PS beads of nominally 15 nm radius, drop cast onto glass and surrounded by silicon oil, imaged with a 1.49 NA objective at a phase offset of $\psi = 20$ degrees and analysed using $\kappa = 1$ and $N_a = 256$. Grey scale from m = -1 mrad to M = 1 mrad. The inset shows a region of $(2.07 \text{ x } 1.55)\,\mu\text{m}^2$ around a bead highlighted by the yellow dashed circle, on a greyscale from m = -0.4 mrad to M = 0.4 mrad. This bead has an A_ϕ^m corresponding to a radius of 24 nm. (b) epi-fluorescence intensity I_{fl} (average of 5 frames with 3 s exposure time each) of the same sample region, on a greyscale from m = 41 to M = 3717 phe. The excitation area was limited to the discernible disk region by a field aperture. Inset as in (a), greyscale m = 41 to M = 1417 phe.
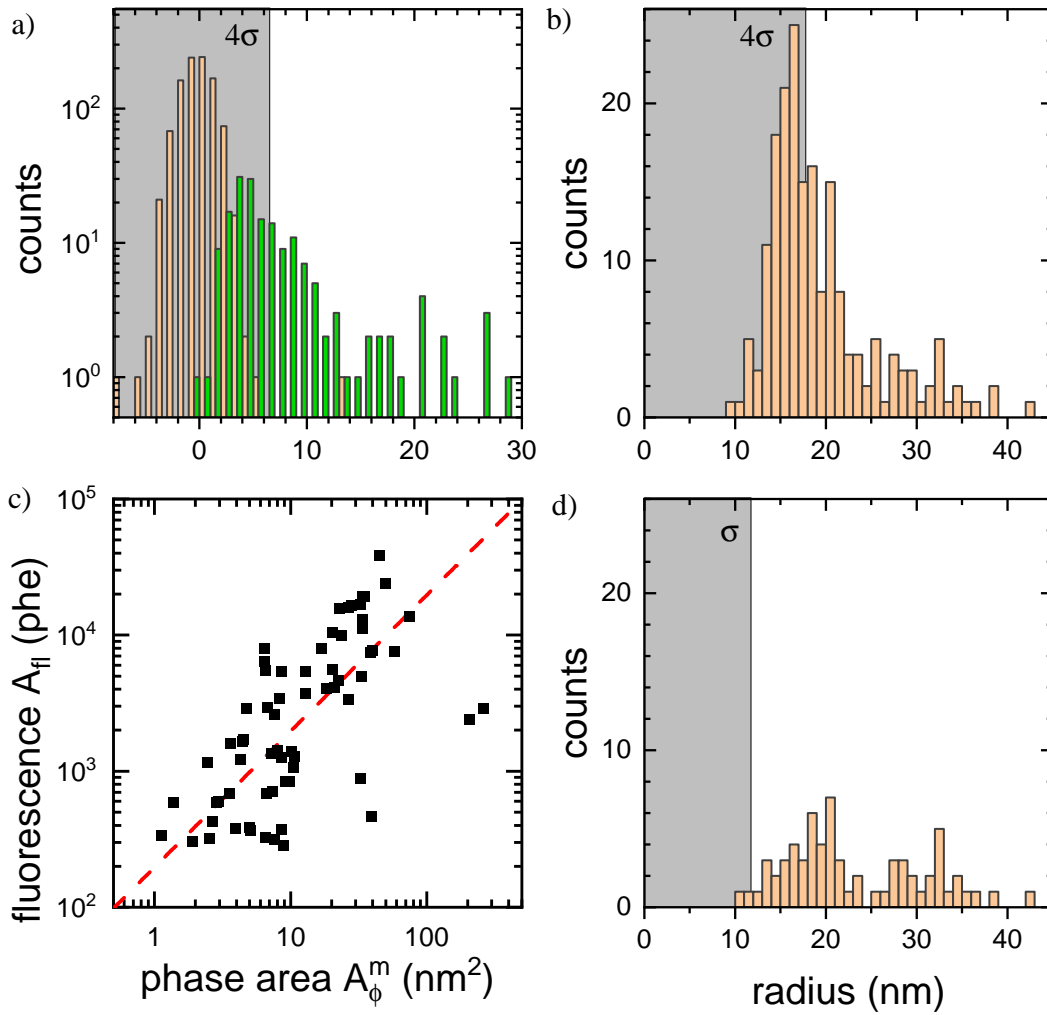
Figure 3.27: Analysis of data shown in Figure 3.25 (a) histogram of the phase area A_ϕ^{m} for background (orange, $\sigma = 1.6\,\mathrm{nm}^2$), and particles (green) located as maxima in $\phi(\vec{r})$ above 0.13 mrad. The region below 4σ is indicated in gray. (b) resulting histogram of particle radius. (c) fluorescence photoelectrons A_{fl} versus A_ϕ^{m}, with a proportionality indicated as dashed line. (d) Histogram of particle radius with corresponding A_{fl} above 274 phe.
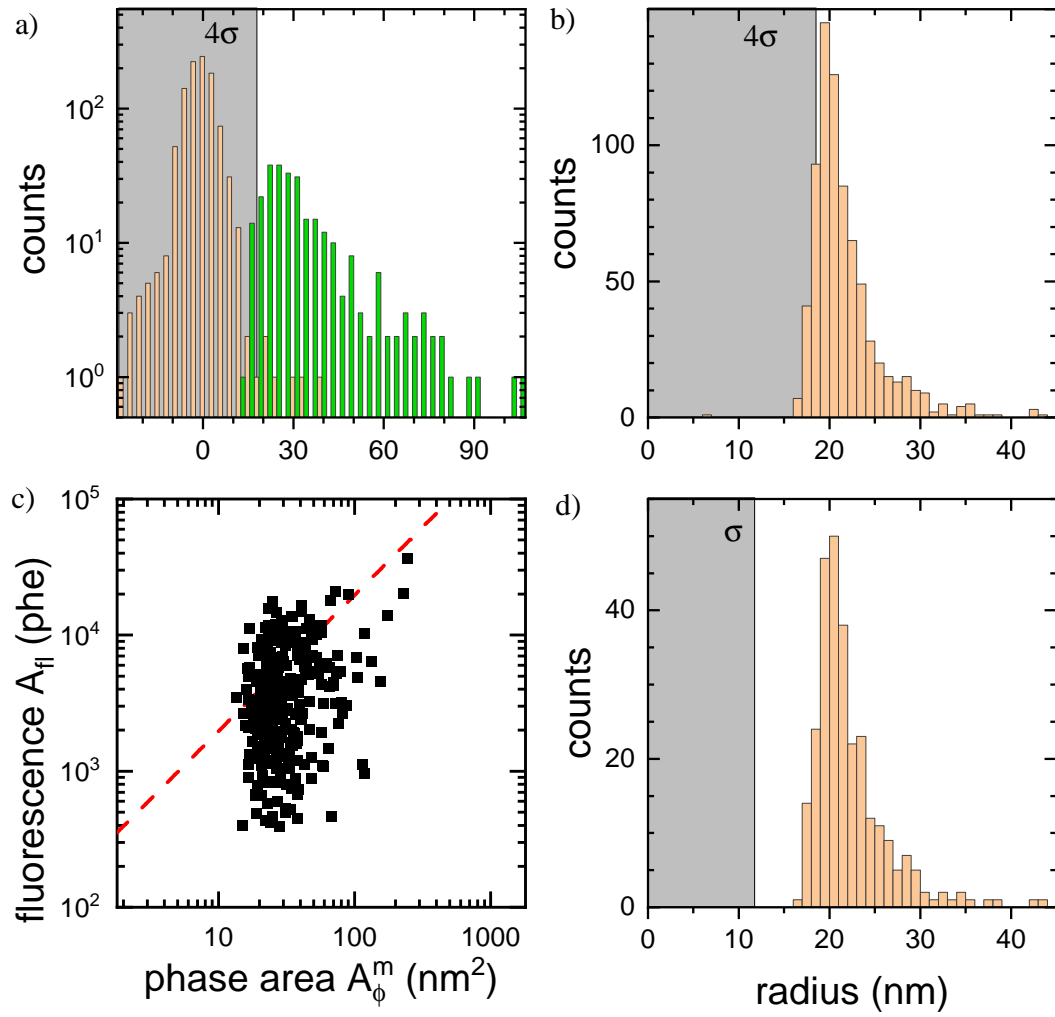
Figure 3.28: Analysis of data shown in Figure 3.26 (a) histogram of the phase area A_ϕ^{m} for background (orange, $\sigma = 1.6\,\mathrm{nm}^2$), and particles (green) located as maxima in $\phi(\vec{r})$ above 0.33 mrad. The region below 4σ is indicated in gray. (b) resulting histogram of particle radius. (c) fluorescence photoelectrons A_{fl} versus A_ϕ^{m}, with a proportionality indicated as dashed line. (d) Histogram of particle radius with corresponding A_{fl} above 455 phe.
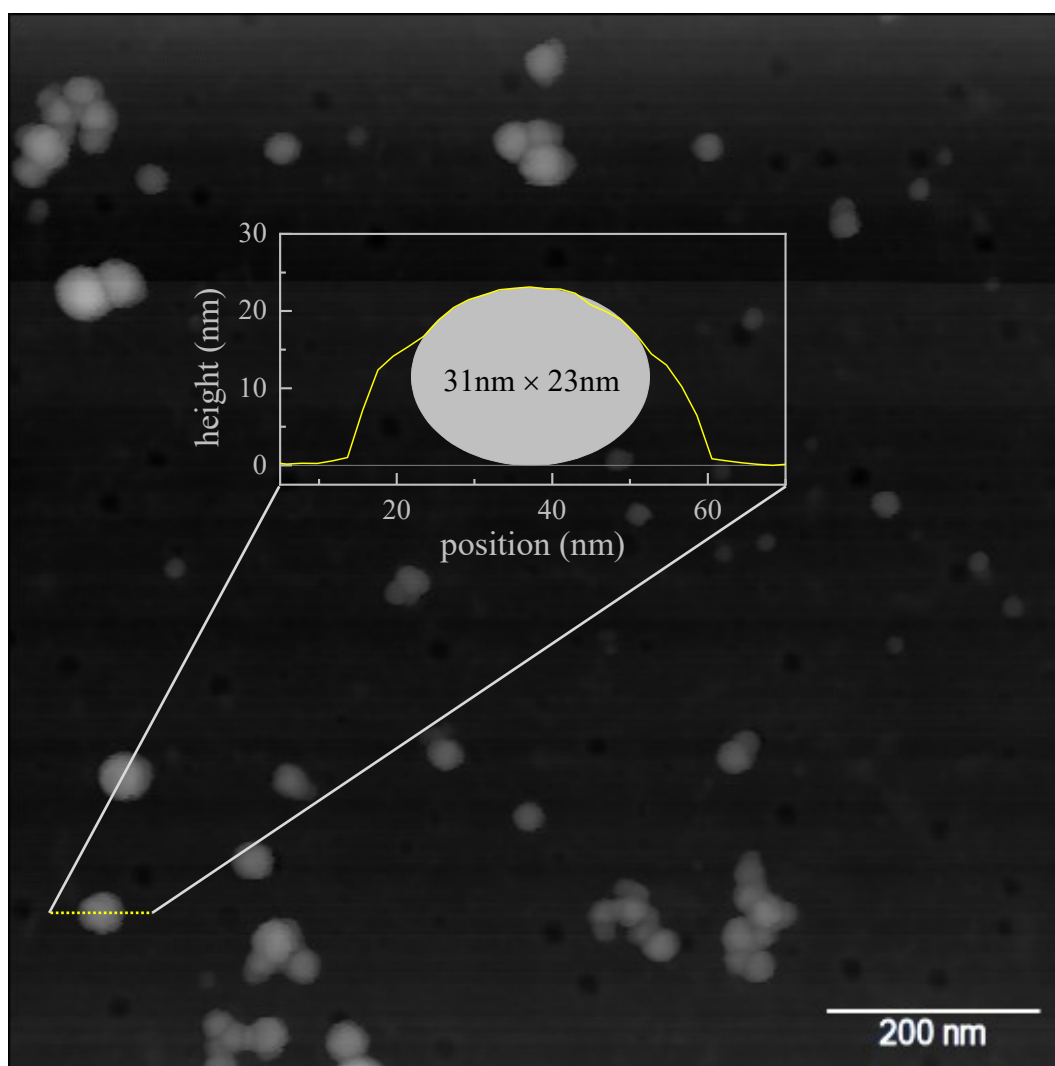
Figure 3.29: Atomic force microscopy image (m = 0 nm to M = 50 nm) showing the 30 nm
radius PS bead sample. The height profile of a single bead with an elliptical
shape of $(31 \times 23)\,\text{nm}^2$ across the yellow dashed line, is shown in the inset
with a 1:1 aspect ratio.
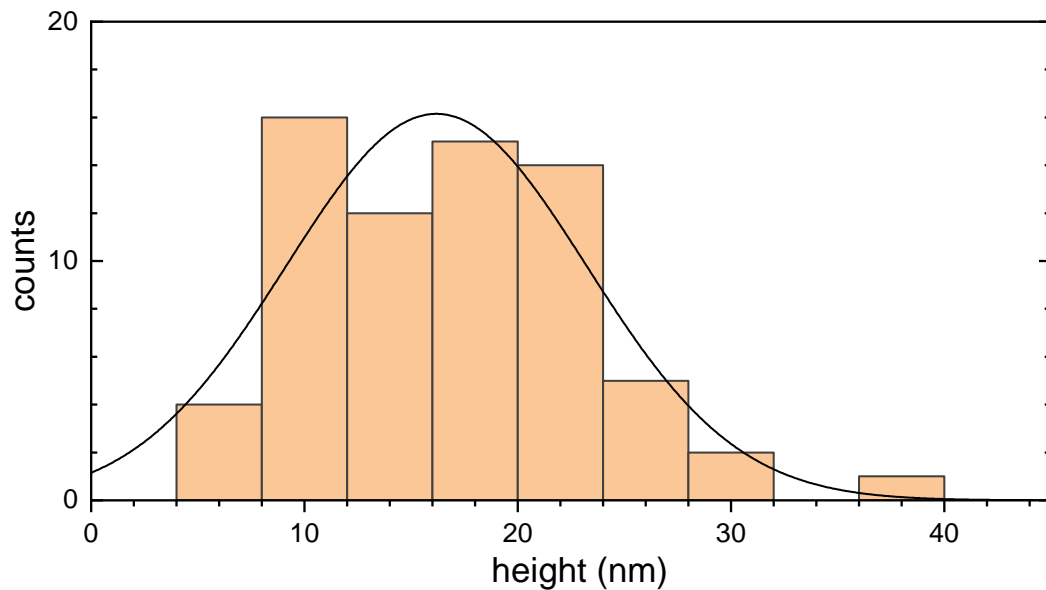
Figure 3.30: AFM height distribution of the 15nm radius bead sample, with a Gaussian fit of mean and standard deviation 16 ± 7 nm.

3.7 Limitations

It is worth noting the most relevant assumptions and limitations of this technique when sizing dielectric NPs. The first being that the particles measured were assumed to be smaller than the diffraction limit such that the particle size is independent of the PSF. This is due to the limitations of DIC at measuring long range phase gradients due to the technique being based on the spatial differential of the phase. It is also assumed that the refractive index is constant over the wavelength range. While this is not an issue in this case, due to the relative 10% bandwidth of the excitation light as well as the nature of the NPs measured for this thesis, birefringence could affect the phase contrast if aligned with the shear direction. For future measurements, a further quarter waveplate could be added both before and after the sample which would circularly polarise the light, for which the probed circular birefringence is weak in natural materials. This adjustment to the setup would also prevent the triple stripe pattern discussed in Section 3.2. Less relevant in this case, though still relevant to dielectric NPs more generally, is the assumption of an isotropic response from the particles. If particles were to have an elongated shape, an effect similar to birefringence would be seen due to the polarisability being dependant on the field orientation.

3.8 Conclusion

In conclusion, the analysis of the qDIC technique has been calibrated for the sizing dielectric particles. Using nominally 200 nm diameter polystyrene beads, the accuracy of the technique has been shown to be within a few nm, corresponding to a relative accuracy of a few percent when compared to other sizing techniques. The precision of the technique has also been shown, corresponding to a minimum detectable polystyrene bead radius of about 10 nm when the 4σ consideration is excluded, mostly limited by the background. However, by requiring the signal to

be a minimum of 4σ above the background for reliable identification, polystyrene beads with a minimum radius of 18 nm can be observed. This lower limit is due to the background structures on the glass surface to which the particles were deposited onto. To get around this, the particles could attach to and detach from the glass surface dynamically, meaning the background could be subtracted over the course of an acquisition rather than relying on a local background subtraction. For a total of 1000 frames this shot noise could be reduced to where 4 nm radius polystyrene beads could be measured. Higher sensitivities can also be achieved by reducing the phase angle used for measurements, possibly allowing polystyrene beads of 2 nm radius to be measured.

Table 3.2: qDIC results for 200 nm PS beads: correction factors ρ, particle integrated phase area A_ϕ and radii R with standard deviations, as well as shot noise σ_s and background noise σ_b. Results for different mounting media, objective NA, phase offset ψ, and analysis pair are shown. The radius limit was calculated from σ_b using $A_\phi = \rho \sigma_b$.

ψ	NA	Pair	κ	r_i	ρ	A_ϕ (nm^2)	R (nm)	σ_s (nm^2)	σ_b (nm^2)	Radius limit (nm)
						silicone oil =1.518				
30	0.75	SN	1	1	7.07	3193.4	97.5 ± 4.30	62.0 ± 1.3	2.05 ± 0.32	16
		SE	100	2	1.27	3164	97.2 ± 4.5	634.7 ± 4.7	50.39 ± 0.85	27
	1.27	SN	1	1.5	3.76	3466.1	100.2 ± 4.4	13.61 ± 0.41	0.62 ± 0.09	8.8
		SE	100	2	1.63	3539.3	100.9 ± 3.5	110.7 ± 2.6	9.36 ± 0.44	16
	1.45	SN	1	2.5	3.48	3570.9	101.2 ± 2.2	17.9 ± 1.0	1.94 ± 0.17	13
		SE	200	4	1.25	3497.3	100.5 ± 3.0	131.3 ± 5.1	16.66 ± 0.87	18
60	0.75	SN	1	1	7.07	4045.7	105.5 ± 5.7	121.5 ± 3.9	3.9 ± 1.0	20
		SE	100	2	1.27	3518.2	100.7 ± 3.4	1250.6 ± 10.5	58.6 ± 2.1	28
	1.27	SN	1	1.5	3.76	2907.6	94.5 ± 4.1	28.11 ± 0.55	0.46 ± 0.25	7.9
		SE	100	2	1.63	3105.8	96.6 ± 4.2	235.3 ± 6.5	10.1 ± 1.4	17
	1.45	SN	1	2.5	3.48	3549.8	101.0 ± 2.3	31.21 ± 0.50	1.53 ± 0.10	12
		SE	200	4	1.25	3486.9	100.4 ± 2.5	215.1 ± 8.8	18.4 ± 1.5	19
90	0.75	SN	1	1	7.07	4011.3	105.2 ± 5.4	212 ± 13	0.0 ± 5.4	22
		SE	100	2	1.27	3507.8	100.6 ± 4.4	2222 ± 30	77.2 ± 7.3	31
	1.27	SN	1	1.5	3.76	2639	91.5 ± 4.2	49.17 ± 0.55	1.17 ± 0.18	11
		SE	100	2	1.63	2735.7	92.6 ± 4.7	375.4 ± 3.9	14.14 ± 0.91	19
	1.45	SN	1	2.5	3.48	3645.5	101.9 ± 2.1	51.1 ± 1.8	2.27 ± 0.38	13
		SE	200	4	1.25	3602.8	101.5 ± 2.5	361 ± 13	24 ± 24	21
						water immersion oil =1.334				
30	0.75	SN	1	1	6.75	13000.1	102.0 ± 4.3	61.8 ± 1.4	4.00 ± 0.24	13
		SE	100	2	1.23	12434.9	100.5 ± 2.5	644 ± 17	91.9 ± 3.0	21
	1.27	SN	1	1.5	5.26	12103.9	99.6 ± 4.2	24.03 ± 0.54	1.56 ± 0.09	8.7
		SE	100	2	2.12	11922.5	99.1 ± 3.7	106.94 ± 0.86	10.52 ± 0.14	12
	1.45	SN	1	2.5	4.12	12472.1	100.6 ± 5.5	15.98 ± 0.37	1.45 ± 0.06	7.9
		SE	200	4	1.38	12711.7	101.2 ± 4.3	139 ± 45	17.7 ± 7.2	13
60	0.75	SN	1	1	6.75	12031.1	99.4 ± 3.6	122.3 ± 3.8	4.66 ± 0.88	14
		SE	100	2	1.23	10940.2	96.3 ± 2.8	1276 ± 14	100.0 ± 2.4	22
	1.27	SN	1	1.5	5.26	10838.3	96.0 ± 5.1	50.6 ± 1.4	2.07 ± 0.29	9.6
		SE	100	2	2.12	11008.5	96.5 ± 4.5	227.7 ± 3.4	11.83 ± 0.65	13
	1.45	SN	1	2.5	4.12	14019.8	104.6 ± 5.6	32.43 ± 0.80	1.56 ± 0.16	8.1
		SE	200	4	1.38	15431.8	108.0 ± 4.2	233 ± 12	18.7 ± 2.0	13
90	0.75	SN	1	1	6.75	11145.9	96.9 ± 4.2	197.2 ± 6.5	3.1 ± 3.1	12
		SE	100	2	1.23	10272.6	94.3 ± 2.9	2108 ± 61	141 ± 11	24
	1.27	SN	1	1.5	5.26	11249.8	97.2 ± 5.4	86.8 ± 3.6	2.5 ± 1.1	10
		SE	100	2	2.12	11284.6	97.3 ± 4.6	395 ± 13	11.8 ± 3.5	13
	1.45	SN	1	2.5	4.12	14923.1	106.8 ± 4.4	53.8 ± 1.7	2.39 ± 0.35	9.3
		SE	200	4	1.38	14425.7	105.6 ± 5.7	370 ± 13	27.2 ± 2.2	15

Chapter 4

Diamond sp2/sp3 Ratios

4.1 Introduction

Nanodiamonds have many medical and bio-imaging applications due to their low cytotoxicity, ease of surface functionalisation, mechanical strength, and presence of fluorescing defects such as nitrogen vacancy centres [51, 52, 71]. However, the applications of NDs extends beyond these fields having quantum, industrial, and electrochemical uses among others. Surface sp2 can have a detrimental effect on the desired properties of NDs. Most prominent of which for medical and bio-imaging applications are the suppression of fluorescence from NV centres, and the increased cytotoxicity associated with sp2 carbon [46, 75]. The amount of sp2 present in each ND is heavily dependant on the method used to synthesise them, with techniques such as detonation synthesis producing a higher level of surface sp2 than HPHT or CVD synthesis, followed by ball milling [35]. Processes to remove surface sp2 have been well established in literature, using combinations of air annealing and acid etches to remove defects from NDs, however, methods to quantitatively ascertain the sp2 content of individual nanodiamonds has not yet been reported on to the best of the author's knowledge [43, 44]. Raman spectroscopy can be used as a qualitative method to determine how much sp2 is present in ensembles of NDs, while recent developments of a combination of XPS and Raman spectroscopy can be used to quantitatively calculate the surface sp2 present in bulk diamond [39, 42]. However, due to the limitations of XPS, this technique is only capable of measuring a few nm into the surface of a material.

Optical extinction microscopy has previously been shown to be capable of providing quantitative information of individual NPs [128]. However, as has been discussed in Section 3.1, this technique is more sensitive to highly absorbing nanoparticles, where the absorption cross section is approximately equal to the extinction cross section thus having a negligible scattering cross section. As such, this technique would not be able to provide an accurate measurement of the sp2 content for individual nanodiamonds due to the highly scattering nature of the NDs themselves. However, this technique can be used to size individual NPs which are purely made up of sp2 which is highly absorbing. Given the calibration reported on in Chapter 3, of the qDIC technique for sizing individual dielectric NPs, it is possible to size individual NDs using this method instead. It is important to note that, again, this technique alone could not be used measure the sp2/sp3 ratio of individual NDs as the sp2 present on the surface of the NDs does not provide a phase contrast due to it being highly absorbing.

Photothermal artefacts have been shown to be present as a background in SRS measurements, due to the absorption of the Stokes beam causing a localised heating around the measured particles, in turn causing a lensing effect which modulates the incoming pump beam. This modulation is recorded as additional SRL, as the pump beam diverges and is cut off by the aperture [169]. Observations of this lensing effect have been made recently during SRS measurements carried out on PS beads and gold NPs, and has been used previously to quantitatively detect gases such as hydrogen with high sensitivity [170, 171, 172]. Presented in this chapter is a method whereby quantitative sp2/sp3 ratios of individual NDs can be ascertained using a combination of optical microscopy techniques, with extinction microscopy and qDIC used to size pure sp2 NPs and NDs, respectively. This was followed by correlative photothermal measurements of both samples to ascertain the response to a given amount of sp2, and hence the sp2 content of the NDs.

4.2 Nanodiamond qDIC and Photothermal Measurements

4.2.1 Average Nanodiamond Volumes

Applying the calibration of qDIC technique to NDs, the three treated samples as discussed in Section 2.1.4 mounted in silicone oil were measured. For the (0 - 150) nm and (0 - 250) nm samples the 0.75 NA objective was used with a phase offset of $\psi = 30°$, while for the (0 - 50) nm sample the 1.27 NA objective was used with a phase offset of $\psi = 60°$. These objectives were used rather than the 1.45 NA objective during these experiments to prevent saturation of the signal from the NDs, which would have caused an underestimation of the ND sizes. It should be noted that for this case, preventing saturation is not as simple as reducing the lamp power. As is discussed in Section 2.2.1 to ensure minimal shot noise, and to maintain consistency with the calibration carried out in Chapter 3, the counts on the camera were to be maintained close to the full well capacity as possible (2900 counts in this case). For each, stacks of 256 images were obtained and analysed using the SE pair as described in Section 3.2. The resulting size distributions for each sample are shown in Figure 4.1, and show an exponential decay in the number of particles measured as the volume of the particles increased. As such, an exponential fit was applied to each such that the number of particles for a certain volume was given as $p = p_0 \exp(-V_p/\bar{V})$, with $\bar{V}$ being the average volume for each sample. The mean volumes were thus found to be $2.1 \times 10^4 \, \text{nm}^3$, $2.4 \times 10^5 \, \text{nm}^3$, and $4.1 \times 10^5 \, \text{nm}^3$ for the (0 - 50) nm, (0 - 150) nm, and (0 - 250) nm samples, respectively. Converting this to an average size for each sample was done using $S = \sqrt[3]{\bar{V}}$, due to diamonds having a brick like shape, which yielded average sizes of 27.6 nm, 62.1 nm, and 74.3 nm for the (0 - 50) nm, (0 - 150) nm, and (0 - 250) nm samples, respectively.

4.2.2 Condenser NA Optimisation

Photothermal signal detection in this experiment is reliant on the conversion of a thermal lens, induced by the absorption of the modulated Stokes beam, to a modulation of the detected pump beam, collected in this case by the condenser. This thermal lens causes a divergence in the pump beam which allows for the NA of the condenser, and hence amount of transmitted signal detected, to be optimised for
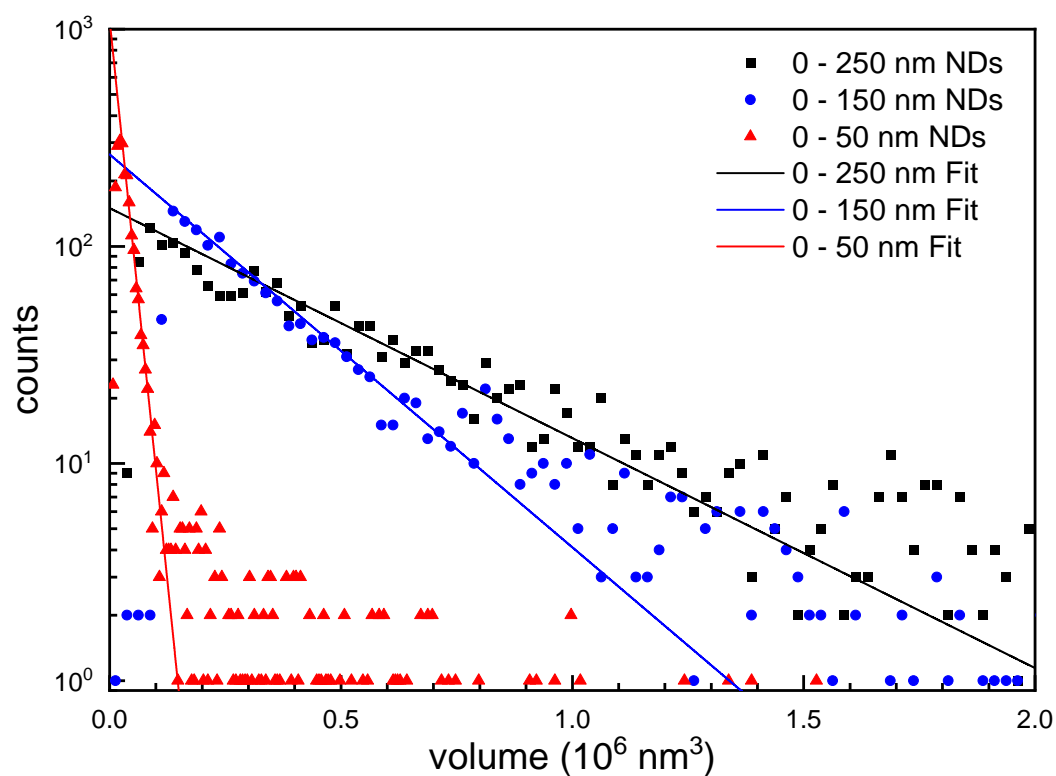
Figure 4.1: Size histograms measured with qDIC on nanodiamonds in silicon oil. Particles with nominal size ranges (0 - 250) nm and (0 - 150) nm were measured using the 0.75 NA objective, while those with (0 - 50) nm sizes were imaged with the 1.27 NA objective. The SE pair was used for the analysis. Solid lines are the exponential fits.

maximum signal to noise. It was expected that at very small NA the majority of the transmitted signal would be blocked, while at very high NA all signal is detected, and thus minimising the effect of the divergence of the transmitted beam. It was therefore expected that, at the NA for which half the transmitted beam is collected, the optimum signal to noise would be observed.

Measurements were carried out on a (0 - 250) nm nanodiamond sample, mounted in silicon oil, with the same region being imaged using the 1.45 NA objective at decreasing values for the condenser NA between 0.45 NA and 1.34 NA. Figure 4.2 shows the dependence of the condenser NA on both the peak relative modulation, as discussed in Section 2.4.2, and signal to noise ratio (SNR) for a single particle. The SNR in this case was estimated using the photothermal signal for a given particle (S_{LI}), the photothermal background signal (S_{BG}), and the photon shot noise of the transmitted pump beam (from the DC signal) using

$$\text{SNR} \propto \frac{S_{LI}(\text{NA}) - S_{BG}(\text{NA})}{\sqrt{DC}}. \tag{4.1}$$

Both the peak relative modulation and the SNR are shown to increase as the condenser NA is decreased, with peak values seen at 0.6 NA. The same pattern was seen for all particles in the region analysed, with the signal either decreasing or saturating at this point, as such it was determined that 0.6 NA was optimal, and was therefore used for all measurements going forward.

4.2.3 Correlative qDIC and Photothermal Measurements of Nanodiamonds

In order to quantify the sp2/sp3 ratio of single NDs, it was first necessary to find their respective volumes, and subsequently the number of sp2 atoms present in each. Given that the sp3 in the ND structure should be dominant, qDIC could be used to determine the volume of the diamonds, as has been shown in Section 4.2.1, with the refractive index used for the analysis being that of bulk diamond (n = 2.42). In order then to find the number of sp2 atoms present in the diamonds, photothermal measurements could be used due to the sp3 structure being transparent at the wavelengths used here. Hence the photothermal signal comes only from the absorption of the Stokes beam due to sp2 bonded atoms causing modulation of the pump beam.

Figure 4.3a and b show the resulting $\delta(\mathbf{r})$ and $\phi(\mathbf{r})$ qDIC images for the untreated 250 nm ND sample. The usual shadow cast pattern can be seen in the $\delta(\mathbf{r})$ image, with the expected stripe pattern seen in the $\phi(\mathbf{r})$ image due to the κ term used in the Wiener filtering process. A correlative photothermal image can be seen in Figure 4.3c, with the amplitude and phase encoded as the value, between 0 to 5 mV, and hue, between $-\pi$ to π radians, in the HSV (standing for Hue, Saturation, and Value) image, respectively. The insets in Figure 4.3b and c show the same particles, indicating that the nanodiamonds in these positions contain at least some sp2 bonded carbon atoms in their structure.

In order to gain a qualitative understanding of the sp2 content of the NDs, the volume for each particle in the image was found as described in Section 2.2.2. The surface area for each could then be calculated simply using $A = 6V^{2/3}$, as this gives the total area of an unwrapped 6-faceted cube. The peak relative modulation found for the corresponding particles was then plotted against this surface area for each sample, the results of which can be seen in Figure 4.4. This showed that in general the treatment described in Section 2.1.4 reduced the amount of sp2 in the
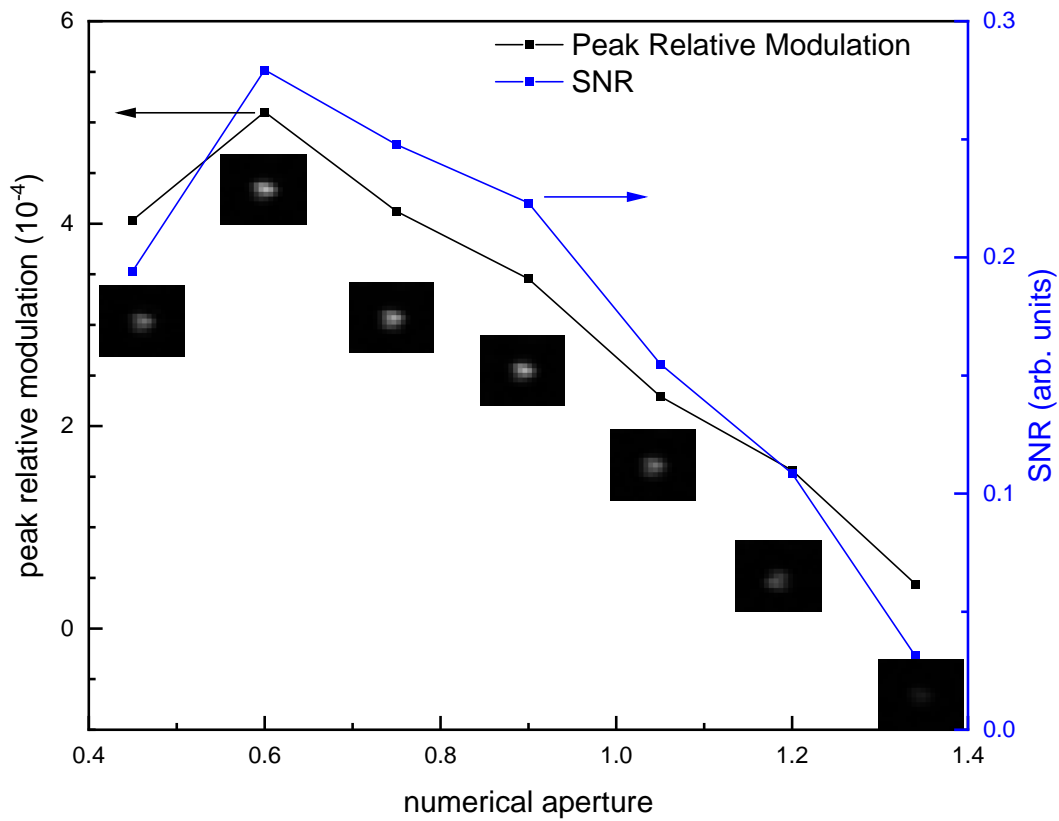
Figure 4.2: Plot showing the dependence of the condenser NA on the peak relative modulation (Black, left scale) and signal to noise ratio (Blue, right scale). Photothermal images of $(2.26 \times 1.89)\,\mu\mathrm{m}^2$ are shown around the particle analysed ($m = 0\,\mathrm{V}$ to $M = 0.015\,\mathrm{V}$).
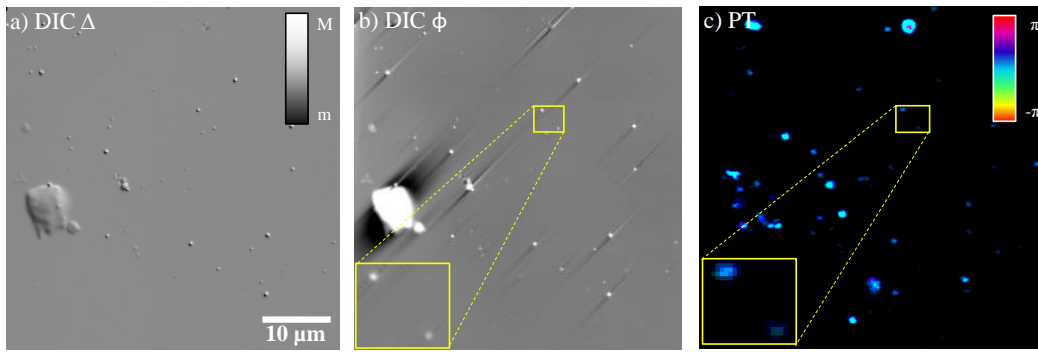
Figure 4.3: qDIC and photothermal images of the untreated 250nm NDs. (a) Differential phase $\delta(\vec{r})$ on a grey scale as shown, from m = -0.1 to M = 0.1. The shadow cast impression of DIC is evident, with the shear $s = 0.238(1,1) = \sqrt{2}$ μm in the (x, y) coordinates with x horizontal and y vertical. (b) Corresponding phase $\phi(\vec{r})$ image (m = -0.1 rad to M = 0.1 rad), with an inset showing a region of (3.94×3.55) μm^2 around selected particles indicated by the yellow square (m = -0.18 rad to M = 0.18 rad) using Wiener filtering with $\kappa = 200$. (c) Photothermal image of the same region using an of a HSV colour map with the value given by the amplitude (0 to 5 mV) and a hue given by the phase $(-\pi$ to π radians), and maximum saturation. The inset shows a zoom of a selected region of (4.53×3.96) μm^2 around the same particles as in b, using a value mapped from 0 to 0.4 mV amplitude

nanodiamonds. This is further evidenced by the fit lines applied to the plot, with that of the untreated NDs having a gradient value of 4×10^{-10} nm^{-2} compared to the fit for treated NDs which had a gradient of 1×10^{-10} nm^{-2}. From these it can also be seen that the sp2 measured is predominantly on the surface as the peak relative modulation increases roughly proportionally with the surface area of the diamonds for both the treated and untreated samples. It is important to note that the treated NDs used here had been stored at room temperature for a period of 4 years, however, it was not expected that these would have undergone graphitisation in that time.

4.2.4 Photothermal Sensitivity

While the phase area sensitivity of the qDIC technique has been determined previously to be around $17\,\text{nm}^2$ (corresponding to a nanodiamond with a size of around $12\,\text{nm}$) for the conditions used here, the sensitivity of the overall method is also dependant on that of the photothermal technique. This was obtained by analysing a number of positions for each region imaged with no ND present in the corresponding DIC images. Resulting histograms for the in-phase and in-quadrature amplitudes were plotted and Gaussian fits applied to both. These fits had standard deviations of $\sigma = 2.93 \times 10^{-5}\,\text{V}$ and $2.89 \times 10^{-5}\,\text{V}$ for the in-phase and in-quadrature components, respectively. Using Equations 2.19 and 2.22, this equates to an amplitude of $\sigma_{amp} = 4.11 \times 10^{-5}\,\text{V}$ and a peak relative modulation of $M_{rel_\sigma} = 3.05 \times 10^{-7}$. In order to ensure the particles are visible above the background noise, a sensitivity limit of two standard deviations above the noise was assumed, meaning a sensitivity limit of $M_{rel} = 6.10 \times 10^{-7}$. This sensitivity limit is shown in Figure 4.4 as a grey coloured region, with any particles observed within this region in Figure 4.4 being excluded from the fits applied.

Given the linear fit applied to both the untreated and treated samples minimum observable ND sizes of 16 nm and 32 nm were derived, respectively. This result was as expected, with the higher sp2 content in the untreated NDs giving a larger photothermal signal as compared to the treated NDs, in turn allowing for smaller NDs to be visible when they are untreated as opposed to when they are treated. Given the higher sensitivity for the qDIC measurements, it can be seen here that the photothermal measurements are the limiting factor as to how small a particle can be observed when using these combined techniques to obtain the sp2/sp3 ratios of single NDs. Given however the low laser powers, measured at the beam entrance, of 2.5 mW and 5 mW for the Stokes and pump beams used, respectively, it is possible for a greater sensitivity in the photothermal measurements to be obtained simply by using higher laser powers. However, in so doing, further issues could be encountered, such as causing the particles to be moved around the sample leaving bright streaks in the images, and possibly causing graphitisation of the NDs due to heating of the samples when the Stokes beam is absorbed by any sp2 present. Figure 4.5 highlights the issue of particles moving around the surface, showing photothermal images of a PGF sample imaged at increasing Stokes powers, from 2 mW to 18 mW, in an attempt to find the best power to use for measurements. While at 2 mW there is no movement of any particles, it is clear that at increasing powers the number of particles moving around the sample increases. This would cause an issue when analysing the images, as such use of lower powers was justified.

4.3 Phase Measurements

The phase of S_{LI} for the various NDs and PGFs are shown in Figures 4.6 and 4.7, respectively. A variation of the phase around 0.5π rad, within $\pm 0.3\pi$ rad, was observed as was expected from literature. This is because the photothermal signal requires some time to build and decay, such that a $\pi/2$ phase shift in the signal would be expected when compared to the stimulated Raman loss signal of the oil used to calibrate the measurements [167].

4.4 Correlative Extinction and Photothermal Measurements of Graphene

Unlike diamond, which strongly scatters visible light, graphene is a strong absorber not only in the visible range but also deep into the infrared. As such it is possible to obtain the absorption cross section of individual graphene flakes using extinction microscopy. This absorption cross section is related to the surface area of the graphene while also being directly proportional to the photothermal signal allowing the number of sp2 carbon atoms in each particle to be calculated. Extinction and photothermal images obtained of the same region for the pure sp2, PGF sample, can be seen in Figure 4.8a and b, respectively. Similarly with Figure 4.3, the phase has been encoded as hue while the photothermal amplitude is given by the HSV value in the same way as previously. To determine which particles seen in the extinction image were single sheets of graphene, line profiles were taken along the particles to show their peak extinction image contrast. For PGFs a peak extinction contrast when unpolarised of around 1.5% was expected (see Equation 4.2 and related discussion below), with this value expected to remain the same, and decrease
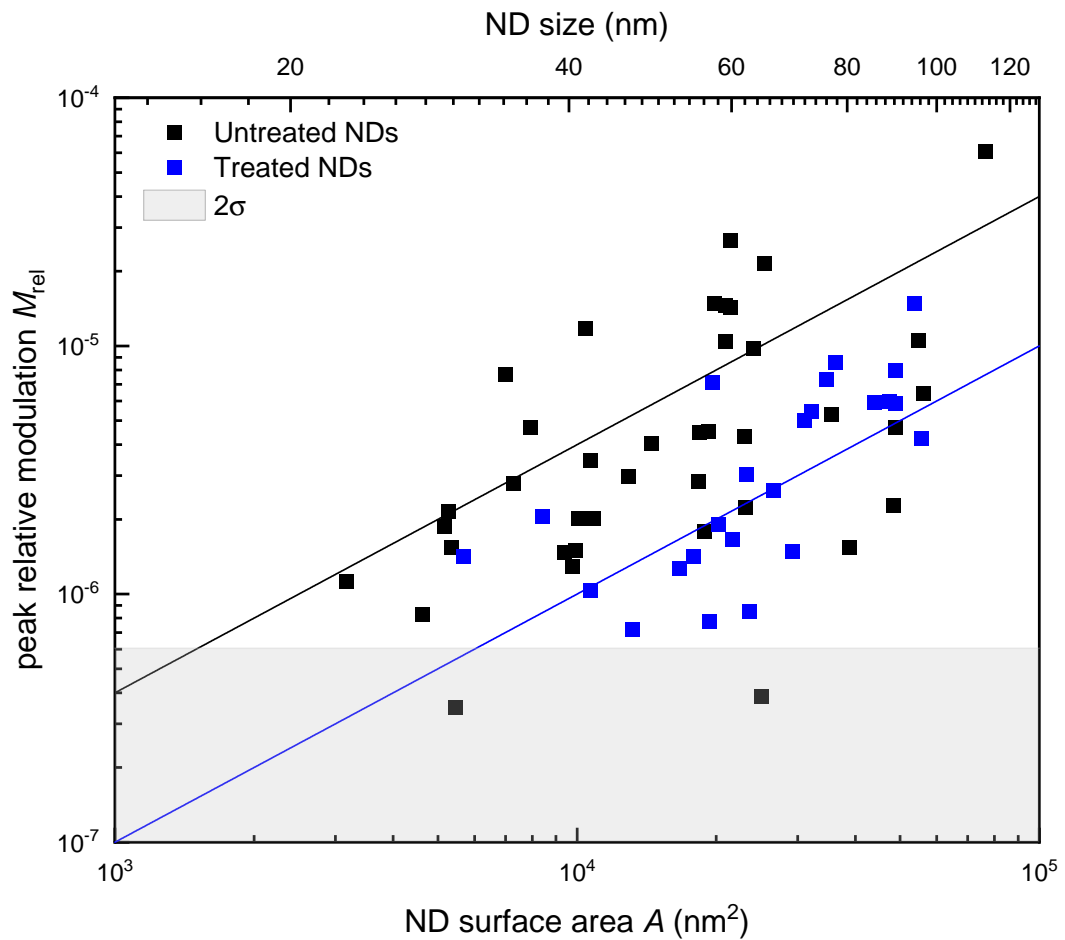
Figure 4.4: Correlation between the ND surface area A calculated from the ND volume measured in qDIC, assuming cubic shape, and the peak relative modulation M_{rel} measured in photothermal and attributed to sp2 bonds. Data for both the untreated (black symbols) and treated (blue symbols) ND samples are shown. Lines are fits proportional to A. The grey shaded region shows the noise (2 standard deviations) of M_{rel}.
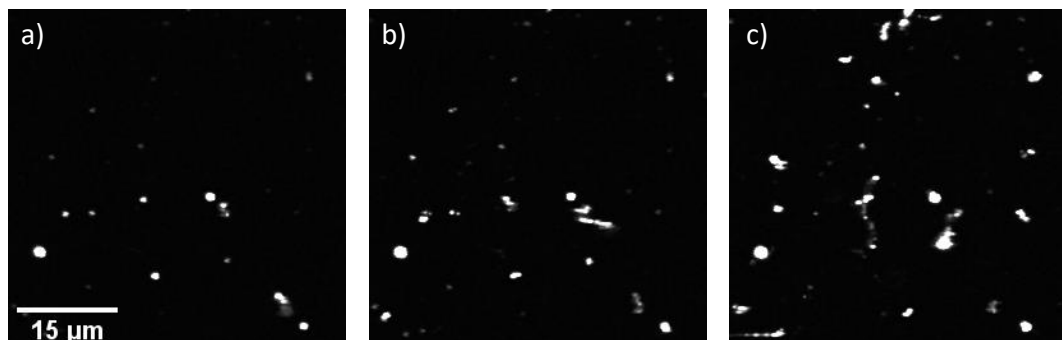
Figure 4.5: Photothermal images of the same region of the PGF sample at Stokes powers of (a, m = 0 V to M = 0.0036 V) 2 mW, (b, m = 0 V to M = 0.0036 V) 9 mW, and (c, m = 0 V to M = 0.0036 V) 18 mW. White streaks along the images show particles which have moved around the sample during measurements.
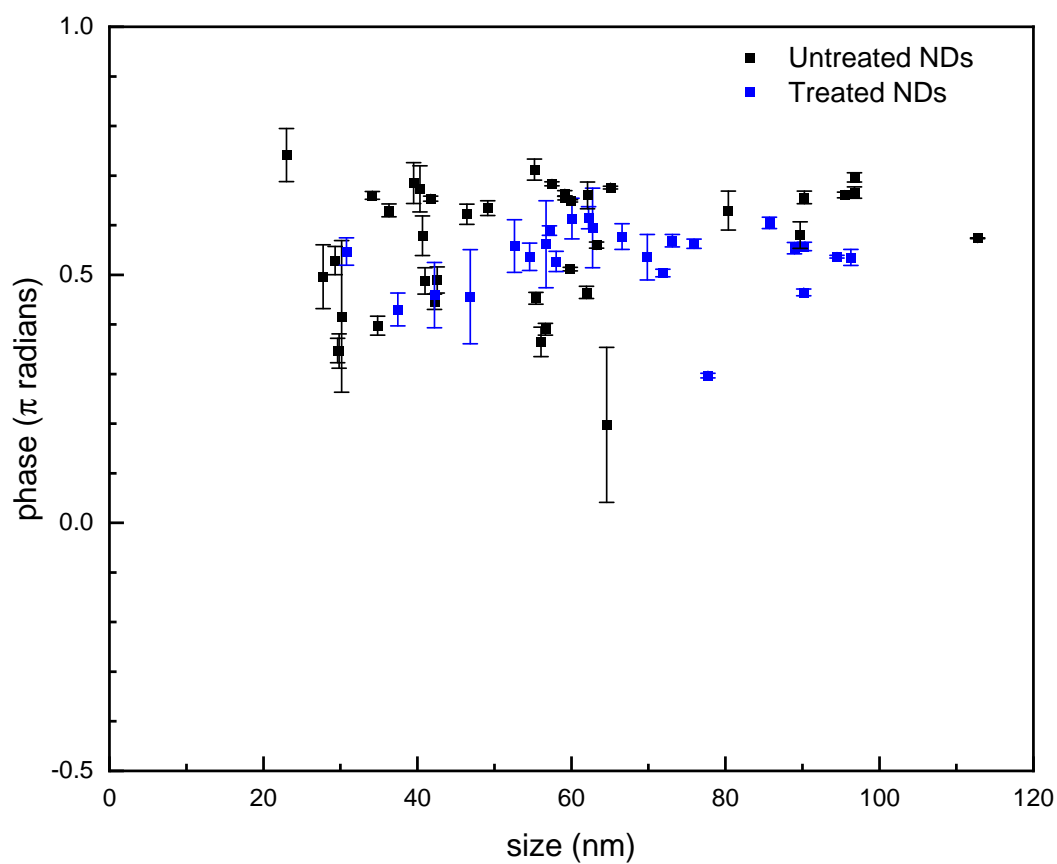
Figure 4.6: Plot showing the calculated phase for all treated (Blue) and untreated (Black) NDs measured against the size of each ND.
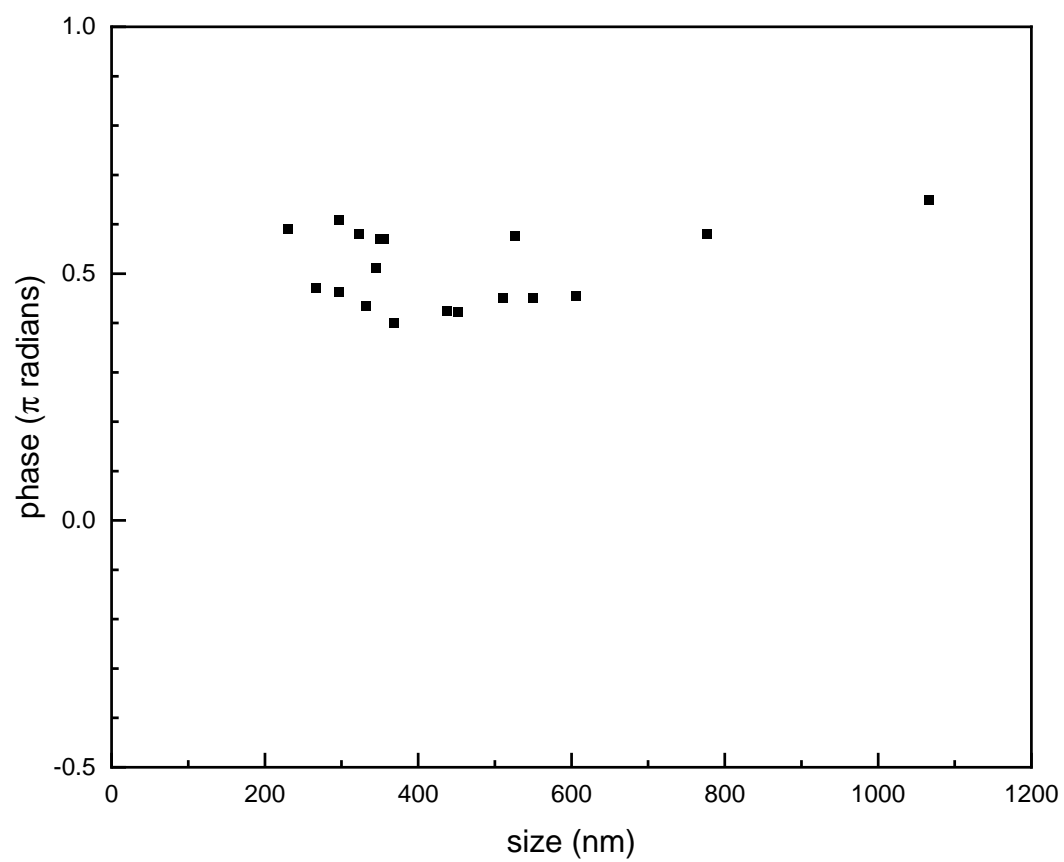
Figure 4.7: Plot showing the calculated phase for all PGFs measured against the size of each.
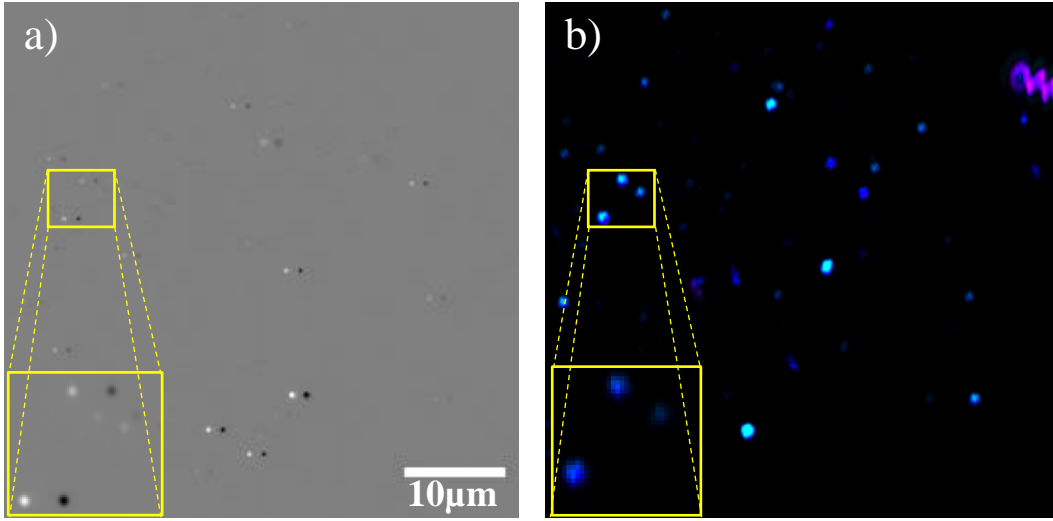
Figure 4.8: (a) Extinction image carried out for a PGF sample (from $m = -0.1$ to $M = 0.1$), with an inset showing a (4.97×4.61) μm^2 region around the particles shown in the yellow square ($m = -0.08$ to $M = 0.08$). (b) Photothermal image showing the same region as (a) ($m = 0$ mV to $M = 10$ mV) with the phase encoded as an RGB colour map as in Figure 4.3, and an inset showing the same particles as in the inset for (a) (5.47×5.28) μm^2 ($m = 0$ mV to $M = 50$ mV).

for measurements using the azimuthal polariser and radial polariser (as discussed in Section 2.3.1), respectively. For the particles analysed values for the peak extinction, when unpolarised, were found to be between 0.8 and 1.2%. For the radial measurements, some decrease in the peak extinction was seen, however, not as much as would be expected from a single graphene sheet. Possibly this discrepancy was due to the 'long shadow' effect, which is the longer shadow cast by the particle when illuminated by oblique light [117], though it could also be that the particles are not single layer as expected but are several layers.

A home built software, Extinction Suite (as described in [128]), was then used to determine the extinction cross section, σ_{ext}, of the particles using the method described in Section 2.3.2. The area of the particles, A_{gr}, could then be calculated from the extinction cross section and the absorption of the graphene, η_{gr}, such that

$$A_{gr} = \frac{\sigma_{ext}}{\eta_{gr}}. \tag{4.2}$$

When in a vacuum, the absorption of graphene would be expected to be around 2.3% as determined by the equation, $\eta_{gr}(\text{vac}) = \pi\alpha$, where α is the fine structure constant [**?**]. However, due to the refractive index of the mounting medium used here (n = 1.518), the expected absorption of the graphene is reduced to the 1.5% mentioned previously (as $\eta_{gr} = \eta_{gr}(\text{vac})/n$). From A_{gr} it is then possible to calculate the number of sp2 atoms within each graphene sheet. Given the 2 atoms per unit cell of graphene, and the unit cell area of graphene being $A_u = 0.052$ nm^2, the number of sp2 atoms in a particle, N_{sp2}, can be found simply by

$$N_{sp2} = \frac{2A_{gr}}{A_u}. \tag{4.3}$$

The peak relative modulation of the particles was found in the same way as for
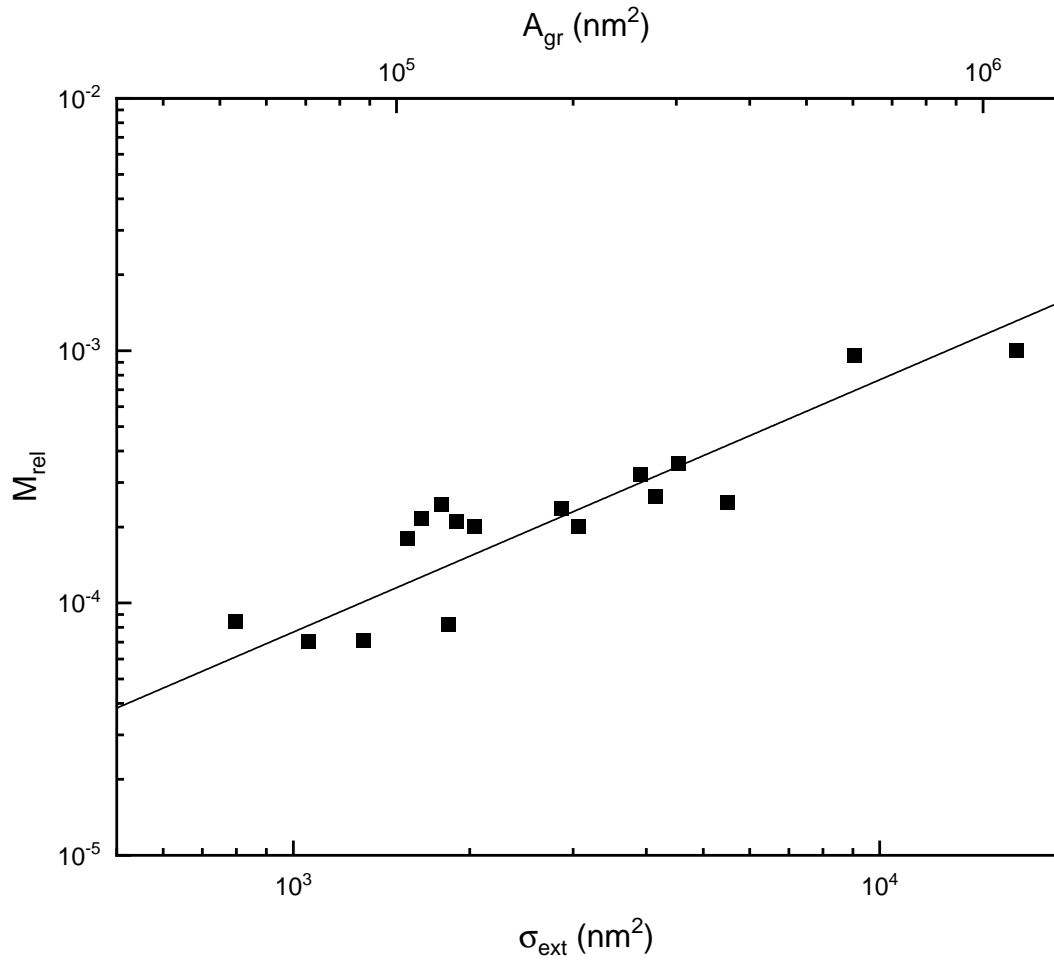
Figure 4.9: Correlation between peak relative modulation, M_{rel}, and the extinction cross-section, σ_{ext}, measured on graphene nanoflakes. The line shows a scaling $M_{rel} = \beta\sigma_{ext}$. The corresponding graphene area $A_{gr} = \sigma_{ext}/\eta_{gr}$ is shown as top axis.

the nanodiamonds in Section 4.2.3. The peak relative modulation was then plotted against both the extinction cross section and the area, as can be seen in Figure 4.9. A straight line fit was then applied to the data, from which it can be seen that M_{rel} increases proportionally to the PGF area, as was expected. The results shown here give a scaling factor of $\beta = 1.15 \times 10^{-9}$ nm^{-2} between M_{rel} and A_{gr}, with variations in this value being due to differences in shape between individual flakes, causing a change in shape of the photothermal lensing.

4.5 sp2/sp3 Ratios

With the dependence of the peak relative modulation due to a known size of pure sp2 sample obtained from photothermal measurements of graphene flakes, as well as the volume of each ND obtained using qDIC, it was possible to determine a quantitative sp2/sp3 ratio for individual NDs. The number of sp3 atoms, N_{sp3}, in each ND was calculated from their respective volume, V_{ND} using

$$N_{sp3} = \frac{8V_{\mathrm{ND}}}{V_u}, \tag{4.4}$$
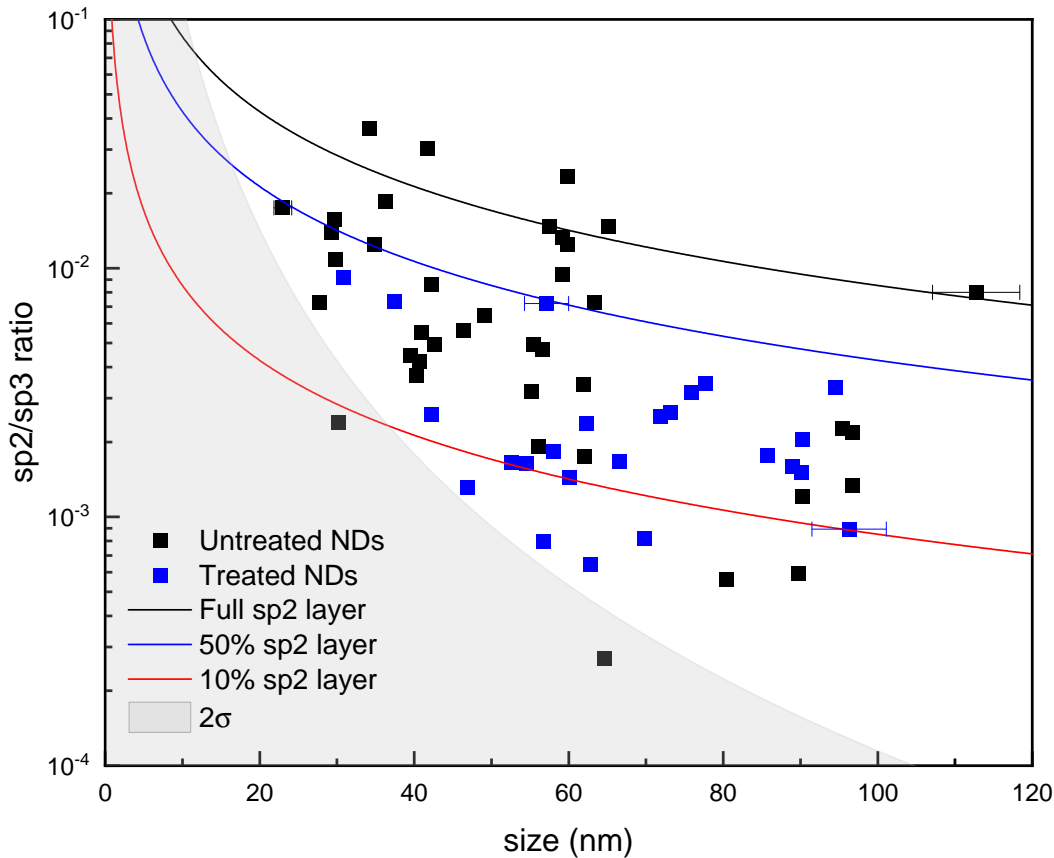
Figure 4.10: Ratio, R, of the number of sp2 to sp3 bonded atoms for individual untreated (black squares) and treated (blue squares) NDs against their sizes measured using qDIC. The error in the size was 5%, as determined from Section 3.4. Lines showing the ratios corresponding to different graphene monolayer coverages are shown - 100% (black), 50% (blue), and 10% (red). The grey shaded region indicates ratio at the photothermal noise limit 2σ.

where the volume of the diamond unit cell structure, V_u, is known to be 0.045 nm^3 and contains 8 atoms. Using then the scaling factor, β, obtained in Section 4.4, the number of sp2 atoms present in each ND could be calculated from the photothermal signal of each seen in Figure 4.4. Knowing this, the sp2/sp3 ratio, R could be calculated simply using $R = n_{sp2}/n_{sp3}$. Figure 4.10 shows this ratio plotted against the size of each ND. In general the results discussed earlier still hold, with the untreated diamonds containing a higher ratio of sp2 atoms when compared to that of the treated diamonds.

Assuming the argument put forward previously, that the sp2 atoms are primarily located on the surface of the diamonds, the thickness, and hence percentage coverage, of the sp2 layer could be calculated. Due to the small layer thickness, t, compared to overall size, S, the equation $t = R \cdot S/6$ could be used to obtain the thickness of the sp2 layer around the six sides of the cubic shape diamond. From Figure 4.10, it can be seen that the all the treated NDs analysed have between 5 - 30% coverage of surface sp2 while the untreated NDs can have as much as 150% surface coverage of sp2, meaning there is a full layer and a half thick sp2 coverage surrounding the surface of the NDs. However, the majority of untreated NDs have far less, with around 50% sp2 coverage.

4.6　Conclusion

In conclusion, a method by which the sp2/sp3 ratios of single nanodiamonds can be calculated has been developed using a combination of qDIC and photothermal microscopy. Nanodiamonds fabricated by HPHT growth and milled to size were investigated, with some having been previously treated to remove sp2 while others were left untreated. The results showed that the untreated diamonds contained up to 150% surface coverage of sp2, while the treatment method has significantly reduced this sp2 content to typically below 30% surface coverage. Using this method, it is possible to detect around 2×10^4 sp2 atoms, calculated from the peak relative modulation found for the sensitivity limit, which corresponds to a full monolayer coverage of a 10 nm diamond.

With the rise in uses of nanodiamonds in industry, medicine, in quantum applications, and many other fields, being able to determine the content of individual diamonds becomes increasingly important. Of particular note is the stability of NV centres, used in quantum applications, which can show spectral instability under optical excitation in the presence of sp2. This technique offers an accurate method to determine the sp2 content of individual nanodiamonds, such that the nanodiamonds used for sensitive applications could be screened for suitability prior to use.

Chapter 5

Extinction of Single Wall Carbon Nanotubes

5.1 Introduction

CNTs, as discussed in Section 1.2, are an allotrope of carbon with a pure sp2 structure, consisting of a single layer of carbon atoms electronically bonded and rolled around an axis forming a tube [79]. Due to this rolling, one of the properties of CNTs is their chiral index, given in terms of their primitive lattice parameters n and m [80]. This chirality determines many of the other properties of the CNTs including whether they are semiconductors, metallic, as well as their diameters [82, 83]. As with NDs, CNTs have a wide variety of uses in medicine and biotechnology [84, 85, 86] due to their tensile strength and electrical properties. As such, accurate determination of the chirality of individual nanotubes has become important to characterise, with methods such as AFM and Raman spectroscopy currently being used [89, 91]. This chapter discusses the experiments conducted to use the optical extinction microscopy method discussed in Chapter 4 and Section 2.3.1 to determine the chirality of individual SWCNTs.

5.2 Preparation of CNT Samples

Prior to any extinction measurements being carried out on the CNTs discussed in Section 2.1.5, preparation needed to be carried out to ensure predominantly individual nanotubes would be deposited on the coverslip. For this purpose, a SWCNT water dispersant from US research nanomaterials (US4498) was used and a titration series of concentrations tested to find the optimum for individual CNT deposition. A dispersion was prepared with a surfactant concentration of $6\,\mu l/ml$ and a CNT concentration of 0.2 mg/ml. $20\,ml$ of this initial dispersion was sonicated using a Fisherbrand probe sonicator (Fisherbrand 12337338) at 30% power for 10 minutes and left stored in a fridge overnight for the large aggregations on CNTs to settle. Two methods to further dilute the dispersion were tested, using only DI water and using a less concentrated surfactant dispersion. The less concentrated dispersion was expected to maintain a sufficient level of surfactant such that the concentration remained above that of the surfactant equilibrium in solution for full coverage of the CNTs, to keep CNTs covered. These titration series were prepared by pipetting decreasing quantities of the supernatant from the initial dispersion into 1 ml of either the DI water or a $0.06\,\mu l/ml$ surfactant dispersion. Titrations from 1:10

down to 1:1000 concentrations of the initial CNT dispersion were prepared for each case. Coverslips were prepared for each titre, with the dispersions being wet cast onto the coverslip surface and left for an hour prior to be rinsed off with DI water. As discussed in Section 2.1.5, GNPs were then spin coated onto the coverslip prior to them being mounted on slides and sealed. To determine which titration was best to be used for full extinction measurements, live extinction microscopy was used. The setup for this technique was the same as discussed in Section 2.3.1, however, a reference background was obtained by averaging a stack of 6400 images of the sample with the stage moved in a scanning pattern 10 μm in x and 10 μm in y. In so doing, any particles present in the region imaged are averaged out to give an image with the background intensity. Using the camera software, this reference image was then subtracted from the live display allowing for extinction images of the sample to be viewed in real time. Figure 5.1 shows the resulting live extinction images (averaged in real time over of 256 frames) of the titration series, using an excitation wavelength of 550 ± 20 nm. These show that for a CNT concentration above 0.02 mg/ml samples are too dense for both titration series (as seen in Figures 5.1a, and d), however, when the surfactant solution was used to disperse to a CNT concentration of 2 μg/ml, the distribution of individual CNTs on the sample was good as can be seen in Figure 5.1e. Lower concentrations of CNTs are shown to be too sparse on the surface, as is true for the 2 μg/ml sample diluted using only DI water (see Figures 5.1b, c, and f). The grid pattern seen in the live extinction images in all panels of Figure 5.1 was determined to be an artefact of the camera software, while the streak artefacts are caused by the reference image for each being obtained at a different FOV on the samples. This means the background for the reference was slightly different to that of the imaged FOV, and when subtracted gives rise to streaks in the resulting images.

5.3 Extinction Measurements of CNTs

5.3.1 Setup and Analysis

The same setup was used for these experiments as described in 2.3.1. Measurements for wavelengths ranging from 400 nm to 800 nm were used at 50 nm increments. Colour filters (Thorlabs FKB-VIS-40) were used to achieve this providing a peak at the desired wavelength and a FWHM of 40 nm. Illumination was provided by the 100 W tungsten-halogen lamp, for wavelengths between 500 nm and 800 nm, while an LED light source (Thorlabs LED4D106) was used for excitation wavelengths of 400 nm and 450 nm as the tungsten lamp emission was too weak in this range. For each excitation wavelength, a linear polariser was used to polarise the light between 0 and 150 degrees, at increments of 30 degrees. The total number of brightfield acquisitions for each polariser angle were 21600 for excitation wavelength of 400 nm to 450 nm, while between 500 nm and 800 nm the total number of brightfield acquisitions per polariser angle was 51200. This provided images with a minimum noise of around 1.6 nm^2, estimated using equation 2.16, for the 550 nm excitation measurements.

Analysis of resulting extinction images was carried out using version 1.3 of an in house software developed by Dr. Francesco Masia called NanotubeFit. In a similar way to how the extinction cross-section is calculated using Extinction Suite, this software found the extinction for positions along the length of each tube. The initial position to be fit was selected by the user at any point along a given nanotube, with
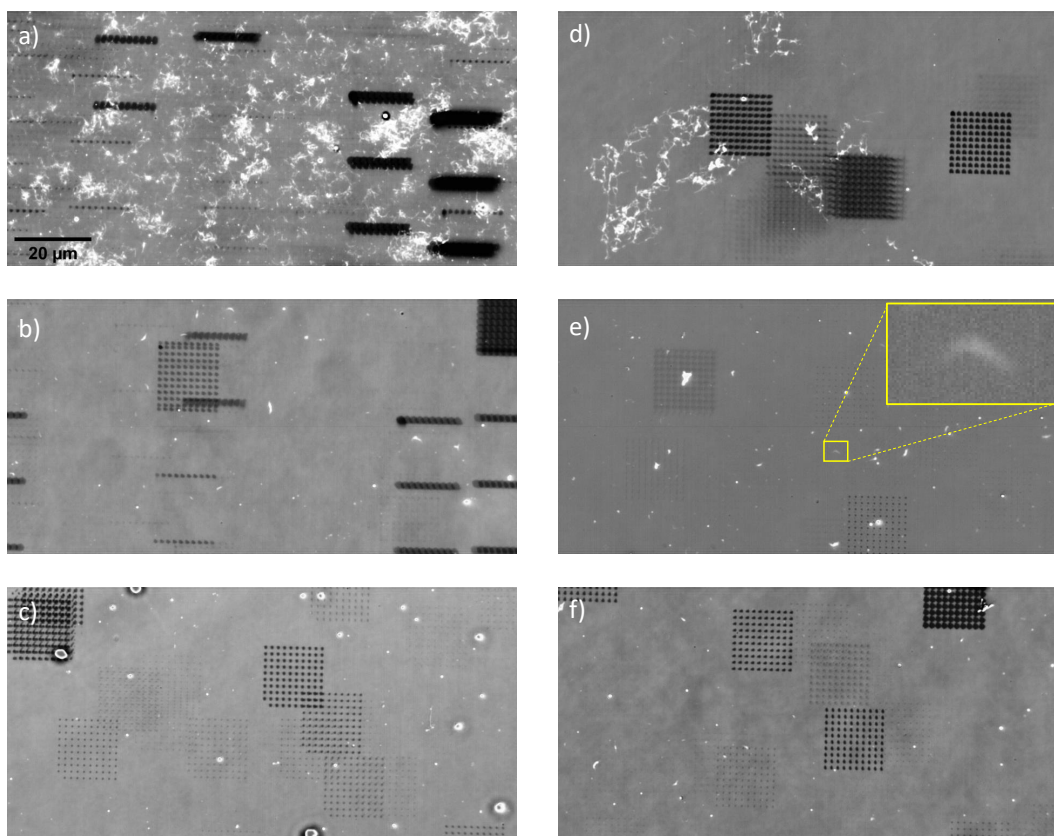
Figure 5.1: Extinction images showing the titration series carried out to determine the optimum concentration of dispersant for CNTs. Titration series using DI water (a $[0.02\,\text{mg/ml}$, $m = 712$ to $M = 64802]$, b $[2\,\mu\text{g/ml}$, $m = 840$ to $M = 64654]$, and c $[0.2\,\mu\text{g/ml mg/ml}$, $m = 1018$ to $M = 64763]$) or surfactant dispersion (d $[0.02\,\text{mg/ml}$, $m = 814$ to $M = 64690]$, e $[2\,\mu\text{g/ml}$, $m = 8876$ to $M = 64602]$, and f $[0.2\,\mu\text{g/ml}$, $m = 815$ to $M = 64837]$) for the same purpose. The inset in e) ($m = 22984$ to $M = 41941$) shows a region around an individual SWCNT of $(4.72 \times 2.76)\,\mu\text{m}^2$. The grid pattern seen was deemed to be due to an artefact of the camera software, and was not visible during live imaging, while the streak artefacts were due to slight variations in the background intensity between the reference and imaged FOV.

the PSF used for the fit defined by the user as either a Gaussian, Lorentz, Airy, or sech^2 function and the 'ROI radius' defined by the user being the size of the radius within which the PSF was analysed. After analysing the initial position to determine the extinction cross section, the algorithm then selected a second position a given distance, defined by the user by a parameter called the 'step size' as a factor of the PSF size, away from the initial position which was then analysed to find the extinction cross section. This was then repeated along the length of the nanotube until reaching the end of the tube. The algorithm determined the edge of the nanotube when the analysed signal fell below the root mean square of the noise multiplied by a user defined parameter called the 'threshold edge', at which point the algorithm would reverse direction and refit the PSFs along the length of the nanotube. The number of times the algorithm reversed directions to refit the nanotube was determined by the user defined parameter called the 'max of iterations'. To allow for a curvature in the nanotube being analysed, another parameter could be adjusted by the user called the 'minimum radius of curvature' which allowed the algorithm to change directions when an edge is reached to continue analysis along the curved nanotube. It should be noted that nanotubes curved on a smaller scale than the PSF, and those lying perpendicular to the coverslip could not be accurately analysed using this software. By optimising these user defined parameters, the residual signal of the fit could be minimised, hence giving higher accuracy for the obtained extinction cross section along the nanotube.

5.3.2 Initial Amplitude Fits of SWCNTs

Figure 5.2 shows an extinction image of a single nanotube, and the resulting residual image obtained from a fit performed using NanotubeFit, showing how the residual was minimised given ROI used for the fitting procedure. To ensure the smoothest fit, an ROI was chosen such that it encompassed the minimum of the second airy ring for each PSF. In this case, this was $4.39\times$ the half width at half maximum of the first channel (being the $\lambda = 400\,\text{nm}$ and $0°$ polariser angle). For each tube a different radius of curvature was found to be optimal due to their different shapes, however for the tube shown in Figure 5.2 this was found to be best at $10\times$ the half width at half maximum of channel 1. Figure 5.3 shows the extinction amplitude measured for each PSF along the length of the nanotube presented in Figure 5.2 from which the extinction cross section, and hence chiral index could be calculated in future measurements.

This shows the viability of identifying individual SWCNTs using this technique, while also showing an example measurement of the PSF amplitudes along an individual SWCNT from which the extinction cross section and hence chiral index could be calculated in future measurements. However, further investigation into the ideal parameters to be used for higher wavelengths are still required, as well as optimisation of the fitting algorithm required for such chirality characterisation.

5.4 Conclusion

In conclusion, dispersions of individual SWCNTs with a concentration of $2\,\mu\text{g/ml}$ have been prepared using a CNT water dispersant, showing a good distribution on the sample. Optical extinction measurements of individual CNTs were subsequently carried out, and amplitude fits of the extinction along the tube optimised to reduce
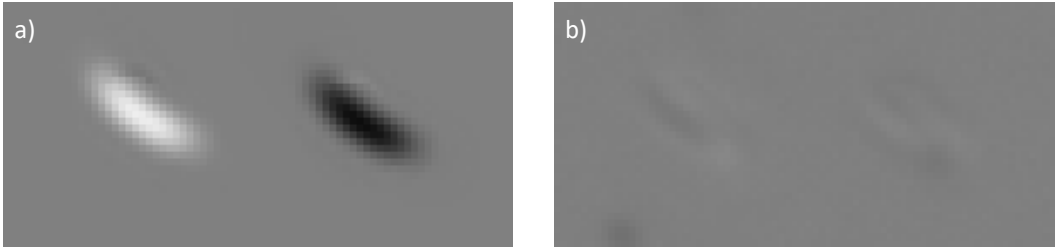
Figure 5.2: Extinction images $(4.88 \times 2.34)\,\mu\text{m}^2)$, obtained using $\lambda_{ex} = 400\,\text{nm}$ and polariser angle of $0°$, showing the amplitude (a, m = - 0.0035 to M = 0.0035) and residual (b, m = -0.02 to M = 0.02) for a CNT using an ROI of $4.39\times$ the HWHM of the PSF for the image.
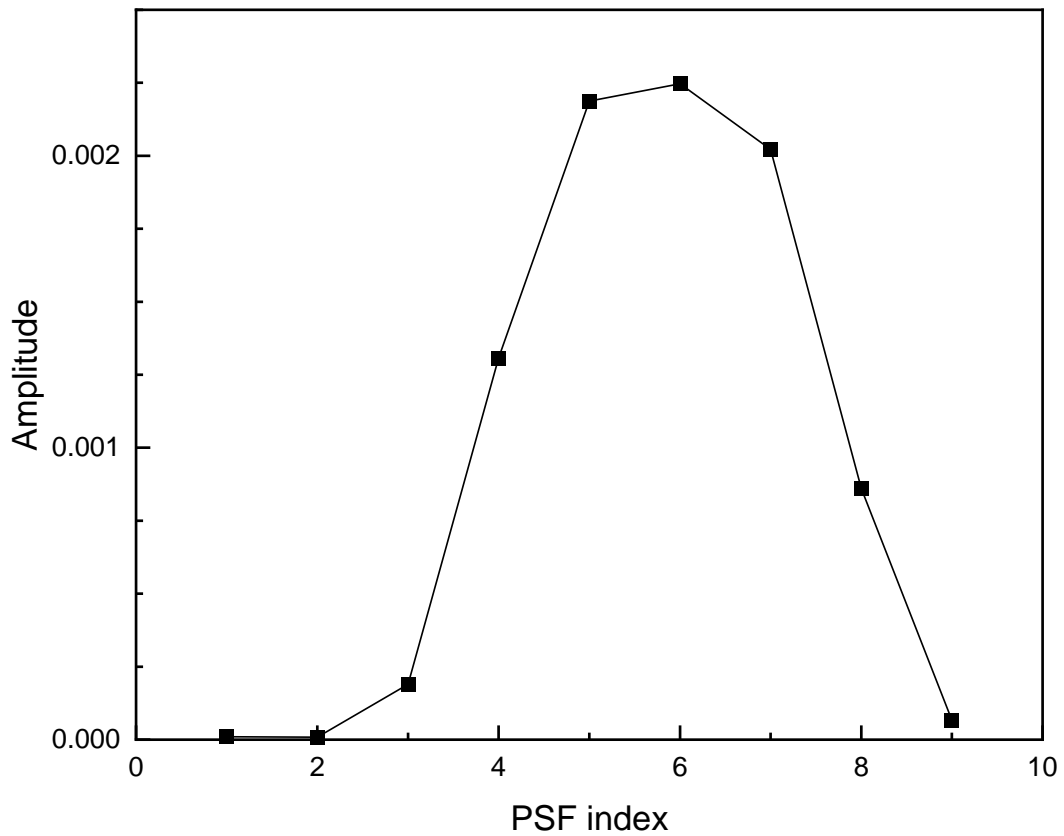
Figure 5.3: Measured extinction amplitude at each PSF along the nanotube shown in Figure 5.2.

the residual signal. This shows a proof of concept for the technique being used to determine SWCNT chiralities. Unfortunately, due to the Coronavirus pandemic, there was not enough time to carry out further measurements and perfect the analysis procedure to accurately determine the chiralities for the SWCNTs. Further experiments could be carried out in future to continue these experiments and perfect the analysis procedure.

Chapter 6

Summary and Conclusion

As has been discussed in Section 1.1.5, the potential medical uses for NDs are wide ranging, and given the other quantum and industrial applications of NDs, characterisation of individual diamonds is becoming ever more important. Among the parameters needed to be characterised is the proportion of sp2 bonded carbon in individual NDs, due to the way in which this can effect their properties. Currently a number of methods to purify NDs of surface sp2 are available, however, the sp2 content of diamonds can only be found qualitatively for ensembles and quantitatively for the surface of bulk diamond, using techniques such as XPS and Raman spectroscopy. To the best of the author's knowledge, there is currently no non-destructive method by which the sp2/sp3 ratios of individual NDs can be ascertained accurately. This thesis aimed to present a method, using a combination of optical microscopy techniques, to quantitatively measure this ratio.

Chapter 3 presents the calibration of a qDIC technique for size measurements of dielectric NPs. For this stage of the calibration PS beads of 100 nm radius, and a CV of 3%, were used. The resulting sizes obtained for the beads showed good agreement with other techniques, within 6 nm radius, including SEM and TEM. Further presented in this chapter was a characterisation of the background and shot noise for this technique. Using fluorescing, 15 nm radius, PS beads it was ascertained that the smallest detectable PS bead as seen by eye would be of 10 nm, though beads reliably detected using the analysis software have a radius of $18\,\mathrm{nm}$ due to the 4σ limit discussed. It should be noted that these measurements were still limited by the background noise, likely due to structures on the glass leftover after the cleaning cleaning procedure. However, if limited only by shot noise, this could practically be reduced to 4 nm with a potential limit of 2 nm radius. Presented in Chapter 4, was an application of this qDIC technique to NDs of varying sizes. Sizes of the individual NDs were successfully obtained, and showed a nearly exponential distribution in their sizes, with a mean of 28 nm found for the sample nominally smaller than 50 nm.

Chapter 4 subsequently presents measurements of both individual NDs and PGFs using photothermal microscopy. From correlative extinction measurements of the graphene flakes, it was possible to obtain a quantitative relationship between the photothermal modulation and the area of graphene present in a particle, with a scaling factor of $\beta = 1.15 \times 10^{-9}\,\mathrm{nm}^{-2}$. Using then the volume of individual nanodiamonds found using qDIC, and the obtained photothermal response for each, the sp2/sp3 ratio could be calculated for individual nanodiamonds and hence the thickness of the surface sp2 layer. It was found that by treating the nanodiamonds

as discussed in Section 2.1.4, the total surface sp2 coverage for the diamonds could be reduced from around 150% to 30%. The sensitivity of the photothermal measurements was found to correspond to 2×10^4 sp2 atoms, which was calculated to correspond to a full layer coverage of a 10 nm diamond. While it would be possible to improve this sensitivity by increasing the Stokes power used to induce the photothermal lens around the particles, this was shown to cause issues particularly with the PGFs which moved around the sample when higher powers were used. A solution could be to fix the graphene flakes and nanodiamonds in place for future measurements.

Finally, Chapter 5 presents the results from the initial investigation into using optical extinction microscopy to determine the chirality of SWCNTs. A method by which individual nanotubes were separated and dispersed in water was discussed, with a nanotube concentration of $2\,\mu$g/ml found to be best. Fits for the CNTs were then presented showing the parameters used to minimise the residual signal for a single nanotube, showing a proof of principle in using optical extinction microscopy for chirality measurements on individual SWCNTs. Due to time limitations brought about with the Coronavirus pandemic, further work was not possible. However, future measurements could be conducted to obtain the chirality of whole nanotubes.

In conclusion, presented in this work is a method by which quantitative measurements of the sp2/sp3 ratios of single nanodiamonds can be obtained using optical microscopy techniques. A combination of qDIC, and photothermal microscopy can be used to accurately measure the number of sp2 atoms present in individual nanodiamonds, while also providing the volume of each nanodiamond. This was facilitated by correlative photothermal and optical extinction microscopy measurements of pristine graphene flakes, from which the photothermal response to a given amount a graphene was calibrated. With the increase in use of nanodiamonds in a number of fields, and given the effect that surface sp2 can have on the properties of the diamonds, this method provides a way to non-destructively ascertain the amount of sp2 present prior to use. Further, a proof of concept is presented using optical extinction microscopy to measure the chirality of individual SWCNTs which could be expanded on by further work.

Publications

The following are the publications which have been produced related to the work presented here.

Articles

Published

1. **S. Hamilton**, D. Regan, L. Payne, W. Langbein, and P. Borri, 'Sizing individual dielectric nanoparticles with quantitative differential interference contrast microscopy', Analyst, vol. 147, no. 8, pp. 1567-1580, Apr. 2022, doi: 10.1039/D1AN02009A.

In Preparation

1. **S. Hamilton**, W. Langbein, and P. Borri, 'Quantitative measurement of graphitic sp2 with sub-monolayer sensitivity on single nanodiamonds using differential interference contrast and photo-thermal microscopy', *In Preparation*, 2023.

Conferences

1. **S. Hamilton**, D. Regan, L. Payne, W. Langbein, and P. Borri, 'Sizing individual dielectric nanoparticles with quantitative differential interference contrast microscopy', *Poster Presentation*, Photon, Nottingham University, UK, 2022.

2. **S. Hamilton**, D. Regan, L. Payne, W. Langbein, and P. Borri, 'Sizing individual dielectric nanoparticles with quantitative differential interference contrast microscopy', *Poster Presentation*, UK Diamond Research Conference, Warwick University, UK, 2022.

3. **S. Hamilton**, D. Regan, L. Payne, W. Langbein, and P. Borri, 'Sizing individual dielectric nanoparticles with quantitative differential interference contrast microscopy', *Oral Presentation*, Focus on Microscopy, Online, 2022.

Bibliography

[1] E. Fitzer and W. Huttner. Structure and strength of carbon/carbon composites. *Journal of Physics D: Applied Physics*, 14(3):347–371, Mar 1981.

[2] sp2 hybridization. https://chem.libretexts.org/@go/page/2579, Oct 2013. Retrieved February 19th 2021.

[3] sp3 hybridization. https://chem.libretexts.org/@go/page/2580, Oct 2013. Retrieved February 19th 2021.

[4] Gerald Ray Miller, Chester F. Poranski, and Henry A. Resing. 13c nmr determination of the in-plane carbon-carbon bond length in graphite intercalation compounds. *The Journal of Chemical Physics*, 80(4):1708–1709, 1984.

[5] D E Nixon and G S Parry. The expansion of the carbon-carbon bond length in potassium graphites. *Journal of Physics C: Solid State Physics*, 2(10):1732–1741, oct 1969.

[6] Robert B More and Jack C Bokros. *Biomaterials: Carbon.* American Cancer Society, 2006.

[7] Thomas Stachel and Jeff W Harris. Formation of diamond in the earth's mantle. *Journal of Physics: Condensed Matter*, 21(36):364206, aug 2009.

[8] Anton Shatskiy, Altyna Bekhtenova, Ivan V. Podborodnikov, Anton V. Arefiev, and Konstantin D. Litasov. Carbonate melt interaction with natural eclogite at 6 gpa and 1100-1200°c: Implications for metasomatic melt composition in subcontinental lithospheric mantle. *Chemical Geology*, 558:119915, 2020.

[9] Yuri N Palyanov, Yuri M Borzdov, Alexander G Sokol, Yuliya V Bataleva, Igor N Kupriyanov, Vadim N Reutsky, Michael Wiedenbeck, and Nikolay V Sobolev. Diamond formation in an electric field under deep earth conditions. *Science advances*, 7(4):eabb4644, 2021.

[10] E. S. de Sa, G. Davies, and William Charles Price. Uniaxial stress studies of the 2.498 ev (h4), 2.417 ev and 2.536 ev vibronic bands in diamond. *Proceedings of the Royal Society of London. A. Mathematical and Physical Sciences*, 357(1689):231–251, 1977.

[11] James E Shigley and Christopher M Breeding. Optical defects in diamond: A quick reference chart. *Gems & Gemology*, 49(2), 2013.

[12] Wayne R. Taylor, Dante Canil, and H. Judith Milledge. Kinetics of ib to iaa nitrogen aggregation in diamond. *Geochimica et Cosmochimica Acta*, 60(23):4725–4733, 1996.

[13] F.H.J. Laidlaw, R. Beanland, D. Fisher, and P.L. Diggle. Point defects and interstitial climb of 90° partial dislocations in brown type iia natural diamond. *Acta Materialia*, 201:494–503, 2020.

[14] J Walker. Optical absorption and luminescence in diamond. *Reports on Progress in Physics*, 42(10):1605–1659, oct 1979.

[15] P T Wedepohl. Electrical and optical properties of type IIb diamonds. *Proceedings of the Physical Society. Section B*, 70(2):177–185, feb 1957.

[16] C. D. Clark, Robert William Ditchburn, H. B. Dyer, and Nevill Francis Mott. The absorption spectra of natural and irradiated diamonds. *Proceedings of the Royal Society of London. Series A. Mathematical and Physical Sciences*, 234(1198):363–381, 1956.

[17] Robert F. Davis. *Diamond Films and Coatings: Development, Properties and Applications (Materials Science and Process Technology Series)*. William Andrew, 1994. ISBN: 9780815513232.

[18] Sally Eaton-Magaña, James E Shigley, and Christopher M Breeding. Observations on hpht-grown synthetic diamonds: A review. *Gems & Gemology*, 53(3), 2017.

[19] L-W Yin, N-W Wang, Z-D Zou, M-S Li, D-S Sun, P-Z Zheng, and Z-Y Yao. Formation and crystal structure of metallic inclusions in a hpht as-grown diamond single crystal. *Applied physics A*, 71:473–476, 2000.

[20] Z.Z. Liang, X. Jia, C.Y. Zang, P.W. Zhu, H.A. Ma, and G.Z. Ren. The influences of n and h on diamond synthesized with ni−mn−co catalyst by hpht. *Diamond and Related Materials*, 14(2):243–247, 2005.

[21] Georgia F. Wood, Carmen E. Zvoriste-Walters, Mark G. Munday, Mark E. Newton, Viacheslav Shkirskiy, Patrick R. Unwin, and Julie V. Macpherson. High pressure high temperature synthesis of highly boron doped diamond microparticles and porous electrodes for electrochemical applications. *Carbon*, 171:845–856, 2021.

[22] Larissa F Dobrzhinetskaya. Microdiamonds−frontier of ultrahigh-pressure metamorphism: A review. *Gondwana Research*, 21(1):207–223, 2012. 10.1016/j.gr.2011.07.014.

[23] J Ullmann, G Schmidt, and W Scharff. Diamond-like amorphous carbon films prepared by rf sputtering in argon. *Thin solid films*, 214(1):35–43, 1992.

[24] Atsuhito Sawabe and Tadao Inuzuka. Growth of diamond thin films by electron assisted chemical vapor deposition. *Applied physics letters*, 46(2):146–147, 1985.

[25] Kazuaki Kurihara, Kenichi Sasaki, Motonobu Kawarada, and Nagaaki Koshino. High rate synthesis of diamond by dc plasma jet chemical vapor deposition. *Applied physics letters*, 52(6):437–438, 1988.

[26] Helena Westberg, Mats Boman, Ann-Sofie Norekrans, and Jan-otto Carlsson. Carbon growth by thermal laser-assisted chemical vapour deposition. *Thin Solid Films*, 215(2):126–133, 1992.

[27] Guan-Ren Lai, EN Farabaugh, A Feldman, and LH Robins. Deposition of diamond films in a closed hot filament cvd system. *Journal of research of the National Institute of Standards and Technology*, 100(1):43, 1995.

[28] T. Mitomo, T. Ohta, E. Kondoh, and K. Ohtsuka. An investigation of product distributions in microwave plasma for diamond growth. *Journal of Applied Physics*, 70(8):4532–4539, 1991.

[29] M Werner and R Locher. Growth and application of undoped and doped diamond films. *Reports on Progress in Physics*, 61(12):1665–1710, dec 1998. 10.1088/0034-4885/61/12/002.

[30] Pria Gautama, Hiromichi Toyota, Yukiharu Iwamoto, Xia Zhu, Shinfuku Nomura, and Shinobu Mukasa. Synthesizing diamond film on cu, fe and si substrate by in-liquid microwave plasma cvd. *Precision Engineering*, 49:412–420, 2017.

[31] Roland Haubner. Low-pressure diamond: From the unbelievable to technical products. *Chemtexts*, 7(2):10, 2021.

[32] David Medina-Cruz, Bahram Saleh, Ada Vernet-Crua, Alessandro Ajo, Amit K. Roy, and Thomas J. Webster. Chapter 22 - drug-delivery nanocarriers for skin wound-healing applications. In Debasis Bagchi, Amitava Das, and Sashwati Roy, editors, *Wound Healing, Tissue Repair, and Regeneration in Diabetes*, pages 439–488. Academic Press, 2020.

[33] Vadym N Mochalin, Olga Shenderova, Dean Ho, and Yury Gogotsi. The properties and applications of nanodiamonds. *Nature nanotechnology*, 7(1):11–23, 2012.

[34] K. Iakoubovskii, M.V. Baidakova, B.H. Wouters, A. Stesmans, G.J. Adriaenssens, A.Ya. Vul', and P.J. Grobet. Structure and defects of detonation synthesis nanodiamond. *Diamond and Related Materials*, 9(3):861 – 865, 2000. 10.1016/S0925-9635(99)00354-4.

[35] G. V. Sakovich, A. S. Zharkov, and E. A. Petrov. Results of research into the physicochemical processes of detonation synthesis and nanodiamond applications. *Nanotechnologies in Russia*, 8(9-10):581–591, 2013.

[36] Long-Jyun Su, Chia-Yi Fang, Yu-Tang Chang, Kuan-Ming Chen, Yueh-Chung Yu, Jui-Hung Hsu, and Huan-Cheng Chang. Creation of high density ensembles of nitrogen-vacancy centers in nitrogen-rich type ib nanodiamonds. *Nanotechnology*, 24(31):315702, jul 2013.

[37] Jean-Paul Boudou, Patrick A Curmi, Fedor Jelezko, Joerg Wrachtrup, Pascal Aubert, Mohamed Sennour, Gopalakrischnan Balasubramanian, Rolf Reuter, Alain Thorel, and Eric Gaffet. High yield fabrication of fluorescent nanodiamonds. *Nanotechnology*, 20(23):235602, may 2009.

[38] Jin-Xu Qin, Xi-Gui Yang, Chao-Fan Lv, Yi-Zhe Li, Kai-Kai Liu, Jin-Hao Zang, Xun Yang, Lin Dong, and Chong-Xin Shan. Nanodiamonds: Synthesis, properties, and applications in nanomedicine. *Materials Design*, 210:110091, 2021.

[39] W Fortunato, AJ Chiquito, JC Galzerani, and JR Moro. Crystalline quality and phase purity of cvd diamond films studied by raman spectroscopy. *Journal of materials science*, 42(17):7331–7336, 2007.

[40] K. Fabisiak, M. Szreiber, C. Uniszkiewicz, T. Runka, and D. Kasprowicz. Electron paramagnetic resonance and raman spectroscopy characterization of diamond films fabricated by hf cvd method. *Crystal Research and Technology*, 45(2):167–172, 2010.

[41] J. C. Lascovich and S. Scaglione. Comparison among xaes, pels and xps techniques for evaluation of sp2 percentage in a-c:h. *Applied Surface Science*, 78(1):17–23, 1994.

[42] A.T. Kozakov, A.G. Kochur, N. Kumar, K. Panda, A.V. Nikolskii, and A.V. Sidashov. Determination of sp2 and sp3 phase fractions on the surface of diamond films from c1s, valence band x-ray photoelectron spectra and ckvv x-ray-excited auger spectra. *Applied Surface Science*, 536:147807, 2021.

[43] Stepan Stehlik, Marian Varga, Martin Ledinsky, Vit Jirasek, Anna Artemenko, Halyna Kozak, Lukas Ondic, Viera Skakalova, Giacomo Argentero, Timothy Pennycook, et al. Size and purity control of hpht nanodiamonds down to 1 nm. *The Journal of Physical Chemistry C*, 119(49):27708–27720, 2015. 10.1021/acs.jpcc.5b05259.

[44] In Y. Gogotsi and V. Presser, editors. *Carbon Nanomaterials (Advanced Materials and Technologies)*. CRC Press, second edition, 2013. ISBN: 9781439897812.

[45] Laia Ginés, Soumen Mandal, David John Morgan, Ryan Lewis, Philip R. Davies, Paola Borri, Gavin W. Morley, and Oliver A. Williams. Production of metal-free diamond nanoparticles. *ACS Omega*, 3(11):16099–16104, 2018.

[46] Amanda M. Schrand, Liming Dai, John J. Schlager, Saber M. Hussain, and Eiji Osawa. Differential biocompatibility of carbon nanotubes and nanodiamonds. *Diamond and Related Materials*, 16(12):2118–2123, 2007. Proceedings of the Joint International Conference: Nanocarbon and Nanodiamond 2006.

[47] A.P. Puzyr, D.A. Neshumayev, S.V. Tarskikh, G.V. Makarskaya, V.Yu. Dolmatov, and V.S. Bondar. Destruction of human blood cells in interaction with detonation nanodiamonds in experiments in vitro. *Diamond and Related Materials*, 13(11):2020–2023, 2004. Proceedings of the 9th International Conference on New Diamond Science and Technology (ICNDST-9).

[48] Yu-Chung Lin, Lin-Wei Tsai, Elena V. Perevedentseva, Jani Mona, Chia-Liang Cheng, Hsin-Hou Chang, Ching-Hui Lin, Der-Shan Sun, Andrei E. Lugovtsov, and Alexander V. Priezzhev. The influence of nanodiamond on the oxygenation states and micro rheological properties of human red blood cells in vitro. *Journal of Biomedical Optics*, 17(10):1 – 10, 2012.

[49] Michal Wasowicz, Mateusz Ficek, Maciej S. Wróbel, Ruchira Chakraborty, Dror Fixler, Pawel Wierzba, and Malgorzata Jedrzejewska-Szczerska. Haemocompatibility of modified nanodiamonds. *Materials*, 10(4), 2017.

[50] Lin-Wei Tsai, Yu-Chung Lin, Elena Perevedentseva, Andrei Lugovtsov, Alexander Priezzhev, and Chia-Liang Cheng. Nanodiamonds for medical applications: Interaction with blood in vitro and in vivo. *International Journal of Molecular Sciences*, 17(7), 2016.

[51] Amanda M. Schrand, Houjin Huang, Cataleya Carlson, John J. Schlager, Eiji Osawa, Saber M. Hussain, and Liming Dai. Are diamond nanoparticles cytotoxic? *The Journal of Physical Chemistry B*, 111(1):2–7, 2007. PMID: 17201422.

[52] K Turcheniuk and Vadym N Mochalin. Biomedical applications of nanodiamond (review). *Nanotechnology*, 28(25):252001, jun 2017.

[53] Yu-Wei Lin, Emmanuel Naveen Raj, Wei-Siang Liao, Johnson Lin, Kuang-Kai Liu, Ting-Hua Chen, Hsiao-Chun Cheng, Chi-Ching Wang, Lily Li, Chinpiao Chen, and Jui-I Chao. Co-delivery of paclitaxel and cetuximab by nanodiamond enhances mitotic catastrophe and tumor inhibition open. *Scientific Reports*, 7, 08 2017.

[54] James Giammarco, Vadym N. Mochalin, James Haeckel, and Yury Gogotsi. The adsorption of tetracycline and vancomycin onto nanodiamond with controlled release. *Journal of Colloid and Interface Science*, 468:253–261, 2016.

[55] *Concise Medical Dictionary*. Oxford University Press, Oxford, 8th edition, 2010.

[56] Xin Wang, Xinyi Casuarine Low, Weixin Hou, Lissa Nurrul Abdullah, Tan Boon Toh, Masturah Mohd Abdul Rashid, Dean Ho, and Edward Kai-Hua Chow. Epirubicin-adsorbed nanodiamonds kill chemoresistant hepatic cancer stem cells. *ACS Nano*, 8(12):12151–12166, 2014. PMID: 25437772.

[57] Hao Zhu, Yun Wang, Abid Hussain, Zhipeng Zhang, Yuanyuan Shen, and Shengrong Guo. Nanodiamond mediated co-delivery of doxorubicin and malaridine to maximize synergistic anti-tumor effects on multi-drug resistant mcf-7/adr cells. *J. Mater. Chem. B*, 5:3531–3540, 2017.

[58] A Coonrod, FQ Li, and M Horwitz. On the mechanism of dna transfection: efficient gene transfer without viruses. *Gene therapy*, 4(12):1313–1321, 1997.

[59] C M Gorman, G T Merlino, M C Willingham, I Pastan, and B H Howard. The rous sarcoma virus long terminal repeat is a strong promoter when introduced into a variety of eukaryotic cells by dna-mediated transfection. *Proceedings of the National Academy of Sciences*, 79(22):6777–6781, 1982.

[60] Murali Ramamoorth and Aparna Narvekar. Non viral vectors in gene therapy-an overview. *Journal of clinical and diagnostic research: JCDR*, 9(1):GE01, 2015.

[61] Roberto Martín, Mercedes Álvaro, José Raúl Herance, and Hermenegildo García. Fenton-treated functionalized diamond nanoparticles as gene delivery system. *ACS Nano*, 4(1):65–74, 2010. PMID: 20047335.

[62] Alexandre Barras, Fernando Ariel Martin, Omprakash Bande, Jean-Sébastien Baumann, Jean-Marc Ghigo, Rabah Boukherroub, Christophe Beloin, Aloysius Siriwardena, and Sabine Szunerits. Glycan-functionalized diamond nanoparticles as potent e. coli anti-adhesives. *Nanoscale*, 5(6):2307–2316, 2013.

[63] Manakamana Khanal, Viktoria Raks, Rahaf Issa, Volodymyr Chernyshenko, Alexandre Barras, Jose M. Garcia Fernandez, Lyuba I. Mikhalovska, Volodymyr Turcheniuk, Vladimir Zaitsev, Rabah Boukherroub, Aloysius Siriwardena, Ian R. Cooper, Peter J. Cragg, and Sabine Szunerits. Selective antimicrobial and antibiofilm disrupting properties of functionalized diamond nanoparticles against escherichia coli and staphylococcus aureus. *Particle & Particle Systems Characterization*, 32(8):822–830, 2015.

[64] Dong-Keun Lee, Sue Vin Kim, Adelheid Nerisa Limansubroto, Albert Yen, Akrivoula Soundia, Cun-Yu Wang, Wenyuan Shi, Christine Hong, Sotirios Tetradis, Yong Kim, No-Hee Park, Mo K. Kang, and Dean Ho. Nanodiamond-gutta percha composite biomaterials for root canal therapy. *ACS Nano*, 9(11):11490–11501, 2015. PMID: 26452304.

[65] D Ho. Nanodiamond modified gutta percha (ndgp) composite for non-surgical root canal therapy (rct) filler material. *University of California, Los Angeles*, 2016.

[66] S Pezzagna, B Naydenov, F Jelezko, J Wrachtrup, and J Meijer. Creation efficiency of nitrogen-vacancy centres in diamond. *New Journal of Physics*, 12(6):065017, jun 2010.

[67] Konstantin Iakoubovskii and Guy J Adriaenssens. Trapping of vacancies by defects in diamond. *Journal of Physics: Condensed Matter*, 13(26):6015, 2001.

[68] Shu-Jung Yu, Ming-Wei Kang, Huan-Cheng Chang, Kuan-Ming Chen, and Yueh-Chung Yu. Bright fluorescent nanodiamonds: No photobleaching and low cytotoxicity. *Journal of the American Chemical Society*, 127(50):17604–17605, 2005. PMID: 16351080.

[69] Neeraj Prabhakar, Tuomas Näreoja, Eva von Haartman, Didem Şen Karaman, Hua Jiang, Sami Koho, Tatiana A Dolenko, Pekka E Hänninen, Denis I Vlasov, Victor G Ralchenko, et al. Core–shell designs of photoluminescent nanodiamonds with porous silica coatings for bioimaging and drug delivery ii: application. *Nanoscale*, 5(9):3713–3722, 2013.

[70] Nitin Mohan, Chao-Sheng Chen, Hsiao-Han Hsieh, Yi-Chun Wu, and Huan-Cheng Chang. In vivo imaging and toxicity assessments of fluorescent nanodiamonds in caenorhabditis elegans. *Nano Letters*, 10(9):3692–3699, 2010. PMID: 20677785.

[71] Francisco Morales-Zavala, Nathalie Casanova-Morales, Raúl B Gonzalez, América Chandía-Cristi, Lisbell D Estrada, Ignacio Alvizú, Victor Waselowski, Fanny Guzman, Simón Guerrero, Marisol Oyarzún-Olave, et al. Functionalization of stable fluorescent nanodiamonds towards reliable detection of biomarkers for alzheimerâs disease. *Journal of nanobiotechnology*, 16(1):1–14, 2018.

[72] Tobias D Merson, Stefania Castelletto, Igor Aharonovich, Alisa Turbic, Trevor J Kilpatrick, and Ann M Turnley. Nanodiamonds with silicon vacancy defects for nontoxic photostable fluorescent labeling of neural precursor cells. *Optics letters*, 38(20):4170–4173, 2013.

[73] Andrew Magyar, Wenhao Hu, Toby Shanley, Michael E Flatté, Evelyn Hu, and Igor Aharonovich. Synthesis of luminescent europium defects in diamond. *Nature communications*, 5(1):1–6, 2014.

[74] Jun Xiao, Pu Liu, Lihua Li, and Guowei Yang. Fluorescence origin of nanodiamonds. *The Journal of Physical Chemistry C*, 119(4):2239–2248, 2015.

[75] Carlo Bradac, Torsten Gaebel, Chris. I. Pakes, Jana M. Say, Andrei V. Zvyagin, and James R. Rabeau. Effect of the nanodiamond host on a nitrogen-vacancy color-centre emission state. *Small*, 9(1):132–139, 2013.

[76] Bradley R. Smith, David W. Inglis, Bjornar Sandnes, James R. Rabeau, Andrei V. Zvyagin, Daniel Gruber, Christopher J. Noble, Robert Vogel, Eiji Åsawa, and Taras Plakhotnik. Five-nanometer diamond with luminescent nitrogen-vacancy defect centers. *Small*, 5(14):1649–1653, 2009.

[77] M. V. Hauf, B. Grotz, B. Naydenov, M. Dankerl, S. Pezzagna, J. Meijer, F. Jelezko, J. Wrachtrup, M. Stutzmann, F. Reinhard, and J. A. Garrido. Chemical control of the charge state of nitrogen-vacancy centers in diamond. *Phys. Rev. B*, 83:081304, Feb 2011.

[78] Iestyn Pope, Lukas Payne, George Zoriniants, Evan Thomas, Oliver Williams, Peter Watson, Wolfgang Langbein, and Paola Borri. Coherent anti-stokes raman scattering microscopy of single nanodiamonds. *Nature nanotechnology*, 9(11):940–946, 2014.

[79] Sumio Iijima. Helical microtubules of graphitic carbon. *nature*, 354(6348):56–58, 1991.

[80] M. Mittal and A. Kumar. Carbon nanotube (cnt) gas sensors for emissions from fossil fuel burning. *Sensors and Actuators B: Chemical*, 203:349–362, 2014.

[81] Susan B. Sinnott and Rodney Andrews. Carbon nanotubes: Synthesis, properties, and applications. *Critical Reviews in Solid State and Materials Sciences*, 26(3):145–249, 2001.

[82] J. W. Mintmire, B. I. Dunlap, and C. T. White. Are fullerene tubules metallic? *Phys. Rev. Lett.*, 68:631–634, Feb 1992.

[83] Noriaki Hamada, Shin-ichi Sawada, and Atsushi Oshiyama. New one-dimensional conductors: Graphitic microtubules. *Phys. Rev. Lett.*, 68:1579–1581, Mar 1992.

[84] Zixian Li, Andre Luis Branco de Barros, Daniel Cristian Ferreira Soares, Sara Nicole Moss, and Laleh Alisaraie. Functionalized single-walled carbon nanotubes: cellular uptake, biodistribution and applications in drug delivery. *International Journal of Pharmaceutics*, 524(1):41–54, 2017.

[85] Raghavendra Prasad and Badekai Ramachandra Bhat. Multi-wall carbon nanotube-nio nanoparticle composite as enzyme-free electrochemical glucose sensor. *Sensors and Actuators B: Chemical*, 220:81–90, 2015.

[86] Anna Kolanowska, Artur P. Herman, Rafal G. Jedrysiak, and Slawomir Boncel. Carbon nanotube materials for electrocardiography. *RSC Adv.*, 11:3020–3042, 2021.

[87] M. Bronikowski, P. Willis, D. Colbert, K. Smith, and R. Smalley. Gas-phase production of carbon single-walled nanotubes from carbon monoxide via the hipco process: A parametric study. *Journal of Vacuum Science and Technology*, 19:1800–1805, 2001.

[88] Neha Arora and N.N. Sharma. Arc discharge synthesis of carbon nanotubes: Comprehensive review. *Diamond and Related Materials*, 50:135–150, 2014.

[89] Friedrich Schöppler, Christoph Mann, Tilman C. Hain, Felix M. Neubauer, Giulia Privitera, Francesco Bonaccorso, Daping Chu, Andrea C. Ferrari, and Tobias Hertel. Molar extinction coefficient of single-wall carbon nanotubes. *The Journal of Physical Chemistry C*, 115(30):14682–14686, 2011.

[90] Laura Oudjedi, A. Nicholas G. Parra-Vasquez, Antoine G. Godin, Laurent Cognet, and Brahim Lounis. Metrological investigation of the (6,5) carbon nanotube absorption cross section. *The Journal of Physical Chemistry Letters*, 4(9):1460–1464, 2013. PMID: 26282299.

[91] A. M. Rao, E. Richter, Shunji Bandow, Bruce Chase, P. C. Eklund, K. A. Williams, S. Fang, K. R. Subbaswamy, M. Menon, A. Thess, R. E. Smalley, G. Dresselhaus, and M. S. Dresselhaus. Diameter-selective raman scattering from vibrational modes in carbon nanotubes. *Science*, 275(5297):187–191, 1997.

[92] Paulo T. Araujo, Stephen K. Doorn, Svetlana Kilina, Sergei Tretiak, Erik Einarsson, Shigeo Maruyama, Helio Chacham, Marcos A. Pimenta, and Ado Jorio. Third and fourth optical transitions in semiconducting carbon nanotubes. *Phys. Rev. Lett.*, 98:067401, Feb 2007.

[93] P. T. Araujo, I. O. Maciel, P. B. C. Pesce, M. A. Pimenta, S. K. Doorn, H. Qian, A. Hartschuh, M. Steiner, L. Grigorian, K. Hata, and A. Jorio. Nature of the constant factor in the relation between radial breathing mode frequency and tube diameter for single-wall carbon nanotubes. *Phys. Rev. B*, 77:241403, Jun 2008.

[94] Louis De Broglie. Xxxv. a tentative theory of light quanta. *Philosophical Magazine Letters*, 86(7):411–423, 2006.

[95] D Mathys. Die entwicklung der elektronenmikroskopie vom bild über die analyse zum nanolabor. *Zentrum für Mikroskopie, University of Basel*, page 8, 2004.

[96] James hillier. https://lemelson.mit.edu/resources/james-hillier. Retrieved March 15th 2023.

[97] Marc De Graef. *Introduction to conventional transmission electron microscopy.* Cambridge University Press, Cambridge, 2003.

[98] Joseph I Goldstein, Dale E Newbury, Joseph R Michael, Nicholas WM Ritchie, John Henry J Scott, and David C Joy. *Scanning electron microscopy and X-ray microanalysis.* Springer, 2017.

[99] T E Everhart and R F M Thornley. Wide-band detector for micro-microampere low-energy electron currents. *Journal of Scientific Instruments*, 37(7):246, jul 1960.

[100] J. Pérez-Arantegui and T. Mulvey. Microscopy techniques | electron microscopy. In Paul Worsfold, Alan Townshend, and Colin Poole, editors, *Encyclopedia of Analytical Science (Second Edition)*, pages 114–124. Elsevier, Oxford, second edition edition, 2005.

[101] L.M. Lacava, B.M. Lacava, R.B. Azevedo, Z.G.M. Lacava, N. Buske, A.L. Tronconi, and P.C. Morais. Nanoparticle sizing: a comparative study using atomic force microscopy, transmission electron microscopy, and ferromagnetic resonance. *Journal of Magnetism and Magnetic Materials*, 225(1):79–83, 2001. Proceedings of the Third International Conference on Scientific and Clinical Applications of Magnetic Carriers.

[102] A.E. Vladár and Vasile-Dan Hodoroaba. Characterization of nanoparticles by scanning electron microscopy. In *Characterization of Nanoparticles*, pages 7–27. Elsevier, 2020.

[103] Najoua Bouzakher Ghomrasni, Carine Chivas-Joly, Laurent Devoille, Jean-Francois Hochepied, and Nicolas Feltin. Challenges in sample preparation for measuring nanoparticles size by scanning electron microscopy from suspensions, powder form and complex media. *Powder Technology*, 359:226–237, 2020.

[104] Frank Babick. Dynamic light scattering (dls). In *Characterization of Nanoparticles*, Micro and Nano Technologies, pages 137–172. Elsevier, 2020.

[105] Will Anderson, Darby Kozak, Victoria A. Coleman, Åsa K. Jämting, and Matt Trau. A comparative study of submicron particle sizing platforms: Accuracy, precision and resolution analysis of polydisperse particle size distributions. *J. Colloid Interface Sci.*, 405:322–330, sep 2013.

[106] Vasco Filipe, Andrea Hawe, and Wim Jiskoot. Critical evaluation of nanoparticle tracking analysis (nta) by nanosight for the measurement of nanoparticles and protein aggregates. *Pharmaceutical research*, 27:796–810, 2010.

[107] Anna D Kashkanova, Martin Blessing, André Gemeinhardt, Didier Soulat, and Vahid Sandoghdar. Precision size and refractive index analysis of weakly scattering nanoparticles in polydispersions. *Nature methods*, 19(5):586–593, 2022.

[108] Kristen E Thane, Airiel M Davis, and Andrew M Hoffman. Improved methods for fluorescent labeling and detection of single extracellular vesicles using nanoparticle tracking analysis. *Scientific Reports*, 9(1):12295, 2019.

[109] Jonathan Dong, Dante Maestre, Clara Conrad-Billroth, and Thomas Juff-mann. Fundamental bounds on the precision of iscat, cobri and dark-field microscopy for 3d localization and mass photometry. *Journal of Physics D: Applied Physics*, 54(39):394002, jul 2021.

[110] L. A. Amos and W. B. Amos. The bending of sliding microtubules imaged by confocal light microscopy and negative stain electron microscopy. *Journal of Cell Science*, 1991(Supplement_14):95–101, 01 1991.

[111] Katelyn M. Spillane, Jaime Ortega-Arroyo, Gabrielle de Wit, Christian Eggeling, Helge Ewers, Mark I. Wallace, and Philipp Kukura. High-speed single-particle tracking of gm1 in model membranes reveals anomalous dif-fusion due to interleaflet coupling and molecular pinning. *Nano Letters*, 14(9):5390–5397, 2014. PMID: 25133992.

[112] Richard W Taylor, Reza Gholami Mahmoodabadi, Verena Rauschenberger, Andreas Giessl, Alexandra Schambony, and Vahid Sandoghdar. Interferomet-ric scattering microscopy reveals microsecond nanoscopic protein motion on a live cell membrane. *Nature Photonics*, 13(7):480–487, 2019.

[113] Eric DB Foley, Manish S Kushwah, Gavin Young, and Philipp Kukura. Mass photometry enables label-free tracking and mass measurement of single pro-teins on lipid bilayers. *Nature Methods*, 18(10):1247–1252, 2021.

[114] Gavin Young, Nikolas Hundt, Daniel Cole, Adam Fineberg, Joanna Andrecka, Andrew Tyler, Anna Olerinyova, Ayla Ansari, Erik G. Marklund, Miranda P. Collier, Shane A. Chandler, Olga Tkachenko, Joel Allen, Max Crispin, Neil Billington, Yasuharu Takagi, James R. Sellers, Cédric Eichmann, Philipp Se-lenko, Lukas Frey, Roland Riek, Martin R. Galpin, Weston B. Struwe, Justin L. P. Benesch, and Philipp Kukura. Quantitative mass imaging of single bio-logical macromolecules. *Science*, 360(6387):423–427, 2018.

[115] Ching-Ya Cheng, Yi-Hung Liao, and Chia-Lung Hsieh. High-speed imag-ing and tracking of very small single nanoparticles by contrast enhanced mi-croscopy. *Nanoscale*, 11:568–577, 2019.

[116] Hendrik Christoffel Hulst and Hendrik C van de Hulst. *Light scattering by small particles*. Courier Corporation, 1981. ISBN: 0-486-64228-3.

[117] Lukas M. Payne, Attilio Zilli, Yisu Wang, Wolfgang Langbein, and Paola Borri. Quantitative high-throughput optical sizing of individual colloidal nanoparticles by wide-field imaging extinction microscopy . In Marek OsiÅski and Wolfgang J. Parak, editors, *Colloidal Nanoparticles for Biomedical Ap-plications XIV*, volume 10892, page 108920J. International Society for Optics and Photonics, SPIE, 2019.

[118] Extinction cross section. https://glossary.ametsoc.org/wiki/Extinction_cross_section, Feb 2012. Retrieved May 31st 2023.

[119] Aurélien Crut, Paolo Maioli, Natalia Del Fatti, and Fabrice Vallée. Optical absorption and scattering spectroscopies of single nano-objects. *Chem. Soc. Rev.*, 43:3921–3956, 2014.

[120] Julia M Bingham, Katherine A Willets, Nilam C Shah, David Q Andrews, and Richard P Van Duyne. Localized surface plasmon resonance imaging: simultaneous single nanoparticle spectroscopy and diffusional dynamics. *The Journal of Physical Chemistry C*, 113(39):16839–16842, 2009.

[121] Jan Becker, Olaf Schubert, and Carsten Sönnichsen. Gold nanoparticle growth monitored in situ using a novel fast optical single-particle spectroscopy method. *Nano letters*, 7(6):1664–1669, 2007.

[122] Mark W Knight, Jonathan Fan, Federico Capasso, and Naomi J Halas. Influence of excitation and collection geometry on the dark field spectra of individual plasmonic nanostructures. *Optics express*, 18(3):2579–2587, 2010.

[123] Lindsey JE Anderson, Kathryn M Mayer, Robert D Fraleigh, Yi Yang, Seunghyun Lee, and Jason H Hafner. Quantitative measurements of individual gold nanoparticle scattering cross sections. *The Journal of Physical Chemistry C*, 114(25):11127–11132, 2010.

[124] Li Ma, Peng Yu, Wenhao Wang, Hao-Chung Kuo, Alexander O. Govorov, Song Sun, and Zhiming Wang. Nanoantenna-enhanced light-emitting diodes: Fundamental and recent progress. *Laser & Photonics Reviews*, 15(5):2000367, 2021.

[125] T. Klar, M. Perner, S. Grosse, G. von Plessen, W. Spirkl, and J. Feldmann. Surface-plasmon resonances in single metallic nanoparticles. *Phys. Rev. Lett.*, 80:4249–4252, May 1998.

[126] David Lasne, Gerhard A Blab, Stéphane Berciaud, Martin Heine, Laurent Groc, Daniel Choquet, Laurent Cognet, and Brahim Lounis. Single nanoparticle photothermal tracking (snapt) of 5-nm gold beads in live cells. *Biophysical journal*, 91(12):4598–4604, 2006.

[127] Stéphane Berciaud, Laurent Cognet, Gerhard A. Blab, and Brahim Lounis. Photothermal heterodyne imaging of individual nonfluorescent nanoclusters and nanocrystals. *Phys. Rev. Lett.*, 93:257402, Dec 2004.

[128] Lukas M. Payne, Wolfgang Langbein, and Paola Borri. Polarization-resolved extinction and scattering cross-sections of individual gold nanoparticles measured by wide-field microscopy on a large ensemble. *Applied Physics Letters*, 102(13):131107, 2013.

[129] Lukas M. Payne, Wolfgang Langbein, and Paola Borri. Wide-Field Imaging of Single-Nanoparticle Extinction with Sub-nm2 Sensitivity. *Physical Review Applied*, 9:034006, March 2018.

[130] Attilio Zilli, Wolfgang Langbein, and Paola Borri. Quantitative measurement of the optical cross sections of single nano-objects by correlative transmission and scattering microspectroscopy. *ACS Photonics*, 6(8):2149–2160, 2019. PMID: 32064304.

[131] R. Kalita, J. Lightley, S. Kumar, Y. Alexandrov, E. Garcia, W. Flanagan, M. A. A. Neil, C. Dunsby, and P. M. W. French. Single-shot quantitative phase contrast using polarisation-resolved differential phase microscopy. In

Emmanuel Beaurepaire, Adela Ben-Yakar, and YongKeun Park, editors, *Advances in Microscopic Imaging III*, volume 11922, page 119220Y. International Society for Optics and Photonics, SPIE, 2021.

[132] Michael Reed Teague. Deterministic phase retrieval: a green's function solution. *J. Opt. Soc. Am.*, 73(11):1434–1441, Nov 1983.

[133] Emrah Bostan, Emmanuel Froustey, Benjamin Rappaz, Etienne Shaffer, Daniel Sage, and Michael Unser. Phase retrieval by using transport-of-intensity equation and differential interference contrast microscopy. In *2014 IEEE International Conference on Image Processing (ICIP)*, pages 3939–3943, 2014.

[134] Stephen D. Grant, Kyle Richford, Heidi L. Burdett, David McKee, and Brian R. Patton. Low-cost, open-access quantitative phase imaging of algal cells using the transport of intensity equation. *Royal Society Open Science*, 7(1):191921, 2020.

[135] John Rodenburg and Andrew Maiden. *Ptychography*, pages 819–904. Springer International Publishing, Cham, 2019.

[136] Yi Jiang, Zhen Chen, Yimo Han, Pratiti Deb, Hui Gao, Saien Xie, Prafull Purohit, Mark W Tate, Jiwoong Park, Sol M Gruner, et al. Electron ptychography of 2d materials to deep sub-ångström resolution. *Nature*, 559(7714):343–349, 2018.

[137] Nomarski Georges. Interferential polarizing device for study of phase objects, February 9 1960. US Patent 2,924,142.

[138] Bradley R. Smith, Marcus Niebert, Taras Plakhotnik, and Andrei V. Zvyagin. Transfection and imaging of diamond nanocrystals as scattering optical labels. *Journal of Luminescence*, 127(1):260 – 263, 2007. Proceedings of the Ninth International Meeting on Hole Burning, Single Molecule, and Related Spectroscopies: Science and Applications.

[139] Xiquan Cui, Matthew Lew, and Changhuei Yang. Quantitative differential interference contrast microscopy based on structured-aperture interference. *Applied Physics Letters*, 93(9):091113, 2008.

[140] Carol J. Cogswell, Nicholas I. Smith, Kieran G. Larkin, and Parameswaran Hariharan. Quantitative DIC microscopy using a geometric phase shifter. In Carol J. Cogswell, Jose-Angel Conchello, and Tony Wilson, editors, *Three-Dimensional Microscopy: Image Acquisition and Processing IV*, volume 2984, pages 72 – 81. International Society for Optics and Photonics, SPIE, 1997.

[141] Sharon V. King, Ariel R. Libertun, Chrysanthe Preza, and Carol J. Cogswell. Calibration of a phase-shifting DIC microscope for quantitative phase imaging. In Jose-Angel Conchello, Carol J. Cogswell, and Tony Wilson, editors, *Three-Dimensional and Multidimensional Microscopy: Image Acquisition and Processing XIV*, volume 6443, pages 105 – 116. International Society for Optics and Photonics, SPIE, 2007.

[142] CI McPhee, G Zoriniants, W Langbein, and Paola Borri. Measuring the lamellarity of giant lipid vesicles with differential interference contrast microscopy. *Biophysical journal*, 105(6):1414–1420, 2013.

[143] David Regan, Joseph Williams, Paola Borri, and Wolfgang Langbein. Lipid Bilayer Thickness Measured by Quantitative DIC Reveals Phase Transitions and Effects of Substrate Hydrophilicity. *LANGMUIR*, 35(43):13805–13814, OCT 29 2019.

[144] David Regan, Joseph Williams, Francesco Masia, Paola Borri, and Wolfgang Langbein. Measuring sub-nanometre thickness changes during phase transitions of supported lipid bilayers with quantitative differential interference contrast microscopy. In Popescu, G and Park, Y, editor, *QUANTITATIVE PHASE IMAGING V*, volume 10887 of *Proceedings of SPIE*, 1000 20TH ST, PO BOX 10, BELLINGHAM, WA 98227-0010 USA, 2019. SPIE; Tomocube, Inc; Phi Optics, Inc, SPIE-INT SOC OPTICAL ENGINEERING. Conference on Quantitative Phase Imaging V, San Francisco, CA, FEB 02-05, 2019.

[145] Chandrasekhara Venkata Raman. A new radiation. *Indian Journal of physics*, 2:387–398, 1928.

[146] G Landsberg. Eine neue erscheinung bei der lichtzerstreuung in krystallen. *Naturwissenschaften*, 16(28):557–558, Jul 1928. 10.1007/BF01506807.

[147] Geo. Glockler. The raman effect. *Rev. Mod. Phys.*, 15:111–173, Apr 1943.

[148] D. J. Gardiner. *Practical Raman Spectroscopy.* Springer Verlag, 1989. ISBN: 9780387502548.

[149] M. Balkanski. Semiconductor physics | light scattering. In Robert D. Guenther, editor, *Encyclopedia of Modern Optics*, pages 460–465. Elsevier, Oxford, 2005.

[150] S. A. Solin and A. K. Ramdas. Raman spectrum of diamond. *Phys. Rev. B*, 1:1687–1698, Feb 1970.

[151] F. Tuinstra and J. L. Koenig. Raman spectrum of graphite. *The Journal of Chemical Physics*, 53(3):1126–1130, 1970.

[152] Haiyong Gao, Fawang Yan, Huixiao Zhang, Jinmin Li, Junxi Wang, and Jianchang Yan. First and second order raman scattering spectroscopy of nonpolar a-plane gan. *Journal of Applied Physics*, 101(10):103533, 2007.

[153] RS Krishnan. The second order raman spectrum of diamond. In *Proceedings of the Indian Academy of Sciences-Section A*, volume 24, pages 25–32. Springer India, 1946.

[154] V. S. Gorelik and Đ. Yu Pyatyshev. Raman scattering in diamond nano- and microcrystals, synthesized at high temperatures and high pressures. *Diamond and Related Materials*, 110:108104, 2020.

[155] Robin R Jones, David C Hooper, Liwu Zhang, Daniel Wolverson, and Ventsislav K Valev. Raman techniques: Fundamentals and frontiers. *Nanoscale research letters*, 14(1):1–34, 2019.

[156] EJ Woodbury and WK Ng. Ruby laser operation in near ir. *Proceedings of the Institute of Radio Engineers*, 50(11):2367, 1962.

[157] Qian Cheng, Yupeng Miao, Joseph Wild, Wei Min, and Yuan Yang. Emerging applications of stimulated raman scattering microscopy in materials science. *Matter*, 4(5):1460–1483, 2021.

[158] Christian W Freudiger, Wei Min, Brian G Saar, Sijia Lu, Gary R Holtom, Chengwei He, Jason C Tsai, Jing X Kang, and X Sunney Xie. Label-free biomedical imaging with high sensitivity by stimulated raman scattering microscopy. *Science*, 322(5909):1857–1861, 2008.

[159] Vladislav V Yakovlev, Georgi I Petrov, Hao F Zhang, Gary D Noojin, Michael L Denton, Robert J Thomas, and Marlan O Scully. Stimulated raman scattering: old physics, new applications. *Journal of modern optics*, 56(18-19):1970–1973, 2009.

[160] Olutayo I. Olubiyi, Fa-Ke Lu, David Calligaris, Ferenc A. Jolesz, and Nathalie Y. Agar. *Chapter 17 - Advances in Molecular Imaging for Surgery*, pages 407–439. Academic Press, Boston, 2015.

[161] A Virga, C Ferrante, G Batignani, D De Fazio, ADG Nunn, AC Ferrari, G Cerullo, and T Scopigno. Coherent anti-stokes raman spectroscopy of single and multi-layer graphene. *Nature Communications*, 10(1):3658, 2019.

[162] E. O. Potma and S Mukamel. Theory of coherent raman scattering. *Coherent Raman Scattering Microscopy*, 2012.

[163] J. P. Gordon, R. C. C. Leite, R. S. Moore, S. P. S. Porto, and J. R. Whinnery. Long−transient effects in lasers with inserted liquid samples. *Journal of Applied Physics*, 36(1):3–8, 1965.

[164] ME Long, RL Swofford, and AC Albrecht. Thermal lens technique: a new method of absorption spectroscopy. *Science*, 191(4223):183–185, 1976.

[165] Dong-Kwon Lim, Aoune Barhoumi, Ryan G. Wylie, Gally Reznor, Robert S. Langer, and Daniel S. Kohane. Enhanced photothermal effect of plasmonic nanoparticles coated with reduced graphene oxide. *Nano Letters*, 13(9):4075–4079, 2013. PMID: 23899267.

[166] Subhasis Adhikari, Patrick Spaeth, Ashish Kar, Martin Dieter Baaske, Saumyakanti Khatua, and Michel Orrit. Photothermal microscopy: imaging the optical absorption of single nanoparticles and single molecules. *ACS nano*, 14(12):16414–16445, 2020.

[167] Stéphane Berciaud, David Lasne, Gerhard A. Blab, Laurent Cognet, and Brahim Lounis. Photothermal heterodyne imaging of individual metallic nanoparticles: Theory versus experiment. *Phys. Rev. B*, 73:045424, Jan 2006.

[168] Mikhail A. Proskurnin, Liliya O. Usoltseva, Dmitry S. Volkov, Dmitry A. Nedosekin, Mikhail V. Korobov, and Vladimir P. Zharov. Photothermal and heat-transfer properties of aqueous detonation nanodiamonds by photothermal microscopy and transient spectroscopy. *The Journal of Physical Chemistry C*, 125(14):7808–7823, 2021.

[169] Pascal Berto, Esben Ravn Andresen, and Hervé Rigneault. Background-free stimulated raman spectroscopy and microscopy. *Phys. Rev. Lett.*, 112:053905, Feb 2014.

[170] Wolfgang Langbein, David Regan, Iestyn Pope, and Paola Borri. Invited article: Heterodyne dual-polarization epi-detected cars microscopy for chemical and topographic imaging of interfaces. *APL Photonics*, 3(9):092402, 2018.

[171] Kristof Reynkens, Stéphane Clemmen, Haolan Zhao, Ali Raza, Tom Vanackere, Andim Stassen, Michiel Van Daele, Jolien Dendooven, and Roel Baets. Gold-induced photothermal background in on-chip surface enhanced stimulated raman spectroscopy. *Opt. Lett.*, 46(5):953–956, Mar 2021.

[172] Y Oki, S Nakazono, Y Nonaka, and M Maeda. Sensitive h(2) detection by use of thermal-lens raman spectroscopy without a tunable laser. *Optics letters*, 25(14):1040–1042, July 2000.

[173] Samuel Hamilton, David Regan, Lukas Payne, Wolfgang Langbein, and Paola Borri. Sizing individual dielectric nanoparticles with quantitative differential interference contrast microscopy. *Analyst*, 147:1567–1580, 2022.